Model Predictive Climate Control for Connected and Automated Vehicles

by

Hao Wang

A dissertation submitted in partial fulfillment
of the requirements for the degree of
Doctor of Philosophy
(Naval Architecture and Marine Engineering)
in the University of Michigan
2019

Doctoral Committee:

Professor Ilya Kolmanovsky, Co-chair
Professor Jing Sun, Co-Chair
Professor Andre Boehman
Professor Heath Hofmann

autowang@umich.edu

ORCID: 0000-0001-8509-6635

To my parents for their selfless love and support.
And to Yifan, for always standing by me.

Acknowledgments

Looking back on my seven years at the University of Michigan and my five-year research experience here, I can remember how challenging this endeavor seemed at the beginning and now I can see everything has turned out okay, if not great, in the end. Towards the end of my PhD study, I developed from a curious graduate student into a researcher who enjoys the process of exploring unknowns. This would not have happened without my advisors, teachers, colleagues, friends and family.

I would first like to thank my advisors Prof. Jing Sun and Prof. Ilya Kolmanovsky for being both supportive and inspiring throughout my graduate studies. In addition to the guidance Prof. Sun has provided in my research endeavors, she has cared about my well-being by encouraging me through the more frustrating aspects of my work. Prof. Kolmanovsky is always humble but rigorous; furthermore, he inspires extraordinary ideas in my research. Both advisors have set the highest standard by being excellent role models. I would also like to thank Prof. Andre Boehman and Prof. Heath Hofmann for serving on my dissertation committee and providing valuable feedback on my work.

Next, I would like to extend a special thanks to Dr. Reza Amini. I have learned a lot about being an independent researcher while collaborating closely with him throughout this dissertation work. I would like to thank Qiuhao Hu for helping with the vehicle tests, especially under extreme weather conditions. In addition, I am grateful to have been a member of our RACE lab and for the time spent with my excellent lab members: Caihao Weng, Zeng Qiu, Jun Hou, Ziyou Song, Xun Gong, Esteban L. Castro, Richard Choroszucha, Zhenzhong Jia, Hyeongjun Park, Dave Reed, Kai Wu, Niankai Yang, Fanny Pinto Delgado, and Dongsik Chang.

I am also grateful to Mr. Mark Jennings for providing me with a valuable internship opportunity at Ford Motor Company. My internship experience stimulated subsequent development of my dissertation work. I would like to express my thanks to my supervisor, Yan Meng and my colleagues, Christopher Greiner, Quansheng Zhang, and Xiaowu Zhang for their guidance and help throughout my internship.

Last but not the least, I would like to thank my family members: my father, Yelin Wang, my mother, Lu Jiang, and my wife, Yifan Wang. Their company is my source of power throughout my life.

TABLE OF CONTENTS

LIST OF FIGURES

Figure

LIST OF TABLES

Table

LIST OF APPENDICES

Appendix

LIST OF ABBREVIATIONS

A/C Air Conditioning

CAL Cabin Air Loop

CAN Controller Area Network

CAV Connected and Automated Vehicle

CECO Combined Energy and Comfort Optimization

CECO-C CECO with Comfort Priority

CECO-E CECO with Energy Priority

COP Coefficient of Performance

DACE Discharge Air Cooling Energy

DACP Discharge Air Cooling Power

EDF Electric Ducted Fan

ICE Internal Combustion Engine

IOCH Intelligent Online Constraint Handling

iPTM Integrated Power and Thermal Management

HEV Hybrid Electric Vehicle

H-MPC Hierarchical Model Predictive Control

HVAC Heating Ventilation and Air Conditioning

MAF Mass Air Flow

MPC Model Predictive Control

LHV Lower Heating Value

LIN Local Interconnect Network

NREL National Renewable Energy Lab

NYCC New York City Cycle

OEM Original Equipment Manufacturer

OTC Occupant Thermal Comfort

PCS Precision Cooling Strategy

PTC Positive Temperature Coefficient

PMV Predicted Mean Vote

RL Refrigerant Loop

SC03 Supplemental Federal Test Procedure-1

SOC State of Charge

UDDS Urban Dynamometer Driving Schedule

UDP User Datagram Protocol

V2I Vehicle to Infrastructure

V2V Vehicle to Vehicle

ABSTRACT

Emerging connected and automated vehicle (CAV) technologies are improving vehicle safety and energy efficiency to the next level and creating unprecedented opportunities and challenges for the control and optimization of the vehicle systems. While previous studies have been focusing on improving the fuel efficiency via powertrain optimizations, vehicle thermal management and its interaction with powertrain control in hot and cold weather conditions have not been fully explored. For light-duty vehicles, the power used by the climate control system usually represents the most significant thermal load. It has been shown that the thermal load imposed by the climate control system may lead to dramatic vehicle range reduction, especially for the vehicles with electrified powertrains. Besides its noticeable impact on vehicle range reduction, the performance of the climate control system also has a direct influence on occupant comfort and customer satisfaction.

Aiming at reducing the energy consumption and improving the occupant thermal comfort (OTC) level for the automotive climate control system, this dissertation takes air conditioning (A/C) system as an example and is dedicated to developing practical A/C management strategies for electrified vehicles. In particular, the proposed strategies leverage the predictive information enabled by the CAV technologies such as the traffic and weather predictions. There are three novel MPC-based A/C management strategies developed in this dissertation, the hierarchical optimization, the precision cooling strategy (PCS), and the combined energy and comfort optimization (CECO). They can be differentiated by their OTC assumptions, robustness considerations, and implementation complexities on the testing vehicle.

In the hierarchical optimization, a two-layer hierarchical MPC (H-MPC) scheme is exploited for potential integration between the A/C and the powertrain systems of an Hybrid Electric Vehicle (HEV). This hierarchical structure handles the timescale difference between power and thermal systems as well as the uncertainties associated with long prediction horizon. Comprehensive simulation results over different driving cycles have demonstrated the energy saving potentials of efficient A/C energy management, which is attributes to leveraging the vehicle speed sensitivity of the A/C system efficiency. In terms of the comfort metric, the average cabin air temperature is applied.

In contrast to this hierarchical optimization, PCS and CECO utilize the simpler single-layer MPC structure assuming accurate predictive information. They are focusing on formulating more practical OTC metrics and the implementation on the testing vehicle. Specifically, the PCS renders the simplest control-oriented model structure and its energy benefits are validated based on an industrial-level A/C system model. The proposed PCS exploits a more practical comfort metric, Discharge Air Cooling Power (DACP), which directly motivates the design of an off-line eco-cooling strategy, which coordinates the A/C operation with respect to the vehicle speed. Vehicle-level energy saving is confirmed according to repeatable vehicle experiments.

Finally, the CECO strategy considers a comprehensive OTC model, Predicted Mean Vote (PMV), and combines the energy and comfort optimizations simultaneously. Further energy saving and OTC improvement can be achieved by explicitly leveraging both traffic and weather predictive information.

CHAPTER 1

Introduction

1.1 Connected and Automated Vehicles

The advent of Connected and Automated Vehicle (CAV) technologies [1] has created tremendous opportunities from control and optimization perspective to improve mobility, safety, and fuel economy/energy efficiency of the vehicles. With CAV, it is expected that the vehicle control system is able to exploit the Vehicle to Vehicle (V2V) and Vehicle to Infrastructure (V2I) communications for more efficient and safer vehicle operation. Different real-world driving scenarios, including highway [2, 3] and urban driving [4, 5], have been considered primarily for improving safety of CAVs. Meanwhile, significant energy saving potentials of CAVs has been envisioned [6, 7, 8, 9].

However, most of existing CAV-related research focuses on utilizing information from V2V/V2I or V2X (e.g., traffic signal and traffic flow information) to improve the powertrain system efficiency via eco-driving/platooning and route planning strategies [10, 11, 12, 13, 14]. At the same time, the literature focusing on the vehicle thermal management and co-optimization with traction power is relatively limited.

Typical thermal management systems in ground vehicles include the engine thermal management system [15, 16], aftertreatment and exhaust heat recovery systems [17, 18], battery and electric machine thermal management systems[19, 20], and cabin heating, ventilation, & air conditioning (HVAC) system [21, 22]. The thermal conditions can directly

affect the performance, reliability, and energy efficiency of the vehicle subsystems, especially in hot or cold environment. Nevertheless, in the context of connected and automated vehicles, how to leverage the V2X information for Integrated Power and Thermal Management (iPTM) is still an open question.

One major challenge for the iPTM of CAVs is to handle the timescale difference between the power and thermal systems. Unlike the power system with fast dynamics, the response of the thermal subsystem is slower due to larger thermal inertia and its optimization often requires a long prediction/planning horizon. While the predictive information such as vehicle speed and traction power demand can be accurately predicted over a short time horizon, longer horizon prediction for thermal management using V2X information is subject to greater uncertainties. Hence, an iPTM system is necessary that 1) can capitalize on the connectivity technology to improve the energy efficiency and 2) be able to handle the uncertainties in the long horizon vehicle speed and traffic events predictions. Moreover, real-time implementation requirements dictate that simple models are used onboard to predict the thermal dynamics and loads over a long prediction horizon. To this end, Hierarchical Model Predictive Control (H-MPC) [23, 24] can be a promising control framework to handle the challenge. H-MPC allows for simultaneous planning of thermal trajectories over a long horizon, and steering the system states toward the planned trajectories over a short horizon. Recent H-MPC developments include the applications to microgrids [25, 26], power flow systems [27], chemical plants [28], and building energy management system.

In this dissertation, the hierarchical optimization framework will be explored for the iPTM of the CAVs, focusing on demonstrating the benefits of incorporating predictive information for efficient climate control system. The proposed H-MPC strategy would allow potential control integration between other thermal subsystems with the powertrain, such as the engine thermal management [29] and battery thermal management [30, 31].

1.2 Automotive Climate Control System

Among all vehicle thermal subsystems, the climate control system, which performs the Heating Ventilation and Air Conditioning (HVAC) functions for the passenger compartment, usually represent the most significant auxiliary loads, especially for light-duty vehicles. It has been estimated that, in the United States, about 7 billion gallons of fuel is consumed per year just to power the air conditioning (A/C) system for light-duty vehicles [32]. A study performed at Argonne National Lab showed a 53.7% reduction in vehicle driving range due to air conditioning and 59.3% reduction in vehicle driving range due to heating for Ford Focus EV, tested over the Urban Dynamometer Driving Schedule (UDDS) [33]. Similarly, a significant reduction of driving range was also reported for Nissan Leaf [33] and in a recent work by National Renewable Energy Lab [34]. Aim at developing more efficient energy management strategies for the climate control system, the Air Conditioning (A/C) system in electrified powertrain is studied first, as electrified vehicle becomes more popular recently.

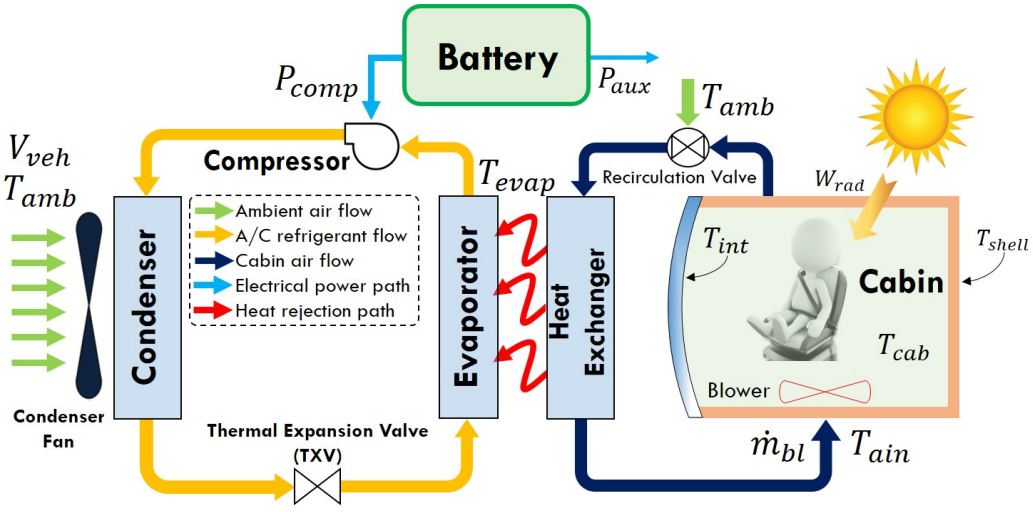

Figure 1.1: Schematic of the A/C system in an electrified powertrain.

Fig. 1.1 provides a schematic of a typical A/C system in an electrified powertrain in which an onboard battery supplies the power to the major power consumers in the A/C

system, namely, the compressor (P_{comp}) and the other auxiliaries (P_{aux}) including the condenser fan and the blower. There are two major loops of flow in the A/C system, the Refrigerant Loop (RL) shown in yellow lines and the Cabin Air Loop (CAL) shown in blue lines. In practice, depending on the cooling power demand from the CAL, the actuators in the RL including the compressor, the condenser fan, and the thermal expansion valve, etc., are coordinated to maintain the evaporator wall temperature (T_{evap}) within the desired and safe range. The variables V_{veh}, T_{amb}, T_{shell} represent the vehicle speed, ambient air temperature, and cabin shell temperature, respectively.

In the literature, the A/C energy management for the vehicle with traditional Internal Combustion Engine (ICE) [35, 36, 37] have been studied, where the A/C compressor is belt-driven by the ICE. However, as vehicle power sources are becoming more electrically dominant, their energy management requires different strategies than those used for vehicles with traditional ICEs. Regarding the A/C energy management for electrified powertrain, previous works [21, 38, 39, 40] have exploited the sensitivity of A/C system efficiency to vehicle speed and vehicle speed preview for reducing energy consumption. The energy saving potentials have been demonstrated based on two high-fidelity simulation models of the electrified A/C systems, CoolSim and ACSim, over various driving cycles.

In general, the objective of A/C energy management is minimizing the energy consumption while maintaining the Occupant Thermal Comfort (OTC) within the comfort constraint. Uncomfortable cabin thermal conditions can increase the stress for the vehicle passengers, thereby inducing higher chances of traffic accidents [41]. However, there is no universal approach quantifying the comfort constraint, especially for automotive HVAC applications. Previous work regarding automotive A/C energy management strategy development in [21, 38, 39, 40] uses the average cabin air temperature (T_{cab}) as the comfort metric and focuses on constraining T_{cab} within prescribed constraints. But, this comfort metric cannot represent the OTC in practice considering the special features in automotive climate control system[42]. In a passenger vehicle, occupants sit close to the vents and di-

rectly feel the temperature and the amount of air flow, and are exposed to the solar radiation directly. Therefore, the occupants thermal sensation is not directly correlated to T_{cab}.

Referring to the schematic shown in Fig. 1.1, there are many variables within the CAL that will influence the OTC such as the average cabin air temperature (T_{cab}), the cabin interior (e.g., seats and panels) temperature (T_{int}), the vent air temperature (T_{ain}), the air flow rate ($\dot{m}_{bl}$), and the solar radiation (W_{rad}) [42]. A thorough review on indoor thermal comfort modeling can be found in [43]. In the review, the thermal comfort models are categorized into three groups, empirical model, thermal-physiological model, and adaptive model. Considering the modeling complexity and detailed model structure, the empirical model can be applied for the real-time control design. Comfort-based design has been widely studied for building HVAC applications [43, 44, 45, 46]. More recently, such control design attracts more and more attentions in automotive applications [47, 48, 49, 50, 51].

In summary, the Combined Energy and Comfort Optimization (CECO) in a connected environment is not fully-explored regarding automotive HVAC control system and the literature addressing predictive thermal management in the vehicle system is very limited. Additionally, the study of the interactions between thermal management and power management systems for electrified vehicles would also require dedicated efforts. More importantly, how to implement the advanced iPTM strategy on vehicles and demonstrate the benefits remain to be open questions. This dissertation is dedicated to seeking partial answers to these questions. In particular, we are focusing on discovering the dynamic coupling between the thermal and power systems, leveraging the special characteristics of the automotive HVAC system to facilitate the iPTM design, developing real-time implementable algorithms to perform the energy and comfort optimizations, and demonstrating the energy saving benefits on the test vehicle.

1.3 Dissertation Work Scope and Contributions

In this dissertation, aiming at addressing the challenges and issues discussed in previous two sections, the contributions are two-fold regarding the developments of MPC-based A/C system management for electrified vehicles.

The first contribution is the modeling and analysis of the A/C system:

- Two high-fidelity simulation models (CoolSim and ACSim) are developed and used as the virtual testbeds for the developments and evaluations of different A/C management strategies. Through the studies of the two models, the vehicle speed sensitivity of the A/C system efficiency has been discovered, which is one of the key ideas for improving the system energy efficiency. The vehicle-level impact of A/C system operation has been identified and analyzed in both simulations and vehicle experiments.

- Control-oriented modeling is performed to support the predictive control designs. For developing MPC-based control strategies, simpler control-oriented models are required for providing reasonably accurate predictions of the A/C system behaviors. Two different control-oriented models have been proposed and validated for the corresponding simulation models. And motivated by the studies on the high-fidelity simulation models, a control-oriented model for the onboard A/C system of the testing vehicle is developed and validated against the experimental data as well.

The second contribution is the development of three novel MPC-based A/C energy management strategies: the hierarchical optimization, the Precision Cooling Strategy (PCS), and the combined energy and comfort optimization (CECO). All of them leverage predictive information for improving the energy and comfort management of the A/C system. They can be differentiated by their OTC assumptions, robustness considerations, and implementation complexities on the testing vehicle.

- The development of a hierarchical optimization framework for the A/C energy management and integration with powertrain system: in the hierarchical optimization, a

two-layer H-MPC control scheme is exploited for potential integration between the A/C and powertrain systems of an HEV. The main reason for developing such hierarchical structure is to handle the timescale difference between power and thermal systems as well as the uncertainties associated with long prediction horizon. The H-MPC is developed and evaluated based on the CoolSim model. Comprehensive simulation results over different driving cycles have been performed to demonstrate the energy saving potentials of efficient A/C energy management. In addition, the impact of uncertain speed preview is also demonstrated. In terms of the comfort metric, the average cabin air temperature is applied.

- The PCS and experimental validation of an eco-cooling strategy: in terms of MPC structure, PCS utilizes a simpler single-layer MPC assuming accurate predictive information over the prediction horizon. It is focusing on formulating a more practical OTC metric and the implementation on the testing vehicle. Specifically, the PCS has the simplest control-oriented model structure and its benefits are validated based on the ACSim model. The proposed PCS exploited a simpler yet more practical comfort metric, DACP, which directly motivates the design of an off-line eco-cooling strategy that can be easily implemented on the testing vehicle for demonstrating energy saving benefit.

- The development of CECO strategy: the CECO strategy considers a comprehensive OTC model, PMV, and combines the energy and comfort optimizations simultaneously while explicitly leveraging both traffic and weather predictive information. The CECO strategy demonstrates additional energy saving and comfort improvement opportunities.

1.4 Dissertation Outline

This dissertation reports the comprehensive research efforts on the MPC applications to the automotive climate control system, which leverage predictive information enabled by emerging CAV technologies. The energy and comfort benefits of applying the proposed MPC-based strategies are demonstrated in both simulations and vehicle experiments.

Chapter 1 provides an introduction on the CAV research and automotive climate control system, highlighting the opportunities and challenges in efficient vehicle thermal management and the integration with the power management.

Chapter 2 introduces the two high-fidelity simulation models for the electrified A/C system, which are used for the design and evaluation purposes throughout this dissertation. The speed sensitivities of the A/C system efficiency for both models are studied and the basic idea for energy efficient A/C operation, eco-cooling, will be presented.

Chapter 3 presents the development of a hierarchical two-layer MPC scheme which exploits vehicle speed and traffic preview predictions over short and long prediction horizons for efficient A/C system energy management with uncertain predictive information. The proposed A/C energy management scheme is then integrated with the powertrain model of a power-split HEV for evaluating the impacts on vehicle-level energy consumption. The energy saving benefits are demonstrated based on the simulations over various driving cycles when comparing with a single-layer MPC results for the temperature tracking control.

In **Chapter 4**, the PCS is presented by incorporating a more practical comfort metric, DACP. The proposed PCS is able to provide precise tracking of the DACP trajectory, which is assumed to meet the passenger comfort requirements. The PCS is developed and evaluated based on an industrial-level A/C system model, ACSim, and the energy benefits are demonstrated versus a baseline controller from Original Equipment Manufacturer (OEM) calibration. It is also demonstrated that by coordinating with future vehicle speed and shifting the A/C power load, the A/C energy consumption can be further reduced.

Directly motivated by the PCS development, in **Chapter 5**, an off-line eco-cooling

strategy is formulated by solving an optimal control problem based on the control-oriented model validated for the testing vehicle. In order to make fair comparisons, repeatable vehicle test of the eco-cooling strategy is carefully designed and the vehicle-level energy saving is confirmed based on the results from 18 sets of vehicle tests.

Chapter 6 considers incorporating a more comprehensive OTC model, PMV, into the energy optimization of the A/C system. The resulting CECO-based strategies show that additional energy saving can be achieved by avoiding the over-cooling while at the same improving the OTC level, compared with conventional cabin temperature tracking strategy. This is beyond the efficient operations exploited in previous chapters by leveraging the vehicle speed sensitivity of the A/C system efficiency.

Chapter 7 draws the conclusions and provide insights on future working directions.

CHAPTER 2

A/C System Speed Sensitivity and Eco-cooling

In this chapter, two high-fidelity A/C simulation models, CoolSim and ACSim, are introduced, which is utilized for the design and evaluation purposes of the proposed control strategies developed in this dissertation. Specifically, CoolSim is used in the developments of the hierarchical optimization and the CECO strategies, while the ACSim model is used in the development of the PCS. Although these two models are developed by different organizations, CoolSim by National Renewable Energy Lab (NREL) and ACSim by Ford Motor Company, they all simulate the behaviors of the electrified A/C system. More importantly, the speed sensitivity of the A/C system efficiency has been discovered and validated in both simulation models. Such speed sensitivity will be exploited repeatedly in simulations and experiments for the rest of this dissertation.

2.1 CoolSim Model and Speed Sensitivity Analysis

CoolSim is an open-source A/C system model available from the NREL, see [52]. Fig. 2.1 shows the schematics of the Simulink® model of the A/C system in CoolSim. The boundary conditions block specifies the speed profiles and ambient conditions such as temperature and pressure; Within the refrigerant loop (RL), the cooling circuit sub-models consists of detailed models of the evaporator, condenser, condenser fan, evaporator valve, and connecting pipes, while, the compressor block, as the primary energy consumer in the A/C system, is modeled separately from the cooling circuit; the cabin air loop (CAL) models the thermal dynamics of the cabin; the control inputs block lists the most important controls of the A/C system, including the cabin air flow rate, evaporator wall temperature set-point, and recirculation rate. See [52] for the modeling details of each subcomponent. This model is capable of simulating cycle-by-cycle behavior of the A/C system, and has been validated versus experimental data. While both electric-driven and belt-driven compressor configurations are available, the electric-driven one is considered for the development in this dissertation.

The nominal controller implemented in this model consists of two Proportional-plus-Integral (PI) control loops with anti-windup and A/C on-off logic. One of the PI loops adjusts the compressor speed for tracking the evaporator wall temperature set-point. The other PI loop regulates the blower speed in order to track the cabin air temperature set-point. The recirculation rate of the cabin air depends proportionally on the difference between the cabin air temperature and the ambient temperature and is saturated according to physical feasible limits. Fig. 2.2 gives an example of the system responses at different vehicle speeds with the nominal controller. The simulation is performed for a time period of 600 sec at different constant vehicle speeds (V_{veh} = 0, 5, 10, 15, 20, and 25 m/s) and for the same target cabin air temperature set-point. The simulation results of the CoolSim model indicate that the efficiency of the A/C system increases as the vehicle speed increases. This observation is consistent with the underlying physics, as the effective ram air speed through

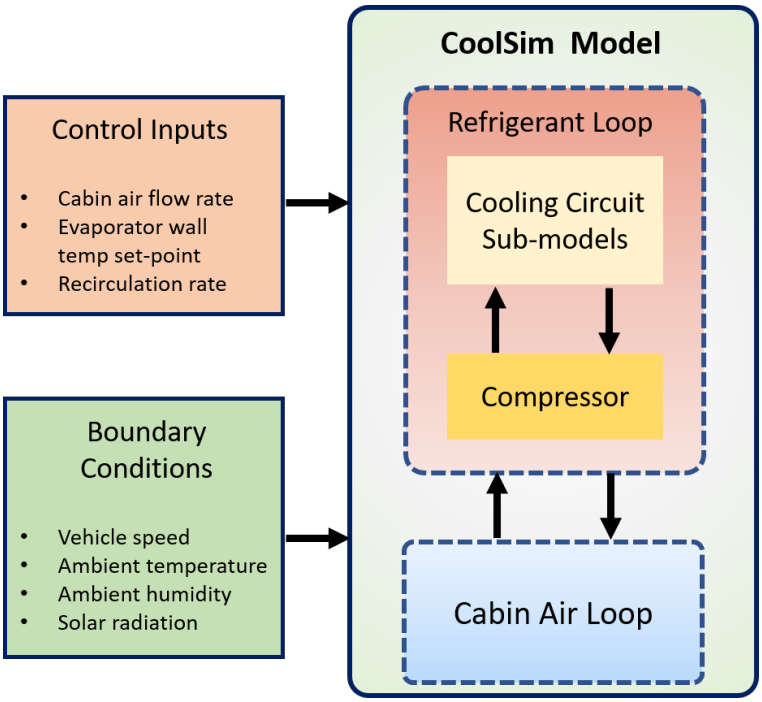

Figure 2.1: Schematic of the CoolSim model.

the condenser increases as vehicle speed increases, so that the condenser dissipates the heat faster, which leads to higher overall efficiency for the A/C system. Similar conclusion is reached in [53]. Table 2.1 summarizes the total energy consumption over the simulation run for different cases shown in Fig. 2.2. According to the values listed in the second row of Table 2.1, the efficiency of the A/C system increases by approximately 30% as the vehicle speed increases from 0 m/s (stop condition) to 25 m/s. The sensitivity to vehicle speed is even more pronounced if considering energy consumption normalized by the traveling distance (see the last row of Table 2.1). A vehicle traveling at higher speed spends less time to cover the same distance, reducing the A/C operating time and thus the associated energy consumption. This speed sensitivity can be exploited in the A/C predictive controller design. To put the numbers in Table 2.1 in perspective, we note that the A/C energy consumption is about a third of traction power in city driving.

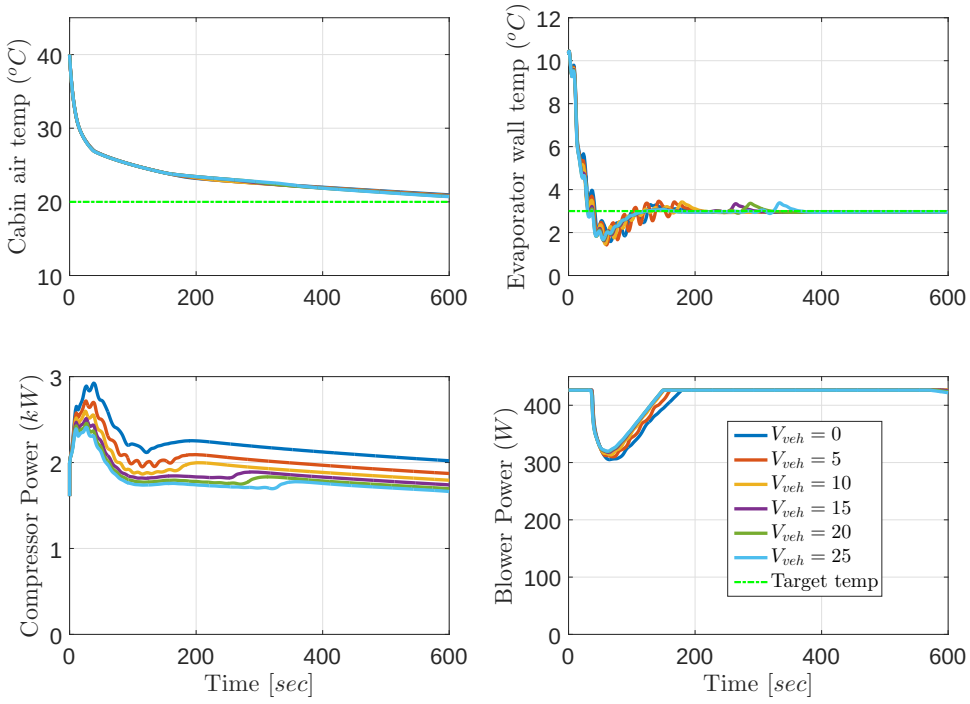

Figure 2.2: Vehicle speed sensitivity demonstrated on CoolSim model.

Table 2.1: Energy consumption for each case in the speed sensitivity test in Fig. 2.2.

Vehicle Speed (m/s)	0	5	10	15	20	25
Energy Consumption (MJ)	1.33	1.23	1.17	1.13	1.10	1.07
Energy Consumption (MJ/km)	NA	0.410	0.195	0.126	0.092	0.071

2.2 ACSim Model and Speed Sensitivity Analysis

ACSim is another high-fidelity model for the electrified A/C system, which is developed at Ford Motor Company. General system schematics are illustrated in Fig. 2.3. This model simulates the entire A/C system for a passenger car and is integrated with the controller module which represents two levels of controls. A higher-level controller is inside the climate control panel block, and it reflects the control settings (e.g. blower level and temper-

ature set-point) from the real vehicle, which directly affect the occupant thermal comfort. Lower-level controllers take the command from the control panel and regulate the behaviors of the physical system via the electric compressor control and the front end air flow control. Boundary conditions are set according to different simulation requirements. This model has been validated versus the data from production vehicle.

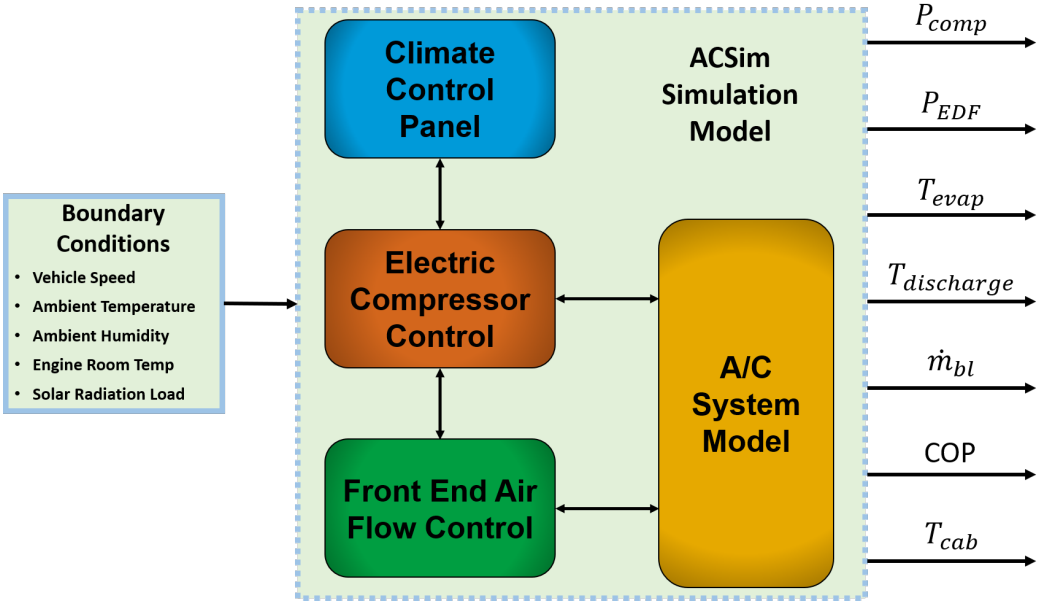

Figure 2.3: Schematics of ACSim simulation model

Next, the same speed sensitivity tests as presented in previous section are performed on the ACSim model. Fig. 2.4 summarizes the total A/C energy consumption ($E_{tot} = E_{comp} + E_{EDF}$, where E_{comp} and E_{EDF} represent the energy consumed by the compressor and the Electric Ducted Fan (EDF), respectively) for each case with different constant speed. Index values from 1 to 10 correspond to constant vehicle speed values from $0\ m/s$ to $25\ m/s$ (equally spaced), respectively. As the simulation results show, the total A/C energy consumption is reduced by 13.6% comparing case 10 with case 1, while the cooling performance is kept the same. This observation is consistent with the findings presented on CoolSim model.

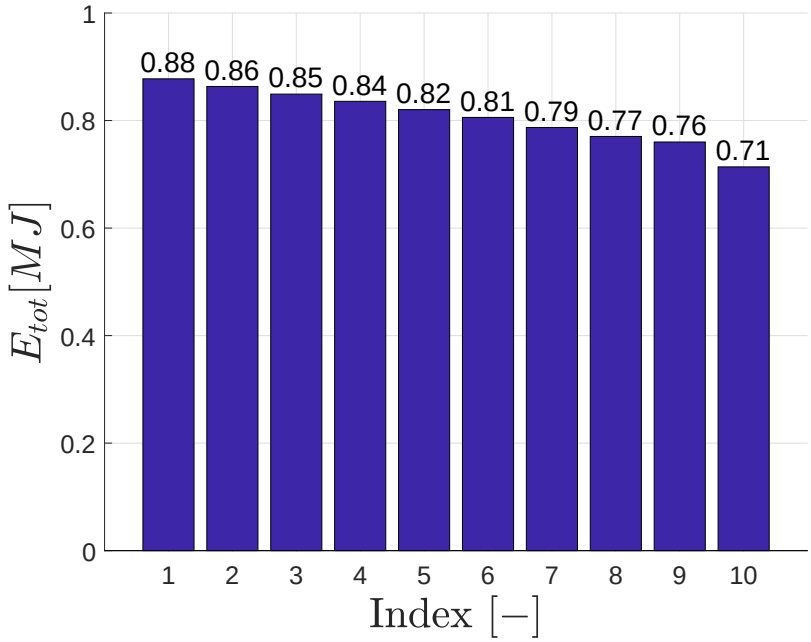

Figure 2.4: Total A/C energy consumption decreases as vehicle speed increases.

2.3 Eco-cooling Idea for Energy Saving

Since the speed sensitivity of the A/C system efficiency has been confirmed based the two high-fidelity simulation models, the basic eco-cooling idea can be illustrated in Fig. 2.5 by leveraging such speed sensitivity. The energy consumption of the A/C system can be reduced by manipulating the A/C operation with respect to the speed preview information when compared with constant A/C operation, i.e., cooling the cabin more when vehicle is at high speed and A/C is more efficient, and cooling the cabin less when vehicle is at low speed and A/C is less efficient. Based on this eco-cooling idea, detailed development on quantifying the A/C operation and maintaining corresponding comfort constraint is pursued subsequently in this dissertation.

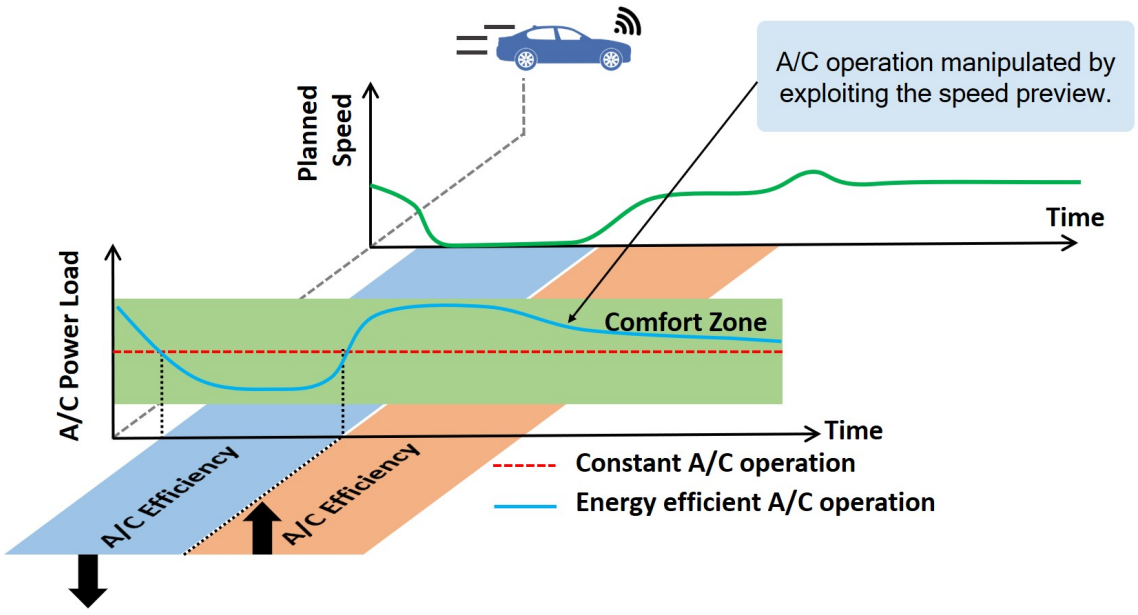

Figure 2.5: Illustration of eco-cooling idea in CAV.

CHAPTER 3

Hierarchical Optimization for Efficient A/C Energy Management

Incorporating traffic information in power management optimization process for electrified and connected vehicles offers opportunities for improving fuel economy. Integrating the management of thermal load with the power management process can provide even greater benefits for connected and automated vehicles (CAVs). However, given the relatively slow dynamics associated with the thermal subsystems, the lack of reliable power and thermal loads prediction over an extended prediction horizon increases the difficulty for efficient thermal management using Model Predictive Control (MPC). Aiming at handling the time-scale difference between the thermal and power systems and uncertainties in vehicle speed prediction, a hierarchical two-layer MPC scheme is proposed in this chapter, which exploits layers of future traffic events with different prediction accuracies over short and long prediction horizons to schedule optimal thermal trajectories. The proposed strategy is developed and evaluated based on high-fidelity simulation models. Vehicle energy saving potentials via efficient A/C energy management is demonstrated over different driving cycles.

3.1 Control-oriented Model Development for CoolSim

3.1.1 Predictive Model Structure

The detailed physical modeling of this A/C system and especially the modeling of the RL shown in Fig.1.1 is complicated [54]. In order to validate the control design, a control-oriented model for the dynamics of A/C system, which will be used as a prediction model in the implementation of MPC, is described in this section. This prediction model is motivated by physics [55] and is based on a similar approach as for building HVAC systems (see [56], and [57]). The model is discrete-time, has two states (T_{cab} and T_{evap}), and has the form,

$$\begin{aligned} T_{cab}(k+1) &= f_{T_{cab}}(k) = T_{cab}(k) + \gamma_1(T_{int}(k) - T_{cab}(k)) \\ &+ \gamma_2(T_{shell}(k) - T_{cab}(k)) \\ &+ \gamma_3(T_{ain}(k) - T_{cab}(k))\dot{m}_{bl}(k) + \tau_1, \end{aligned} \tag{3.1}$$

$$\begin{aligned} T_{evap}(k+1) &= f_{T_{evap}}(k) = \gamma_4 T_{evap}(k) \\ &+ \gamma_5(T_{evap}(k) - T^{s.p.}_{evap}(k)) + \tau_2, \end{aligned} \tag{3.2}$$

$$T_{ain}(k) = \gamma_6 T_{evap}(k) + \gamma_7 \dot{m}_{bl}(k) + \tau_3. \tag{3.3}$$

In Eqns. (3.1)-(3.3), T_{cab}, T_{int}, T_{shell}, T_{evap}, and T_{ain} represent the temperatures (in K) of the cabin air, the cabin interior (e.g. seats and panels), the cabin shell, the evaporator wall and the cabin inlet air flow, respectively. The control inputs to the model are $\dot{m}_{bl}$ (blower flow rate in kg/s) and $T_{evap,set}$ (evaporator wall temperature set-point in K). The model parameters, γ_i $(i = 1, 2, ..., 7)$ and τ_j $(j = 1, 2, 3)$ are identified from CoolSim model. Note that the model given by Eqns. (4.2)-(4.4) is nonlinear due to a bilinear term in Eqn. (4.2). The structure of the model reflects the following assumptions:

1. The recirculation rate of the cabin air (α_{recirc}) is constant ($\alpha_{recirc} \in [0\ 1]$, where $\alpha_{recirc} = 0$ means cabin inlet air is all from ambient while $\alpha_{recirc} = 1$ means all cabin air is recirculated via A/C system).

2. The dynamics of T_{int} and T_{shell} are slower than the dynamics of T_{cab} and T_{evap}. Thus, T_{int} and T_{shell} are treated as measured inputs.

3. The sensitivity of the states to vehicle speed is not reflected in the prediction model; accounting for this sensitivity is left to future research.

4. Blower dynamics can be ignored because of its small time constant.

3.1.2 Model Identification and Validation

Next, the outputs from the CoolSim model excited with random input signals are sampled at 0.2Hz to generate data for identifying the unknown parameters in Eqns. (4.2)-(4.4). The resulting identified parameters are

$$\gamma = [\gamma_1\ \gamma_2\ ...\ \gamma_7] = [0.2451\ 0.0867\ 1.2999\ 1.0047\ -0.5176\ 0.4553\ 34.9579]\,, \quad (3.4)$$

$$\tau = [\tau_1\ \tau_2\ \tau_3] = [-0.1842\ -1.3226\ 154.4995]\,. \quad (3.5)$$

Fig. 3.1 shows the validation results of the control-oriented model, which predicts the system behaviors over 300 steps into the future ($1500\ sec$) given the measurements only at the initial time step. T_{int} and T_{shell}, which are external inputs to the model, are assumed to be constant over the prediction horizon. By comparing the behavior of the control-oriented model with the high fidelity CoolSim model in Fig. 3.1, it can be seen that the identified model (Eqns. (4.2)-(4.4)) provides reasonably accurate results.

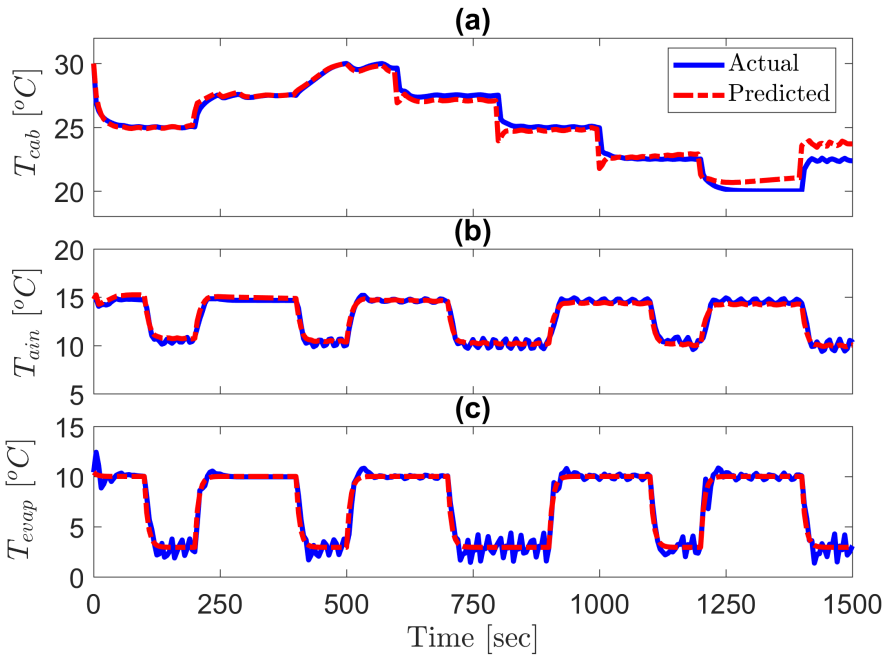

Figure 3.1: Model predictions initialized at a specific time point.

3.2 Problem Formulation of the Hierarchical Optimization

In this section, we will present the detailed problem formulations of the two-layer H-MPC, which represents the hierarchical optimization for efficient A/C energy management and potential integration with powertrain system control. For comparison purpose, a simpler single-layer MPC is also formulated. For both control schemes, since the primary objective is to minimize the energy consumption of the A/C system, accurate predictions in A/C power consumption become important. Two major energy consumers in the A/C system are the compressor and the blower. According to [56], their consumed powers can be

estimated by:

$$\begin{aligned} P_{comp}(k) &= \frac{c_p}{COP}\dot{m}_{bl}(k)(T_{amb} - T_{ain}(k)), \\ &= \frac{c_p}{COP}\dot{m}_{bl}(k)(T_{amb} - \gamma_6 T_{evap}(k) - \gamma_7 \dot{m}_{bl}(k) - \tau_3), \qquad (3.6) \\ P_{bl}(k) &= \beta_1 \dot{m}_{bl}^2(k) + \beta_2 \dot{m}_{bl}(k) + \beta_3, \qquad (3.7) \end{aligned}$$

where P_{comp} and P_{bl} represent the powers of the compressor and blower (in W), respectively, c_p is the specific heat capacity of air at constant pressure, COP is the Coefficient of Performance (COP) of the A/C system [58], which is assumed to be constant for the case studies on CoolSim model and $[\beta_1\ \beta_2\ \beta_3] = [24156\ -1974.2\ 49.318]$ are the parameters identified from CoolSim data. These two power predictions will be utilized throughout the development of control schemes on CoolSim model.

3.2.1 Single-layer MPC Formulation

For comparing purposes, a single-layer MPC is formulated as follows,

$$\begin{aligned} \min_{\substack{T_{evap}^{s.p.}(\cdot|k) \\ \dot{m}_{bl}(\cdot|k)}} \quad & \sum_{i=0}^{N} \left\{ \begin{array}{l} P_{comp}(i|k) + P_{bl}(i|k) \\ +w_c(T_{cab}(i|k) - T_{cab}^{s.p.})^2 \end{array} \right\}, \\ \text{s.t.} \quad & T_{cab}(i+1|k) = f_{T_{cab}}(i|k),\ i = 0, \cdots, N, \\ & T_{evap}(i+1|k) = f_{T_{evap}}(i|k),\ i = 0, \cdots, N, \\ & T_{cab}^{LB} \le T_{cab}(i|k) \le T_{cab}^{UB},\ i = 0, \cdots, N, \qquad (3.8) \\ & T_{evap}^{LB} \le T_{evap}(i|k) \le T_{evap}^{UB},\ i = 0, \cdots, N, \\ & 0.05 \le \dot{m}_{bl}(i|k) \le 0.15\ kg/s,\ i = 0, \cdots, N-1, \\ & 3^oC \le T_{evap}^{s.p.}(i|k) \le 10^oC,\ i = 0, \cdots, N-1, \\ & T_{cab}(0|k) = T_{cab}(k),\ T_{evap}(0|k) = T_{evap}(k). \end{aligned}$$

In (3.8), N is the prediction horizon for the single-layer MPC, $(i|k)$ designates the prediction for the time instant $k+i$ made at the time instant k. The nonlinear MPC optimization problem (3.8) is formulated with two objectives represented by its cost function. One is to minimize the system energy consumption ($P_{comp} + P_{bl}$) and the other one is minimize the tracking error of the cabin temperature setpoint ($T_{cab}^{s.p.}$) that the passenger selects. Meanwhile state and input constraints are also enforced. The values of the state and input constraints in (3.8) are selected according to the operation limits of the CoolSim® model. The parameters T_{cab}^{UB} and T_{cab}^{LB} are the upper and lower limits on the cabin temperature, which is intended to define the comfort zone of the passenger. Furthermore, $T_{evap}^{UB} = 12^oC$ and $T_{evap}^{LB} = 0^oC$ are the upper and lower limits of the evaporator wall temperature. The weighing factors for tracking the cabin temperature setpoint is denoted by w_c. The functions $f_{T_{cab}}$ and $f_{T_{evap}}$ are used to represent the dynamics of T_{cab} and T_{evap} defined by Eqn. (3.1)-Eqn. (3.3).

To formulate a baseline case based on this single-layer MPC, the prediction horizon N is selected to be $30\ sec$ and w_c is selected to be a large positive number to guarantee the passenger comfort. While in the reminder of this section, this single-layer MPC is incorporated into a two-layer H-MPC design, which is further enhanced by incorporating traffic data to improve the overall system energy efficiency.

3.2.2 Two-layer H-MPC Formulation

The two-layer solution uses a scheduling layer MPC at the upper layer, and a piloting layer MPC at the lower layer. The scheduling layer MPC first calculates the optimal trajectories for the A/C system with respect to future traffic events. These scheduled trajectories are passed on to the piloting layer MPC to track these optimal trajectories. Given the relatively slow thermal dynamics of the cabin, a long prediction horizon is required to schedule the optimal cabin thermal trajectories. Consequently, the scheduling layer MPC is formulated over a long prediction horizon (H_l). On the other hand, to reduce the computation burden,

the piloting layer MPC is designed with a shorter prediction horizon (H_s) than the scheduling layer MPC. Moreover, the design of the piloting layer MPC can be simplified compared to (3.8), as the long horizon traffic information and system constraints are being included and handled at the scheduling layer MPC.

3.2.2.1 Scheduling Layer MPC with Long Horizon

The cost function of the scheduling layer MPC is based on several modifications of (3.8). In order to incorporate the future traffic information into the MPC design, a new variable, η_{AC}, is included to bring the sensitivity of the A/C system to vehicle speed into the optimization problem formulation. Namely, the cost function associated with the A/C system power consumption is defined as:

$$\ell_{power} = \frac{P_{comp}(i|k)}{\eta_{AC}(i|k)} + P_{bl}(i|k), \tag{3.9}$$

where, P_{comp} is calculated according to Eqn. (3.6). η_{AC} in Eqn. (3.9) is dependent on the vehicle speed forecast from the traffic data. When $V_{veh} = 0$, $\eta_{AC} = 1$. Once V_{veh} increases, η_{AC} will increase to reflect the increase in the A/C system efficiency at higher speeds.

Another term is incorporated in the running cost function of the scheduling layer AC MPC to reflect the objective of maintaining average cabin temperature at the setpoint ($T_{cab}^{s.p.}$):

$$\ell_{s.p.} = \left(T_{cab}^{s.p.} - \frac{\sum_{i=0}^{H_l} T_{cab(i|k)}}{H_l + 1}\right)^2, \tag{3.10}$$

where, $\sum_{i=0}^{H_l} T_{cab}(i|k)/(H_l + 1)$ is the average cabin temperature over the long prediction horizon H_l.

The design of the MPC is dictated by the trade-off between the passenger comfort and the system power consumption. To explicitly incorporate this design requirement, in addition to the physical control inputs of the A/C system ($\dot{m}_{bl},\ T_{evap}^{s.p.}$), a synthetic optimization

variable is required to determine the efficient trade-off between the A/C power consumption and the passenger comfort. According to Eqn. (3.9), the energy efficient operation of the A/C system is achieved if the upper limit of the cabin air temperature T_{cab}^{UB} is tracked by the controller. On the other side, according to Eqn. (3.10), the ideal case for the passenger comfort is to perfectly track the commanded temperature setpoint $T_{cab}^{s.p.}$. In order to leverage the A/C system sensitivity to the vehicle speed for improving the energy efficiency, it is beneficial to follow T_{cab}^{UB} during the vehicle stops, and put more effort to track $T_{cab}^{s.p.}$ during the high efficiency periods of the A/C system operation, i.e., high vehicle speeds. To this end, a third term is added to the running cost which is referred to as the Intelligent Online Constraint Handling (IOCH) term (L_{IOCH}):

$$L_{IOCH} = \frac{\eta_{AC}(i|k) - 1}{\epsilon(i|k) + \xi}, \tag{3.11}$$

where, $\xi > 0$ is a constant. ϵ is a new "slack" (synthetic) optimization variable, which is also used to update the upper limit of the cabin temperature comfort zone (T_{cab}^{UB}) as follows:

$$\tilde{T}_{cab}^{UB}(i|k) = T_{cab}^{UB}(i) - \epsilon(i|k). \tag{3.12}$$

L_{IOCH} defined in Eqn. (3.11) and the introduction of the slack variable lead to the following properties:

1. when $V_{veh} = 0$ and $\eta_{AC} = 1$, $L_{IOCH} = 0$.
2. when $V_{veh} \to 0$, $\epsilon \to 0$ and $T_{cab} \to T_{cab}^{UB}$.
3. when $\eta_{AC} > 1$, the upper bound of T_{cab} is tightened to make the AC system work harder when the AC system efficiency is higher.

Based on the above modifications, the scheduling layer MPC with traffic information incorporated and IOCH mechanism is based on the solution of the following optimization problem:

$$
\begin{aligned}
\min_{\substack{T^{s.p.}_{evap}(\cdot|k)\\ \dot{m}_{bl}(\cdot|k)\\ \epsilon(\cdot|k)}} \quad & \sum_{i=0}^{H_l} \left\{ \begin{array}{c} \dfrac{P_{comp}(i|k)}{\eta_{AC}(i|k)} + P_{bl}(i|k) + \beta\Big(\dfrac{\eta_{AC}(i)-1}{\epsilon(i|k)+\xi}\Big) \\ +\lambda\Big(T^{s.p.}_{cab}(i|k) - \dfrac{\sum_{i=0}^{H_l} T_{cab(i|k)}}{H_l+1}\Big)^2 \end{array} \right\}, \\
\text{s.t.} \quad & T_{cab}(i+1|k) = f_{T_{cab}}(i|k),\ i=0,\cdots,H_l, \\
& T_{evap}(i+1|k) = f_{T_{evap}}(i|k),\ i=0,\cdots,H_l, \\
& T^{LB}_{cab} \le T_{cab}(i|k) \le T^{UB}_{cab} - \epsilon(i|k),\ i=0,\cdots,H_l, \\
& T^{LB}_{evap} \le T_{evap}(i|k) \le T^{UB}_{evap},\ i=0,\cdots,H_l, \\
& 0.05 \le \dot{m}_{bl}(i|k) \le 0.15\ kg/s,\ i=0,\cdots,H_l-1, \\
& 3^oC \le T^{s.p.}_{evap}(i|k) \le 10^oC,\ i=0,\cdots,H_l-1, \\
& 0^oC \le \epsilon(i|k) \le 3^oC,\ i=0,\cdots,H_l-1, \\
& T_{cab}(0|k) = T_{cab}(k),\ T_{evap}(0|k) = T_{evap}(k),
\end{aligned}
\tag{3.13}
$$

where β and ξ are constant weighting factors to adjust the trade-off between A/C system energy consumption and cabin temperature setpoint tracking. Fig. 3.2 shows the results of implementing the A/C MPC with IOCH mechanism on the control-oriented model. The calculated $\epsilon(k)$ along with the driving cycle (UDDS) are plotted in Fig. 3.2-a. As expected $\epsilon(k)$ decreases to zero whenever V_{veh} decreases to zero. As can be observed from Fig. 3.2-b, T_{cab} follows the $\tilde{T}^{UB}_{cab} = T^{UB}_{cab} - \epsilon$, which exhibits the desired energy efficient cooling profile. Furthermore, Fig. 3.2-c verifies the desirable response of L_{IOCH} as a function of the vehicle speed (i.e., $L_{IOCH}(k)$ decreases to zero when $V_{veh}(k)$ decreases to zero).

3.2.2.2 Piloting Layer MPC with Short Horizon

The planned trajectory of $\tilde{T}^{UB}_{cab}(i|k) = T^{UB}_{cab} - \epsilon(i|k)$ from the scheduling layer MPC is next passed on to the piloting layer MPC, which is designed to track the scheduled trajectories. The piloting layer MPC is defined based on the solution of the following problem over a short horizon (H_s):

$$
\begin{aligned}
\min_{\substack{T^{s.p.}_{evap}(\cdot|k)\\ \dot{m}_{bl}(\cdot|k)}} \quad & \sum_{i=0}^{H_s} \left\{ \begin{array}{c} P_{comp}(i|k) + P_{bl}(i|k) \\ +w_c\Big(T_{cab}(i|k) - (T^{UB}_{cab}(i) - \epsilon(i|k))\Big)^2 \end{array} \right\}, \\
\text{s.t.} \quad & T_{cab}(i+1|k) = f_{T_{cab}}(i|k),\ i = 0, \cdots, H_s, \\
& T_{evap}(i+1|k) = f_{T_{evap}}(i|k),\ i = 0, \cdots, H_s, \\
& 0.05 \leq \dot{m}_{bl}(i|k) \leq 0.15\ kg/s,\ i = 0, \cdots, H_s - 1, \\
& 3^oC \leq T^{s.p.}_{evap}(i|k) \leq 10^oC,\ i = 0, \cdots, H_s - 1, \\
& T_{cab}(0|k) = T_{cab}(k),\ T_{evap}(0|k) = T_{evap}(k).
\end{aligned} \tag{3.14}
$$

As compared to the scheduling layer MPC (3.13), the piloting layer MPC has fewer optimization variables and constraints, a less complicated cost function, and a shorter prediction horizon ($H_l > H_s$). To reduce the fluctuation of the piloting layer MPC setpoint ($\tilde{T}^{UB}_{cab}$), the optimized values of ϵ from the scheduling layer MPC are quantized before being passed on to the piloting layer MPC. Specifically, in our implementation, ϵ is quantized at a quantization level of 0.5^oC. Fig. 3.2-a shows the actual $\epsilon(k) = \epsilon(0|k)$, and the quantized $\epsilon(k)$, which is passed on to the piloting layer MPC.

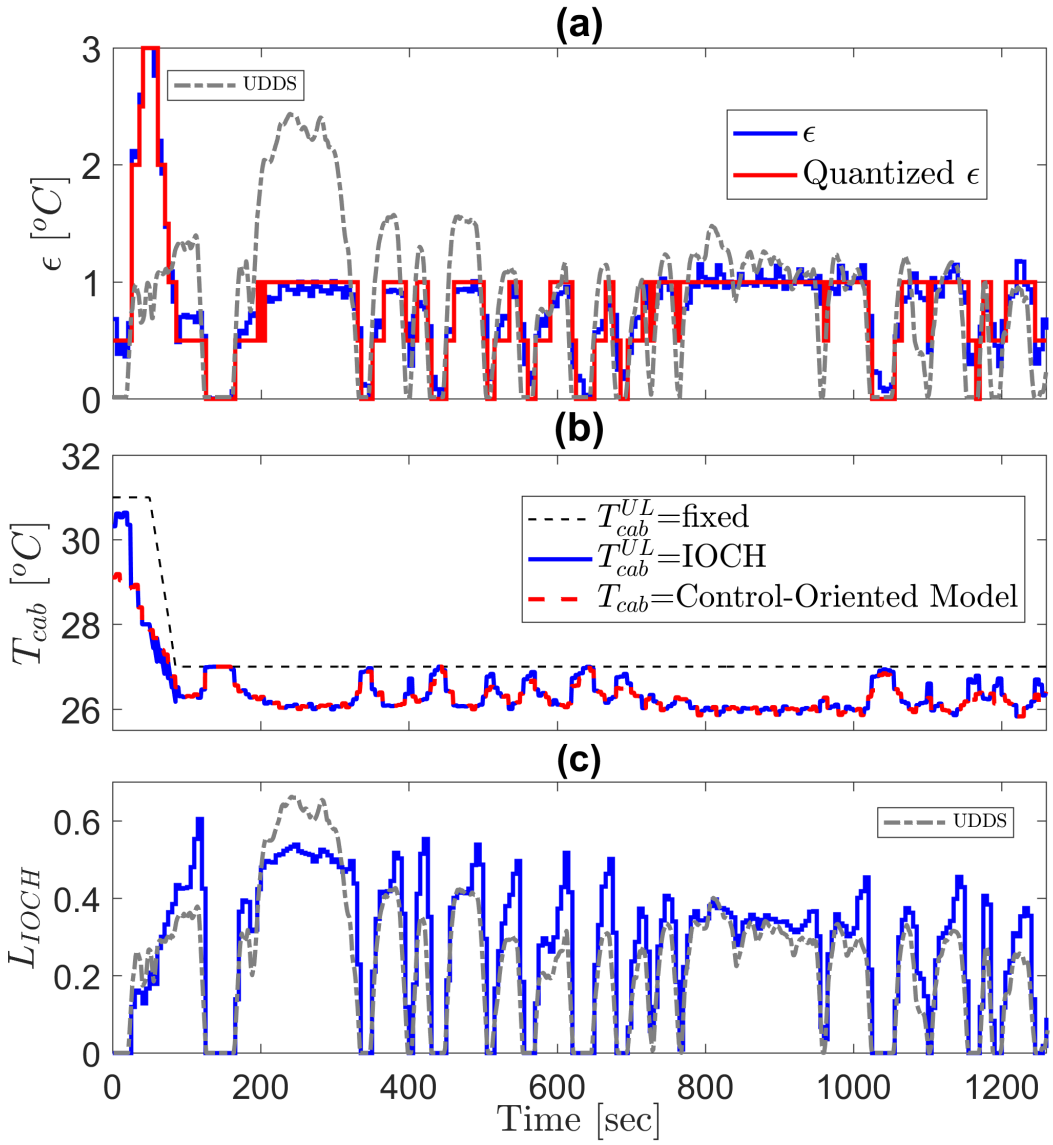

Figure 3.2: Intelligent online constraint handling (IOCH) performance for the UDDS (H_s= 6 (30 sec), and H_l=12 (60 sec).

3.2.2.3 Real-Time Implementation of the H-MPC

In order to validate the computational capability of the proposed two-layer hierarchical MPC for the A/C system, the controller is implemented on a rapid prototyping system using Speedgoat®, as an actual electronic control unit (ECU), with an Intel® Celeron Core processor. The physical set-up of the controller can be seen from Fig. 3.3.

The controller is implemented on the control-oriented model to avoid the additional

CPU	Intel Celeron 2 GHz 4 cores
Operating system	Simulink Real-Time™
Memory	4GB
Supported from MATLAB	2016a or newer
Main drive	32 GB SSD
Power supply	9-36 VDC Input Range with external adapter for AC 100-240V, 50/60 Hz

Figure 3.3: Speedgoat® controller and its configuration.

computation times required for simulating the high-fidelity CoolSim model. The MPC is simulated in MATLAB/SIMULINK® using C-code based S-functions, and the SQP algorithm [59, 60] has been used for solving the optimization problem numerically. The computation times incurred at the scheduling and piloting layers and corresponding to trajectories of the proposed two-layer MPC are plotted in Fig. 3.4 for the UDDS. The update rates of both MPCs are $5\ sec.$ As shown in Fig. 3.4, the piloting layer MPC with a short prediction horizon of $H_s = 6$ requires an average computation time of $0.558\ msec$, with maximum computation time of $2.9\ msec.$ At the same time, the scheduling layer MPC requires longer computation times, as it has more optimization variables and constraints with longer prediction horizon. The results in Fig. 3.4 show that the scheduling layer MPC with $H_l = 24$ requires an average computation time of $55.829\ msec.$ The scheduling and piloting layer MPCs run simultaneously, thereby the overall computation time of the two-layer MPC is dictated by the slower layer (scheduling layer) with the maximum computation time of up to $62\ msec.$ It can be observed that the computation times of the piloting and scheduling layer MPCs are well below the ECU update rate of $5000\ msec$, thereby confirming the computational feasibility of the hierarchical MPC for real-time implementation on an actual ECU.

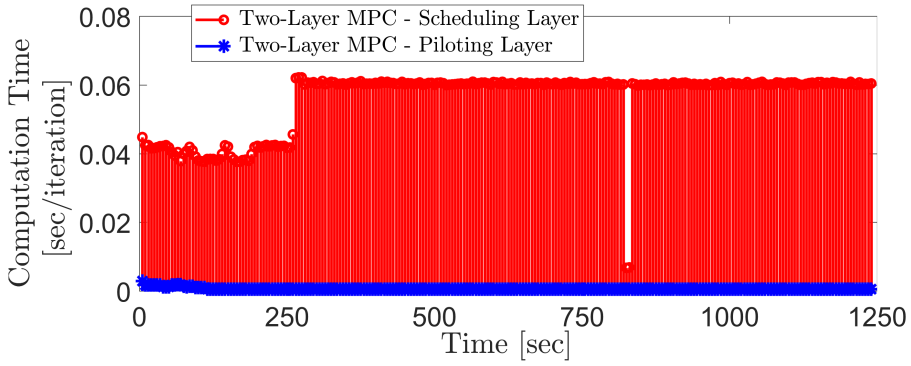

Figure 3.4: Real-time computation times of the scheduling and piloting layers MPC over UDDS with H_s= 6 (30 sec), and H_l=24 (120 sec) implemented on the Speedgoat.

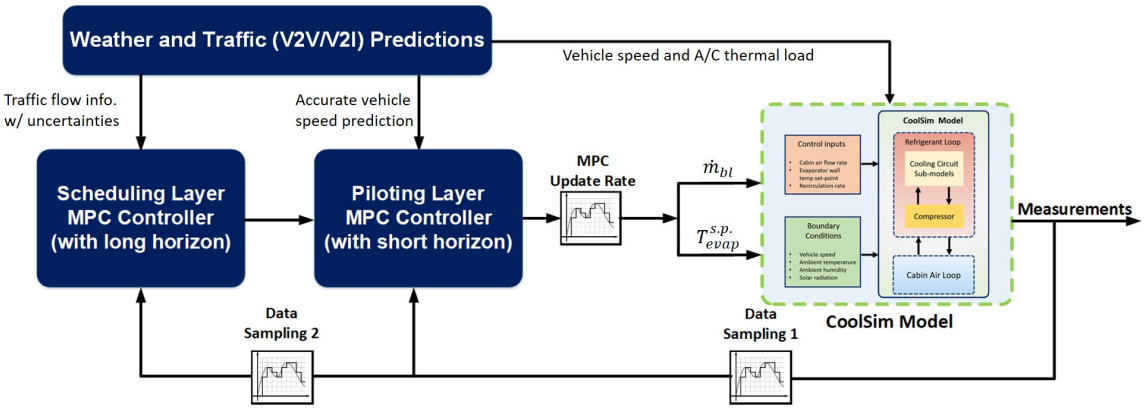

Figure 3.5: Overall schematic of the H-MPC implemented in closed-loop with CoolSim Model.

3.3 Simulation Results and Performance Evaluation

3.3.1 A/C Energy Saving Demonstrated on CoolSim Model

Fig. 3.5 shows the overall schematic of implementing the proposed two-layer H-MPC in closed-loop with the CoolSim model. While the hierarchical framework shown in Fig. 3.5 is generic and it allows for incorporation of weather forecast information, in this paper we assume that the ambient temperature and weather conditions are constant.

3.3.1.1 A/C load optimization and shift via IOCH mechanism

Fig. 3.6 presents the results of implementing the two-layer MPC for cabin thermal management and the decentralized MPC for BTM over UDDS on the high-fidelity thermal simulation models. For the hierarchical MPC in (3.13) and (3.14), the sampling time of $T = 5\ sec$ is considered at both layers. The passenger requests $T_{cab}^{s.p.} = 26^oC$. Assuming $SOC(0) = 95\%$, it can be observed that the single-layer MPC (3.8) consumes a considerable part of the battery energy (Fig. 3.6-d) for tracking $T_{cab}^{s.p.}$. On the other hand, according to the vehicle speed profile, the two-layer MPC schedules $\tilde{T}_{bat}^{UL}$ to reduce the load on the A/C compressor when V_{veh} decreases to zero (Fig. 3.6-a). In other words, the IOCH mechanism allows for shifting the A/C load from the inefficient periods, i.e., vehicle stops, to the high efficiency periods, i.e., high vehicle speeds. As shown in Fig. 3.6-d, the two-layer MPC is able to save 5.4% of the battery energy by taking proactive actions to minimize the cooling load on the A/C compressor during low efficiency periods of the A/C system operation.

The plotted results in Fig. 3.6-a show an average cabin temperature of 26^oC for the single-layer MPC, compared to the value of 26.5^oC for the two-layer MPC with IOCH. This means that 5.4% of the battery energy can be saved by allowing the average cabin temperature to rise by less than 2%. Figs. 3.6-b,c, and e show the compressor speed, A/C power demand ($P_{comp} + P_{bl}$), and the quantized ϵ calculated by the scheduling layer MPC.

3.3.1.2 Cabin air as a thermal storage

The relatively slow dynamics of the cabin air temperatures provide a unique opportunity to treat the cabin air as a "temporary" thermal storage. When a long stop duration is projected by the scheduling layer MPC along the prediction horizon, the controller plans to reduce the load on the A/C compressor. This means that when the vehicle comes to a complete stop, T_{cab} starts to rise. However, due to the slow dynamics of T_{cab}, it does not rise immediately, and it takes a while until T_{cab} reaches T_{cab}^{UB}. Thus, energy can be saved by shutting off

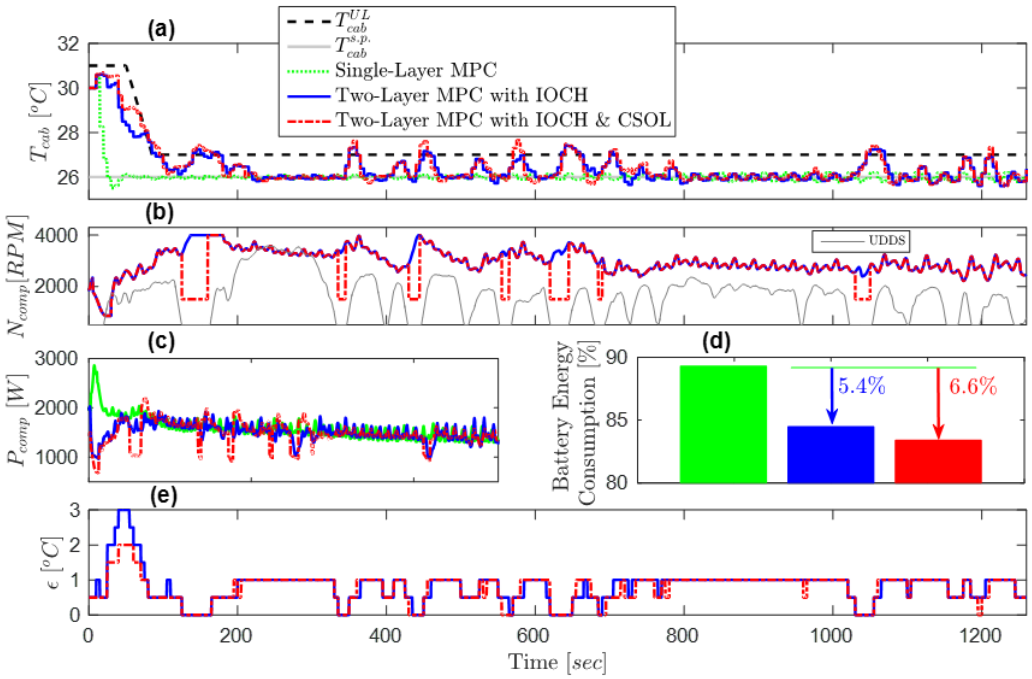

Figure 3.6: Overall performance of the two-layer MPC with IOCH mechanism for constant $T_{cab}^{s.p.}$ and UDDS (N_1=H_s= 6 (30 sec), and H_l=12 (60 sec)).

the compressor. When the vehicle starts to move again after a temporary stop, the A/C compressor can start to run to compensate for the rise in the cabin temperature.

3.3.1.3 Compressor shut off logic

In order to take advantage of the available "temporary" thermal storage within the cabin, we incorporate an add-on compressor shut off logic into the piloting layer MPC to increase the energy saving potential of the proposed two-layer MPC solution. Note that if the compressor is completely turned off during the vehicle stop period, T_{cab} may increase to even above T_{cab}^{UB}. Moreover, recovering the cabin temperature from beyond T_{cab}^{UB} to the comfort zone will increase the cooling load significantly, and such an increase may not be acceptable to the passengers. Thus, to minimize T_{cab}^{UB} constraint violation and avoid imposing unexpected cooling load on the A/C compressor, instead of completely turning the compressor off, the compressor shut off logic ($CSOL$) is introduced to reduce the compressor

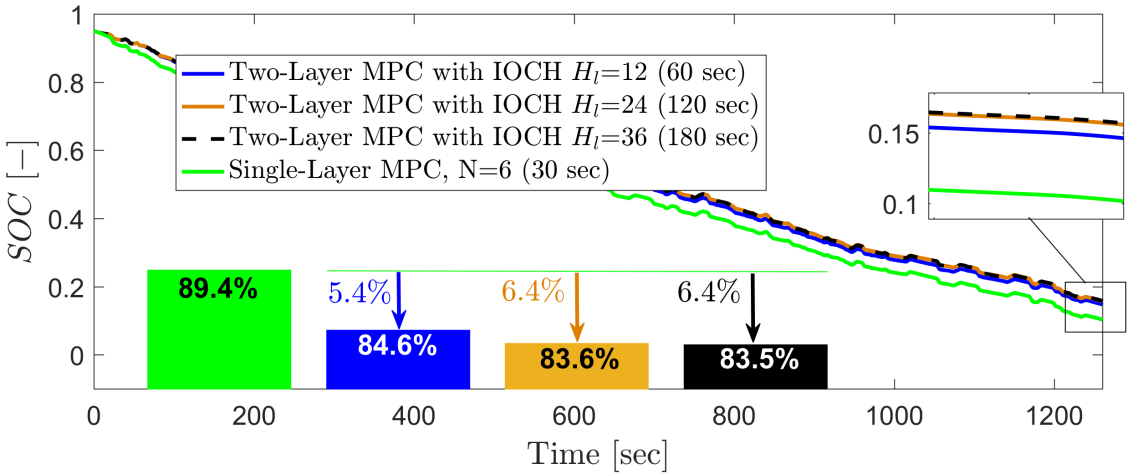

Figure 3.7: Effect of increasing the scheduling layer MPC prediction horizon (H_l) of the two-layer MPC on the battery energy consumption for UDDS. N_1=H_s=6 (30 sec).

speed to below 2000 RPM when the following conditions hold:

- $\epsilon(1|k) = \epsilon(2|k) = 0$
- $T_{cab} < T_{cab}^{UB} + \vartheta,\ 1 > \vartheta > 0\ ^oC$

The first criterion implies that CSOL could reduce the compressor speed if the vehicle has come to a complete stop for at least 10 sec. This condition is imposed to ignore no-significant vehicle stop events and minimize the transients in the compressor operation. The second condition guarantees that T_{cab} will not go beyond $T_{cab}^{UP} + \vartheta$ threshold, where ϑ is a small number (e.g., 0.5 ^oC).

The responses with the two-layer MPC and the add-on CSOL are also plotted in Fig. 3.6. It can be seen from Fig. 3.6-a that when CSOL conditions are fulfilled, T_{cab} increases slightly above T_{cab}^{UB}. At the same time, CSOL decreases the compressor speed (Fig. 3.6-b) at vehicle stops, which consequently reduces the AC system power consumption (Fig. 3.6-c). As shown in Fig. 3.6-d, the two-layer MPC equipped with IOCH and CSOL is able to save 6.6% of the battery energy at the end of the driving cycle, compared to the single-layer MPC.

3.3.1.4 Impact of the prediction horizon (H_l) length

The results in Fig. 3.6 are based on a scheduling MPC with $H_l = 12$ $(60\ sec)$. Fig. 3.7 shows that by increasing H_l from 12 to 36 $(180\ sec)$, the energy saving potential of the two-layer MPC with IOCH mechanism will increase from 5.4% to 6.4%. This is expected as increasing the prediction horizon makes more information available to the controller, and the output of the scheduling layer MPC is closer to the global optimal solution. However, there are two issues which complicate the implementation of the scheduling layer MPC with a long horizon. Firstly, the prediction of future traffic events over a long horizon (e.g., greater than $30\ sec$) is not reliable. Secondly, extending the prediction horizon may significantly increase the MPC computation effort, thereby making the real-time implementation of the controller more difficult. Sec. 3.3.2 addresses the solution to these issues.

3.3.2 Impact of Uncertainties in Vehicle Speed Prediction

As discussed in the previous section (Fig. 3.7), the information about future driving conditions, in particular, the vehicle speed profile over a long horizon, can facilitate the design of an energy-efficient A/C system. In this section, we highlight the opportunity to base an approximate knowledge of future vehicle speed profile on the average traffic flow velocity (V_{flow}) estimate following the approach proposed in [61]. This knowledge, when integrated into the two-layer MPC controller, can reduce energy consumption. While the knowledge of the exact demanded traction power over a short horizon is essential for the energy management of the HEVs, it will be shown in this section that even a very approximate knowledge of the traffic flow information over a long horizon can be beneficial for the cabin and battery thermal management.

In [61], the traffic flow data are extracted from a traffic monitoring system described in [62], based on GPS-enabled smart phones. This system exploits the extensive coverage of the cellular network, GPS-based position and velocity measurements, and the communication infrastructure of cellphones. Here, the traffic flow speed is calculated according to

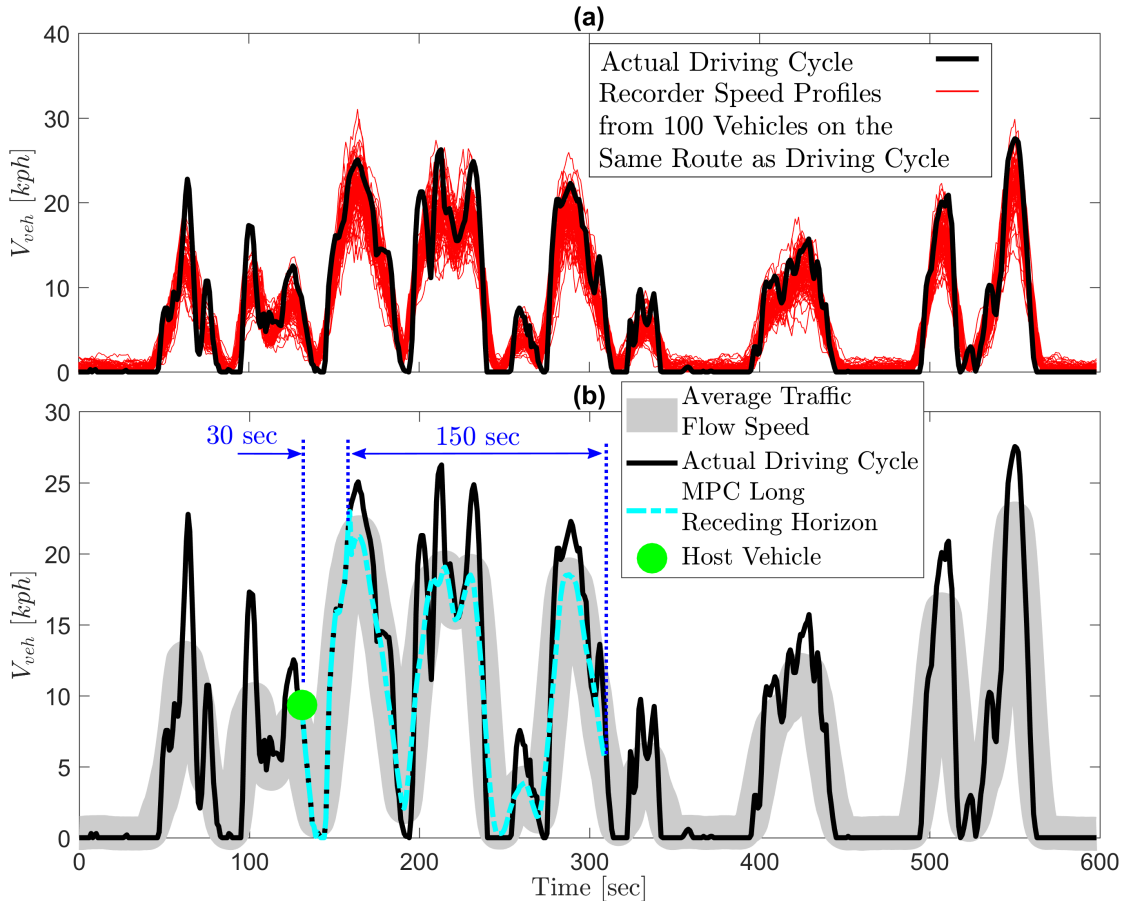

Figure 3.8: The average traffic flow speed estimate versus the actual speed over a driving cycle.

the moving average of the recorded speed trajectories of 100 vehicles traveling following the same route as the "host" vehicle over a moving time-window of $120 - 180$ sec. Not all of these vehicles are required to be on the same route as the host vehicle for the entire simulation time, instead the speed signals of the vehicles exiting the route are replaced by those entering the route, so that the traffic flow speed is estimated based on a large set of vehicles speed trajectories along the host vehicle route. With this approach it is possible to build a dynamic map of average traffic velocity over a long horizon.

In this paper, we assume that the vehicle speed can be accurately estimated over a 30-sec horizon according to V2V/V2I data, while for the rest of the long horizon, the average traffic flow information is used to predict the thermal loads. It is envisioned that

the traffic flow data are being collected, analyzed, and updated by a central/cloud server in real-time, and they are available to the vehicle control system at no extra computational cost. Additionally, V_{flow} is updated every 5 sec as the traffic flow changes downstream. Fig. 3.8 illustrates the concept of the average traffic flow speed trajectory and compares it against the actual speed profile. As can be observed from Fig. 3.8-b, over the long receding horizon of the MPC, the vehicle speed is accurately predicted for the first 30 sec. Then, the predicted vehicle speed merges into the average traffic flow speed band (the gray band in Fig. 3.8-b) over the long horizon.

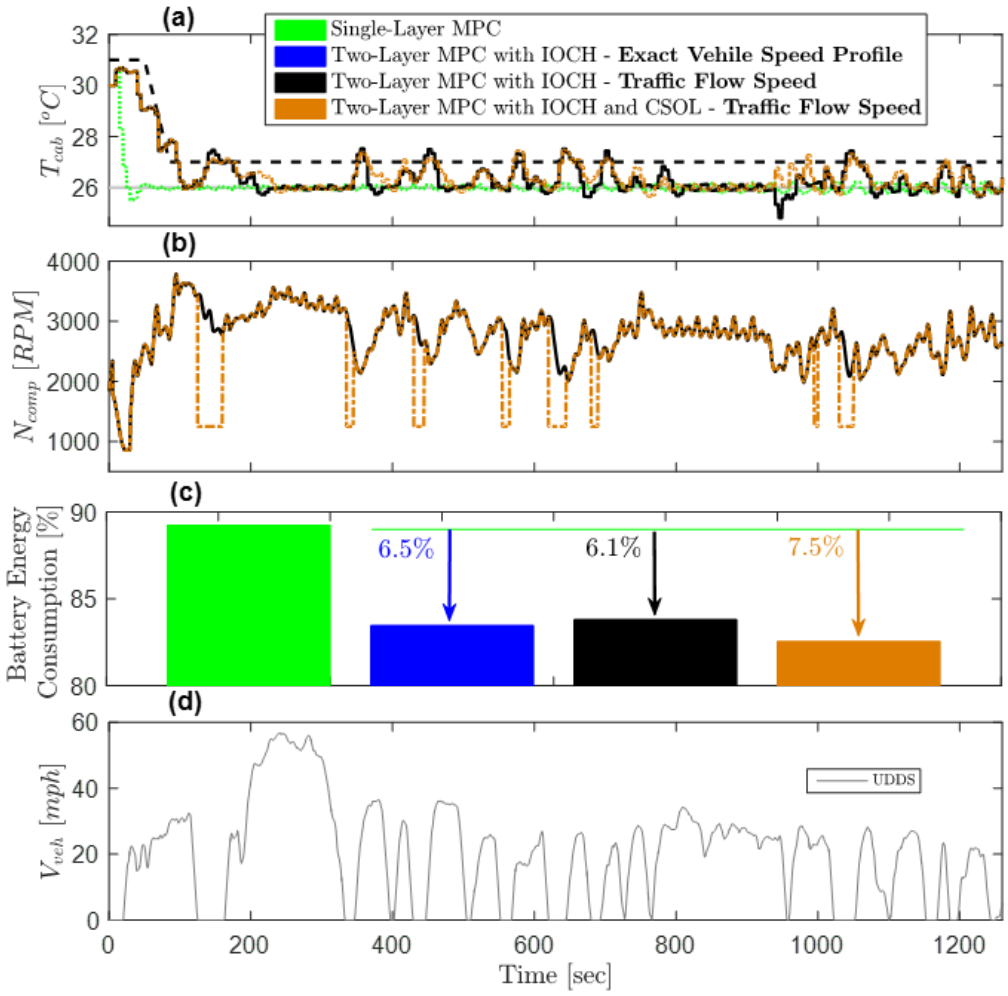

Figure 3.9: Overall performance of the two-layer MPC with IOCH mechanism with exact vehicle speed profile and with traffic flow speed information for the UDDS (N_1=H_s= 6 (30 sec), and H_l=24 (120 sec)).

Fig. 3.9 represents the results of testing the two-layer MPC with exact vehicle speed profile and estimated traffic flow speed information (Fig. 3.8) over the long prediction horizon. It was previously shown in Fig. 3.7 that increasing H_l from 24 to 36 does not considerably improve the energy saving results. Thus, to keep the computation time of the scheduling layer MPC as low as possible, the value of $H_l = 24$ (corresponding to a 120 sec time window) is selected. Compared with the two-layer MPC with exact vehicle speed profile, it is observed that the two-layer MPC with exact vehicle speed profile and traffic flow information results in similar cabin thermal management (Fig. 3.9-a), and that the energy saving results from the two-layer MPC with traffic flow information are still substantial (6.1% less battery energy consumed compared with the single-layer MPC). Furthermore, by inclusion of the CSOL in the two-layer MPC solution, the battery energy saving from the predictive controller with estimated vehicle speed from average traffic flow information over the long horizon is increased to 7.5%. Eventually, Fig. 3.9-d shows that the BTM results are similar for all studied cases, as the cabin temperature is the same. This is mainly due to the relatively slow thermal dynamics of the vehicle. As a consequence, only major events along the driving cycle will affect the thermal system behavior, and the proposed approach to traffic flow speed estimation is able to capture these major traffic events for the thermal management purpose.

3.3.3 Vehicle-level Implementation and Fuel Energy Saving

Previous simulation results were based on the assumption that the ICE power output is the same for all scenarios. In this section, the ICE is considered as an active source of power. To this end, the developed two-layer MPC in the previous sections is implemented at the vehicle level hybrid controller of the Prius HEV simulation model, which also includes a power split logic adopted from Autonomie® software [63]. The power split logic sustains the battery charge by the end of the driving cycle so that $SOC(0)$=$SOC(k_f)$. Fig. 3.10-a shows that charge sustainability constraint is met over the UDDS for both controllers.

However, since the two-layer MPC consumes less battery energy for thermal management purpose, State of Charge (SOC) is higher on average for the two-layer MPC compared to the single-layer MPC. This means that the power split logic commands the ICE to run for a longer time to compensate the drop in SOC from the single-layer MPC, so that the battery charge is sustained by the end of the driving cycle. Consequently, the overall fuel consumption is higher from the single-layer MPC. As shown in Fig. 3.10-b, the two-layer MPC reduces the HEV equivalent fuel consumption by 2.2%, while reducing the engine ON percentage by 2.7% during the driving cycle. This improvement is attributed to the inclusion of future vehicle speed prediction into the optimization.

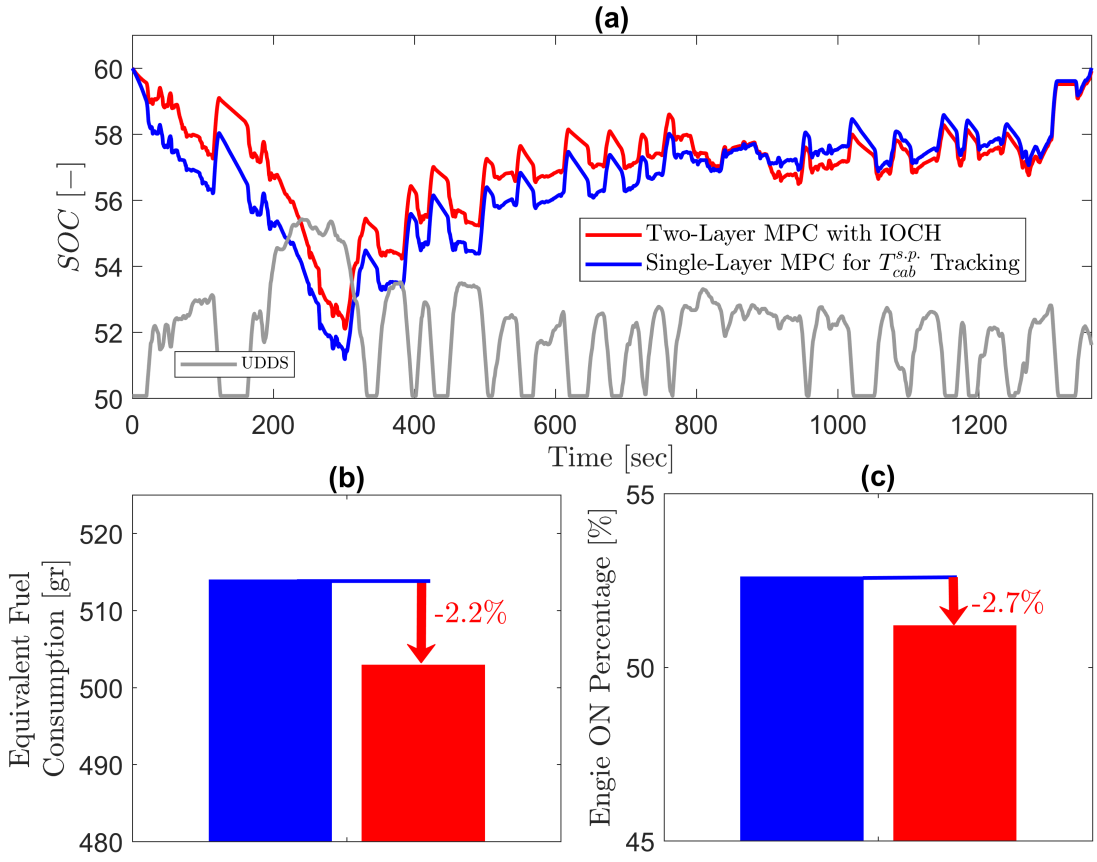

Figure 3.10: Results of implementing the single-layer and two-layer MPC with IOCH mechanisms on the high-fidelity Autonomie® HEV model for overall fuel consumption evaluation over UDDS assuming $SOC(0)$=60% (N_1=H_s= 6 (30 sec), and H_l=24 (120 sec)).

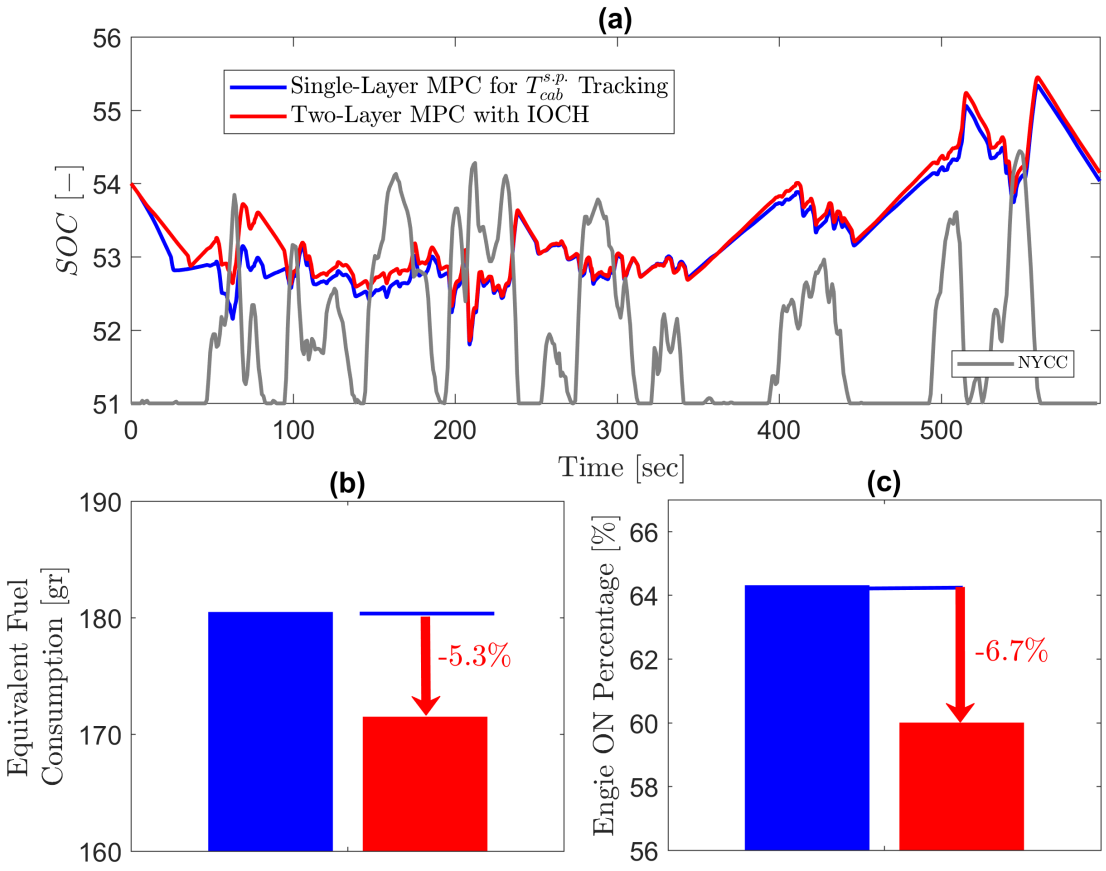

Figure 3.11: Results of implementing the single-layer and two-layer MPC with IOCH mechanism on the high-fidelity Autonomie® HEV model for overall fuel consumption evaluation over NYCC assuming $SOC(0)$=54% (N_1=H_s= 6 (30 sec), and H_l=24 (120 sec)).

For the congested city driving cycle (e.g., New York City Cycle (NYCC)), as shown in Fig. 3.11, the two-layer MPC with IOCH is able to reduce the HEV fuel consumption by 5.3%, compared to the single-layer MPC that tracks a constant cabin temperature setpoint. Compared to the single-layer MPC, the two-layer MPC decreases the fuel consumption by reducing the A/C cooling load on the battery at relatively long vehicle stops over the congested driving cycle, which results in less battery charge depletion. Consequently, the ICE needs to run for a shorter time by 6.7% (Fig. 3.11-c). By comparing UDDS and NYCC results from Figs. 3.10 and 3.11, it can be observed that due to nature of the NYCC, the energy saving resulted from two-layer MPC is larger for NYCC. This is because for the

NYCC, the cumulative vehicle stop time is longer than on UDDS. Thus, if the A/C cooling load is not optimized with respect to traffic conditions and the A/C compressor keeps working during the long stops, the battery charge will drop quickly. Moreover, compared to UDDS, the average traction power is lower by 70% for the congested traffic condition. Assuming the same weather and initial cabin temperature conditions, the A/C system power consumption is in the same range for both driving cycles. Therefore, the ratio of A/C cooling power to the NYCC traction power is much higher than the same ratio for UDDS, meaning that optimization of the A/C cooling load will have a more significant impact on the fuel consumption rate for the congested driving cycle, as shown in Fig. 3.11.

Finally, the same A/C energy management strategy is implemented over different driving cycles. Fig. 3.12 shows the vehicle-level fuel energy saving of the proposed strategy compared with the single-layer MPC baseline. As can be seen from Fig. 3.12, the energy saving benefit of the proposed A/C energy management strategy is more pronounced as the traffic congestion level increases, which confirms the conclusion made above when comparing the results between the UDDS and NYCC driving cycles.

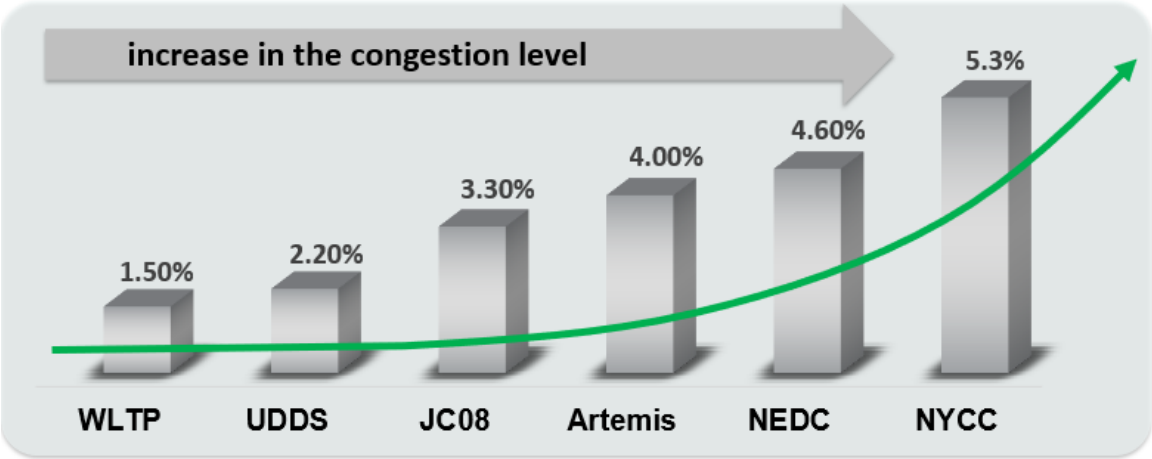

Figure 3.12: Vehicle level energy saving results over different driving cycles compared with the single-layer MPC baseline.

CHAPTER 4

Precision Cooling Strategy (PCS)

In Chapter 3, we proposed a hierarchical optimization framework for efficient A/C energy management, which leverages the vehicle speed sensitivity of A/C system efficiency for saving energy. In particular, the two-layer MPC structure considers the time-scale difference between the power and thermal systems and handles the uncertainties in vehicle speed prediction. Simulations results over different driving cycles have demonstrated the energy saving potentials. However, from the perspective of passenger comfort, only the constraints on the average cabin temperature (T_{cab}) was applied in the H-MPC problem formulation, which is not sufficient to represent practical occupant thermal comfort (OTC) requirements. To this end, the subsequent development in this dissertation will focus more on defining practical OTC metrics and incorporating them into overall A/C energy management problem.

4.1 Discharge Air Cooling Power and Comfort Implications

In this chapter, a precision cooling strategy (PCS) is proposed, attempting to address the trade-offs between the occupant thermal comfort and the A/C system energy consumption [53]. In order to quantify such trade-offs, a new performance metric, discharge air cooling power (DACP), is defined as follows:

$$P_{DACP}(t) = c_p(T_{cab}(t) - T_{discharge}(t))\dot{m}_{bl}(t), \tag{4.1}$$

where c_p is the specific heat capacity of air, T_{cab} represents the average cabin temperature, $T_{discharge}$ represents the discharge air temperature, namely, the temperature of the air after the heat exchange with the evaporator, and $\dot{m}_{bl}$ represents the air flow rate into the cabin delivered by HVAC blower. Note that the DACP in Eqn. (4.1) is defined for the case when A/C is running in the recirculation mode, which is also the simulation condition investigated in this chapter. If fresh air mode is considered, T_{cab} should be replaced by T_{amb} (ambient temperature). The integral of DACP over time is referred to as the Discharge Air Cooling Energy (DACE) and it is denoted by E_{DACE}, which will be used to quantify the overall cooling delivered to the cabin over a specified time window. Note that if the heats picked-up along the air delivery path is neglected, we may treat $T_{discharge}$ the same as T_{ain} (vent air temperature) as defined in previous chapter.

A key assumption behind this definition is that there exists a time-varying trajectory of $P_{DACP,targ}$ that, if it is precisely tracked, the occupant comfort requirement can be satisfied. In the definition, two major variables, temperature and flow rate of the cooling air, are considered to primarily impact the comfort. Compared with the average room temperature, which is commonly used as the performance metric in building HVAC control [56], [57] and also in our previous works [21], [38], [39], the choice of P_{DACP} accounts for special

characteristics of the automotive A/C system. In a passenger vehicle, occupants sit close to the vents and directly feel the temperature and the amount of air flow. The occupants' sensation to A/C is therefore not directly correlated to average cabin temperature but instead may be better captured by the new performance index proposed here. We note that realistic occupant comfort requirements are much more complicated than the $P_{DACP,targ}$ metric defined here and that a more comprehensive OTC model will be presented in Chapter 6. Besides the precise tracking of $P_{DACP,targ}$ which is intended to prevent over-cooling of the cabin, the idea similar to the development in Chapter 3 of exploiting the speed sensitivity of A/C system efficiency will also be pursued in the design of the PCS.

4.2 Control-oriented Model Development for ACSim

4.2.1 Predictive Model Structure

Like other high-fidelity A/C system models [54], ACSim model introduced in Chapter 2 involves detailed thermal and fluid dynamics of the refrigerant and has a large number of look-up tables from calibrations, which make it impossible to be used in a controller design. Therefore, a simplified model of the system dynamics is necessary. Specifically, the following discrete-time model structure is proposed to satisfy the requirements for MPC-based design:

$$\begin{aligned} T_{evap}(k+1) &= f_{T_{evap}} = T_{evap}(k) \\ &+ \gamma_1(T_{evap}(k) - T_{evap,targ}(k)) \\ &+ \gamma_2(T_{evap}(k) - T_{amb})\dot{m}_{bl}(k) \\ &+ \gamma_3(T_{evap}(k) - T_{amb})\Delta\dot{m}_{bl}(k) + \gamma_4, \qquad (4.2) \\ \dot{m}_{bl}(k+1) &= f_{\dot{m}_{bl}} = \dot{m}_{bl}(k) + \Delta\dot{m}_{bl}(k), \qquad (4.3) \\ T_{discharge}(k) &= f_{T_{discharge}} \\ &= \gamma_5 T_{evap}(k) + \gamma_6 T_{cab}(k) + \gamma_7. \qquad (4.4) \end{aligned}$$

In Eqns. (4.2)-(4.4), T_{cab}, T_{evap}, T_{amb}, $\dot{m}_{bl}$ and $T_{discharge}$ represent the cabin average air temperature, the evaporator wall temperature, the ambient temperature, the blower air flow rate, and the discharge air temperature, respectively. All temperatures are in ^oC and the blower air flow rate has the units of kg/s. The model states are T_{evap} and $\dot{m}_{bl}$. The model inputs are the incremental blower air flow rate, $\Delta\dot{m}_{bl}$, and the evaporator wall temperature target, $T_{evap,targ}$. The model parameters, γ_i $(i = 1, 2, ..., 7)$, are constants and to be identified for matching the system responses. This predictive model is nonlinear because of the multiplicative coupling between model states and inputs in Eqn. (4.2).

Compared with the evaporator wall temperature model proposed in [21] and presented in Chapter 3, which is modeled as a first-order system with $T_{evap,targ}$ as an input, air flow effects ($\dot{m}_{bl}$ and $\Delta\dot{m}_{bl}$) are considered in this work based on the observation that with fixed $T_{evap,targ}$, T_{evap} changes when air flow changes.

4.2.2 Model Identification and Validation

Next, the ACSim model is simulated with different random sinusoidal input signals. The system responses are collected with the sampling time, $T_s = 3sec$, to identify the unknown parameters in Eqn. (4.2) and Eqn. (4.4). The resulting identified parameters are $\gamma = [\gamma_1\ \gamma_2\ ...\ \gamma_7] = [-0.084, -0.487, -1.121, -1.730, 0.729, 0.690, -11.457]$.

Fig. 4.1 provides the validation results of the simplified predictive model for matching the outputs from ACSim model. It confirms the good accuracy of the proposed model in modeling the key dynamics of the A/C system.

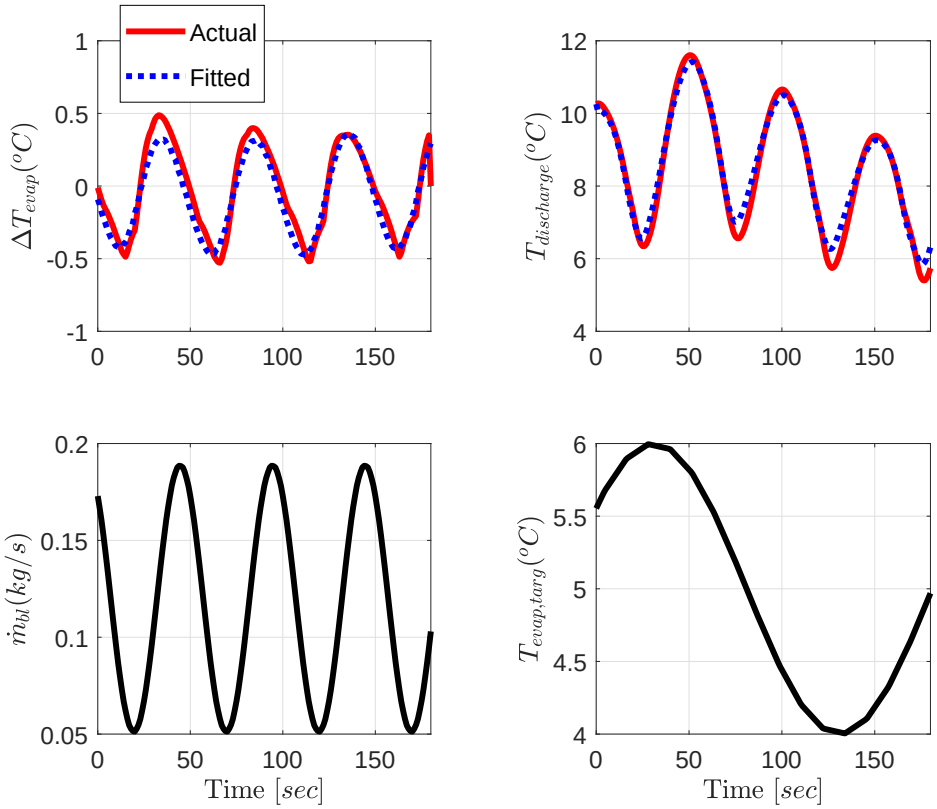

Figure 4.1: Model validation results of $\Delta T_{evap}(k) = T_{evap}(k+1) - T_{evap}(k)$ and $T_{discharge}(k)$ for given sinusoidal excitations.

4.3 Problem Formulation of the PCS

In this section, the problem formulation of the proposed PCS is described, whose objective is combining the minimization of overall A/C energy consumption and the tracking error with respect to the target $P_{DACP,targ}$ trajectory. As may be observed in Fig. (**??**), the compressor power is dominant as compared with the EDF power. Therefore, we decide to use the predicted compressor power in the cost function to reflect the overall system energy consumption in the proposed nonlinear MPC (NMPC) problem. According to [56], P_{comp} can be estimated by:

$$P_{comp}(k) = \frac{c_p}{COP(k)}(T_{cab}(k) - T_{discharge}(k))\dot{m}_{bl}(k), \tag{4.5}$$

where $c_p = 1008\ J/(kg \cdot K)$ is the specific heat capacity of air at constant pressure, COP represents the A/C system coefficient of performance [58]. Note that, COP may be time-varying, however, in the MPC problem formulation, it is assumed to be constant over the prediction horizon and will be updated based on current measurements at the beginning of each control iteration. Fig. 4.2 shows the comparison between the compressor power estimated using Eqn. (4.5) and the actual compressor power computed by ACSim, which is based on the thermo-dynamics of the vapor-compression refrigeration system.

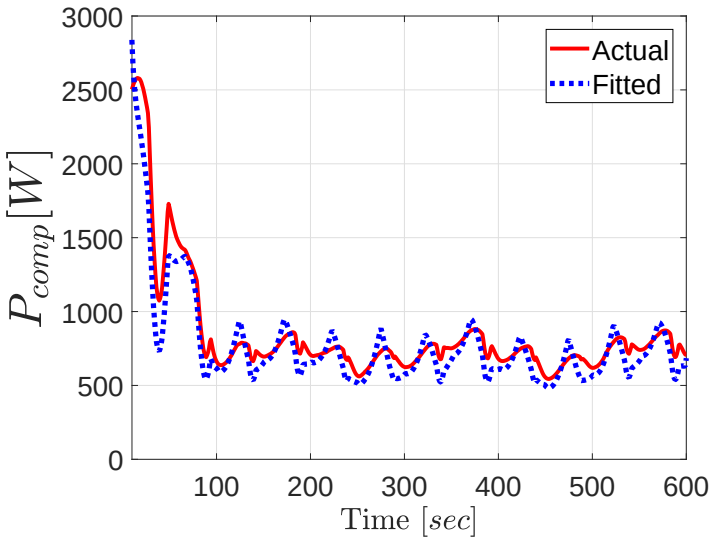

Figure 4.2: Estimated compressor power based on Eqn. (4.5) compared with actual compressor power measured from ACSim.

Then, we define the PCS strategy as the following nonlinear optimization problem:

$$
\begin{aligned}
\min_{\substack{\Delta\dot{m}_{bl} \\ T_{evap,targ}}} \quad & \sum_{i=0}^{N_p} \left\{ \begin{array}{l} P_{comp}(i|k) + \alpha \cdot (P_{DACP}(i|k) \\ \\ -\beta(i|k) \cdot P_{DACP,targ}(i|k))^2 \end{array} \right\}, \\
\text{s.t.} \quad & T_{evap}(i+1|k) = f_{T_{evap}}(i|k), \\
& \dot{m}_{bl}(i+1|k) = f_{\dot{m}_{bl}}(i|k), \\
& 0\ ^oC \leq T_{evap}(i|k) \leq T_{evap}^{UB}(i|k), \\
& 0.05\ kg/s \leq \dot{m}_{bl}(i|k) \leq 0.15\ kg/s, \\
& -0.05\ kg/s \leq \Delta\dot{m}_{bl}(i|k) \leq 0.05\ kg/s, \\
& 2\ ^oC \leq T_{evap,targ}(i|k) \leq 10\ ^oC, \\
& T_{evap}(0|k) = T_{evap}(k),\ \dot{m}_{bl}(0|k) = \dot{m}_{bl}(k).
\end{aligned}
\tag{4.6}
$$

In (4.6), $(i|k)$ denotes the prediction for the time instant $k+i$ made at the time instant k, $f_{T_{evap}}$ and $f_{\dot{m}_{bl}}$ are from Eqn. (4.2) and Eqn. (4.3). In the cost function, α and β are design parameters. In this study, α is set to be a large positive constant, e.g., 10^5, to ensure the tracking performance. While β can be either constant, 1, or time-varying with respect to vehicle speed preview, depending on the operating scenarios of the A/C system. Detailed design of β and its impact will be discussed in the next section. $P_{DACP,targ}$ and T_{evap}^{UB} represent the target DACP trajectory and the time-varying upper bound for T_{evap}, respectively, which are assumed to be known over the prediction horizon. Constant constraints for other variables are given according to the system operating requirements. For the results presented in the next section, the prediction horizon, N_p, is set to be 10. The NMPC problem described by (4.6) is solved numerically using the MPCTools package [64]. This package exploits CasADi [65] for automatic differentiation and IPOPT algorithm for the numerical optimization.

4.4 Simulation Results and Performance Evaluation of the PCS

4.4.1 Simulation Results on the Simplified Model

The performance of the proposed MPC-based PCS is first evaluated on the simplified system model developed in Section 4.3. In Fig. 4.3, an example of simulating a typical summer cabin cool-down scenario is shown. In order to ensure precise tracking of $P_{DACP,targ}$, constant $\beta = 1$ is set. Vehicle speed trajectory from Supplemental Federal Test Procedure-1 (SC03) cycle is applied. It can been from Fig. 4.3 that all the state and input constraints in red dotted lines are satisfied, and perfect tracking of $P_{DACP,targ}$ is achieved except for the initial transient period. In this simulation, T_{cab} and COP are assumed to be constant values.

4.4.2 Simulation Results on the ACSim Model

Next, the proposed control strategy is integrated in closed-loop with the ACSim model. Fig. 4.4 illustrates the implementation in Simulink®. The model predictive controller takes sensor measurements, predefined $P_{DACP,targ}$ trajectories, and future vehicle speed from the traffic prediction as inputs, solves the optimization problem defined by (4.6), and provides the control inputs to the ACSim model.

In this case study, the proposed MPC controller updates the control inputs every $3\ sec$, while the outputs from ACSim model is originally sampled at $0.1\ sec$. The same cabin cool-down process is considered and $P_{DACP,targ}$ trajectory is calculated from a Ford benchmark case over SC03 cycle. In addition, a heuristic design of β with respect to the speed profile from SC03 cycle is applied. The dependence of β on different vehicle speed can be seen from Fig. 4.5. The idea behind such heuristic design of β coincides with the exploration of the speed sensitivity of A/C operation, which is that energy efficiency may be improved by shifting the A/C load from low efficiency region (at low vehicle speed) to high efficiency

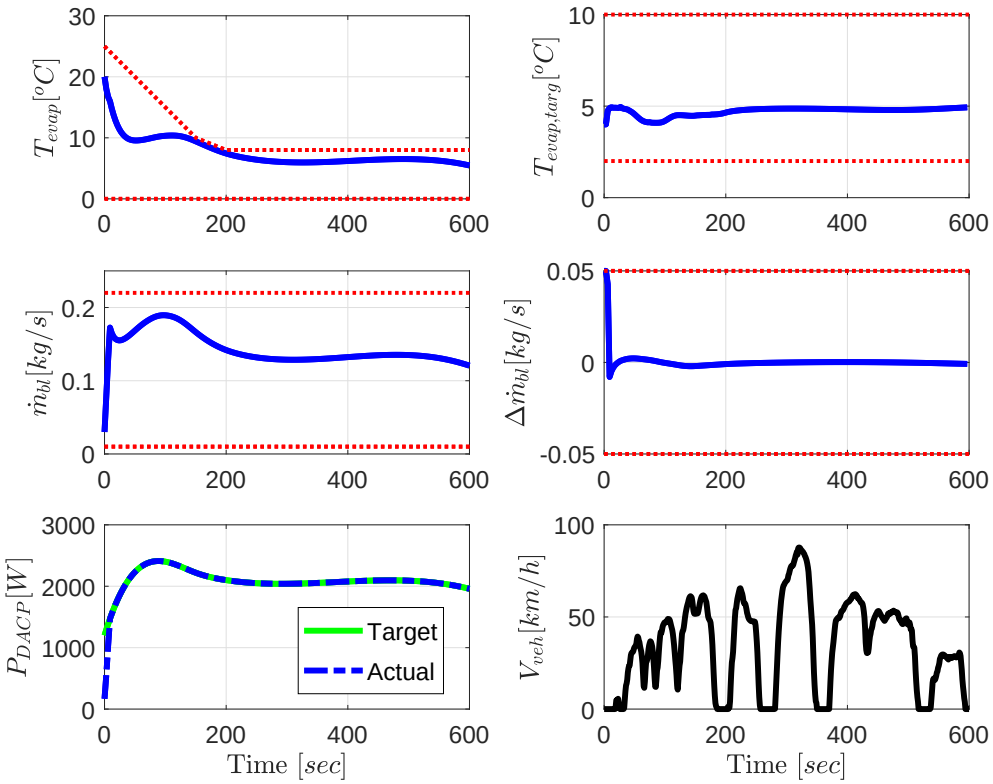

Figure 4.3: Performance evaluation of the proposed PCS on the simplified A/C system model.

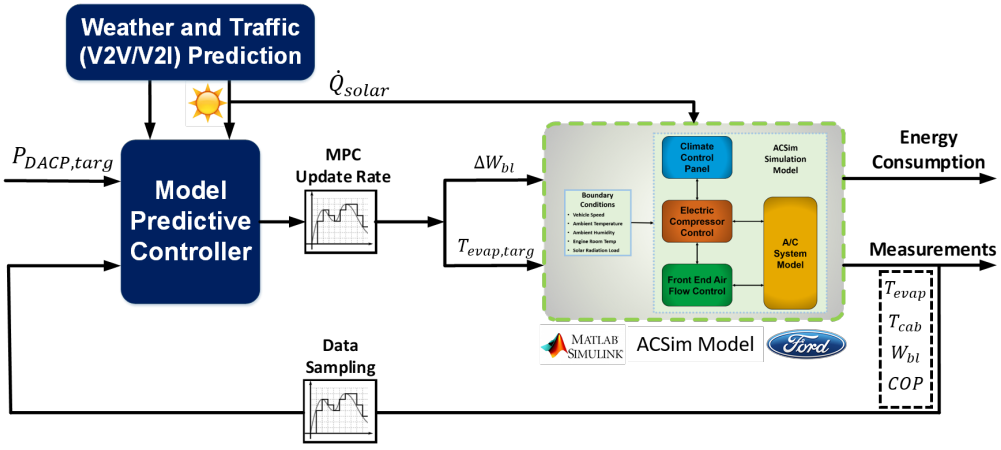

Figure 4.4: Schematics of integrating the MPC-based PCS with ACSim model in Simulink®.

region (at high vehicle speed). In the simulation with time-varying β, the vehicle speed over the prediction horizon is assumed to be known via connectivity technology, thus the values of β over the prediction horizon are also available.

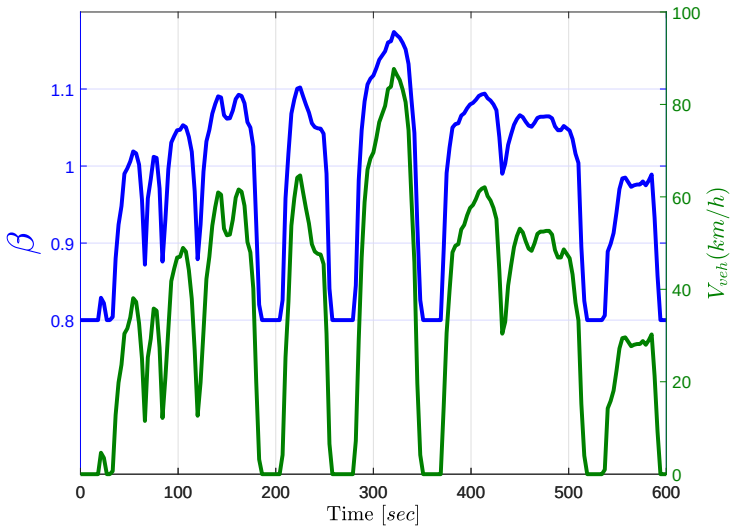

Figure 4.5: Heuristic design of speed-dependent β.

Fig. 4.6 compares the benchmark case with the NMPC results with constant β and speed-dependent β, respectively. As observed from the results, for the constant β case, the NMPC regulates the control inputs to achieve precise tracking of the $P_{DACP,targ}$ trajectories. For the speed-dependent β, the actual P_{DACP} varies around the target. In addition, clear coordination between the control inputs and vehicle speed can be seen in the speed-dependent β case indicating successful load shift as intended. In this simulation, T_{cab} and COP are assumed to have constant values along prediction horizon for each control iteration and are updated using measurements at every sampling instant. Additional system responses including the trajectories of P_{comp}, P_{EDF}, T_{cab} and $T_{discharge}$ are shown in Fig. 4.7. Detailed energy consumptions of different cases are reported in Table 4.1. It can be seen that, compared with the benchmark case, the total A/C energy consumption is reduced by 4.9% for the MPC results with constant β. This is because for matching the $P_{DACP,targ}$, the MPC-based controller tends to reduce the air flow ($\dot{m}_{bl}$) towards the end of

the cycle, which results in the same pull-down period of the cabin temperature (T_{cab}) but slight increase in final cabin temperature (with difference less than 1^oC). In other words, the actual cooling capacity of the A/C system is reduced for the MPC case while achieving the same occupant thermal comfort level according to the proposed metric. If we compare the MPC results with speed-dependent β with the ones with constant β, we can see that the energy consumption of the A/C system may be further reduced by 0.8% while providing 1.1% higher E_{DACE}. The energy saving achieved by A/C load shifting can be even higher if designing β optimally instead of designing it in a heuristic way.

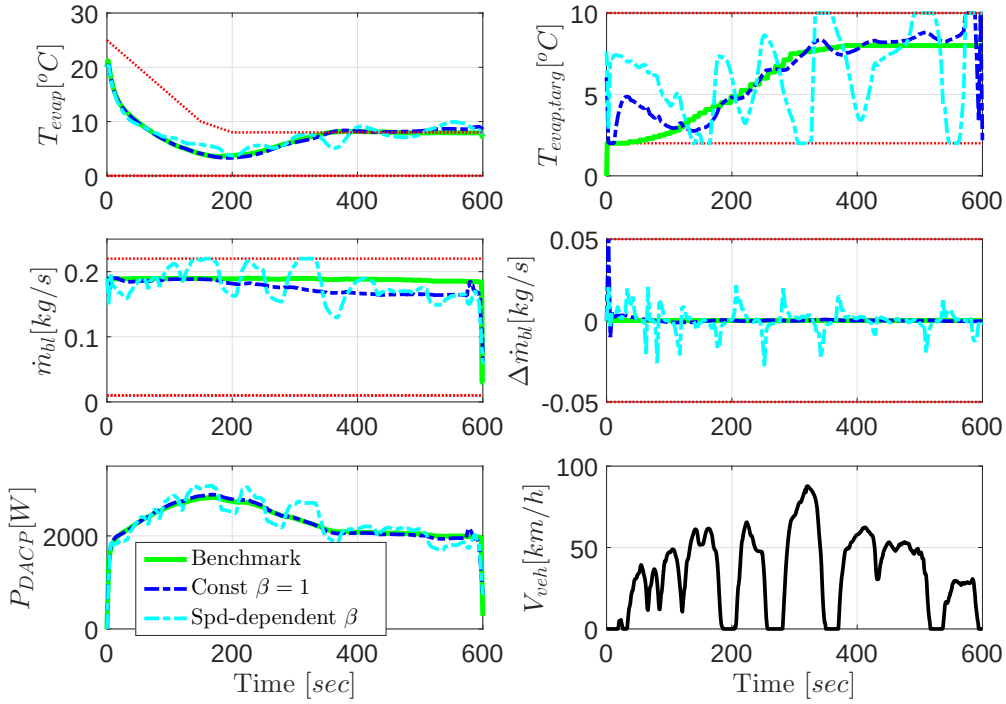

Figure 4.6: Comparison between the proposed PCS and the benchmark case on the ACSim model (key control variables).

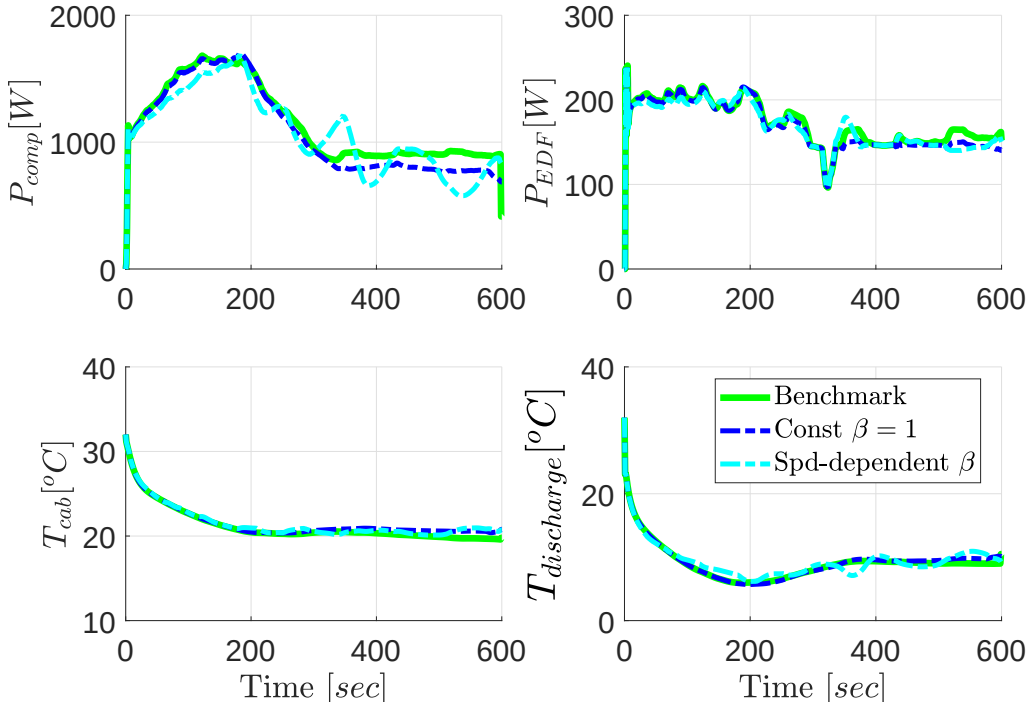

Figure 4.7: Comparison between the proposed PCS and the benchmark case on the ACSim model (A/C energy consumptions and temperatures) .

Table 4.1: A/C system energy consumption comparisons of applying constant $\beta = 1$ and speed dependent β with respect to the benchmark.

	E_{DACE} [kJ]	E_{comp} [kJ]	E_{EDF} [kJ]	E_{tot} [kJ]
Benchmark	1378.4	689.4	103.2	792.6
Constant $\beta = 1$	1377.7 (-0.1%)	653.4	100.6	754.0 (-4.9%)
Spd-dependent β	1392.0 (+1.0%)	647.2	100.6	747.8 (-5.7%)

Fig. 4.8 reports the elapsed CPU time for each control iteration compared with 3 sec for the MPC sampling time. This result is obtained based on a 2.9 GHz Windows computer for the speed-dependent β case considered in this section. Note that the worst case execution time is significantly lower than the available time. These results suggest that our NMPC approach could be computationally feasible even in slower ECU as the ECU implementation will be based on highly optimized C-code (rather than Matlab) that, based

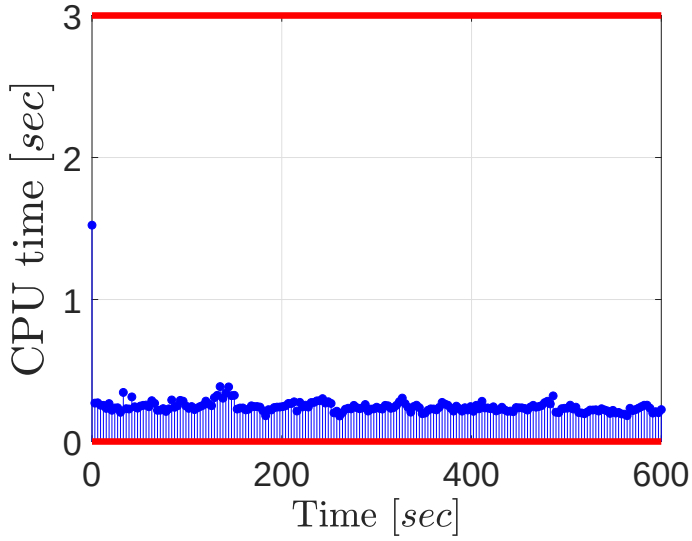

Figure 4.8: Elapsed CPU time for computing MPC solution for each control instant on ACSim model.

on our past experience, is likely to offset the processor differences.

CHAPTER 5

Experimental Validation of an Eco-cooling Strategy on a Hybrid Electric Vehicle

In this chapter, the design and vehicle tests of an eco-cooling strategy will be presented. The eco-cooling strategy leverages the sensitivity of A/C system efficiency to vehicle speed demonstrated in previous chapters. The design of eco-cooling strategy inherits the idea from the precision cooling strategy (PCS) presented in Chapter 4, but is adapted to the specific vehicle testing requirements. The energy savings on both A/C system level and vehicle level will be demonstrated based on the average value of multiple repeatable tests. Besides the energy saving from the eco-cooling tests, A/C recirculation impact will also be discussed based on additional testing results.

5.1 Vehicle Instrumentation and Baseline Tests on HVAC System

5.1.1 Vehicle Instrumentation

Our testing vehicle is a 2017 Toyota Prius Four Turing HEV, which was procured in June 2017. It has been instrumented by Roush in order to enable the implementation of the HVAC controls and demonstrate the vehicle energy saving. The schematic of the modified HVAC system is shown in Fig. 5.1.

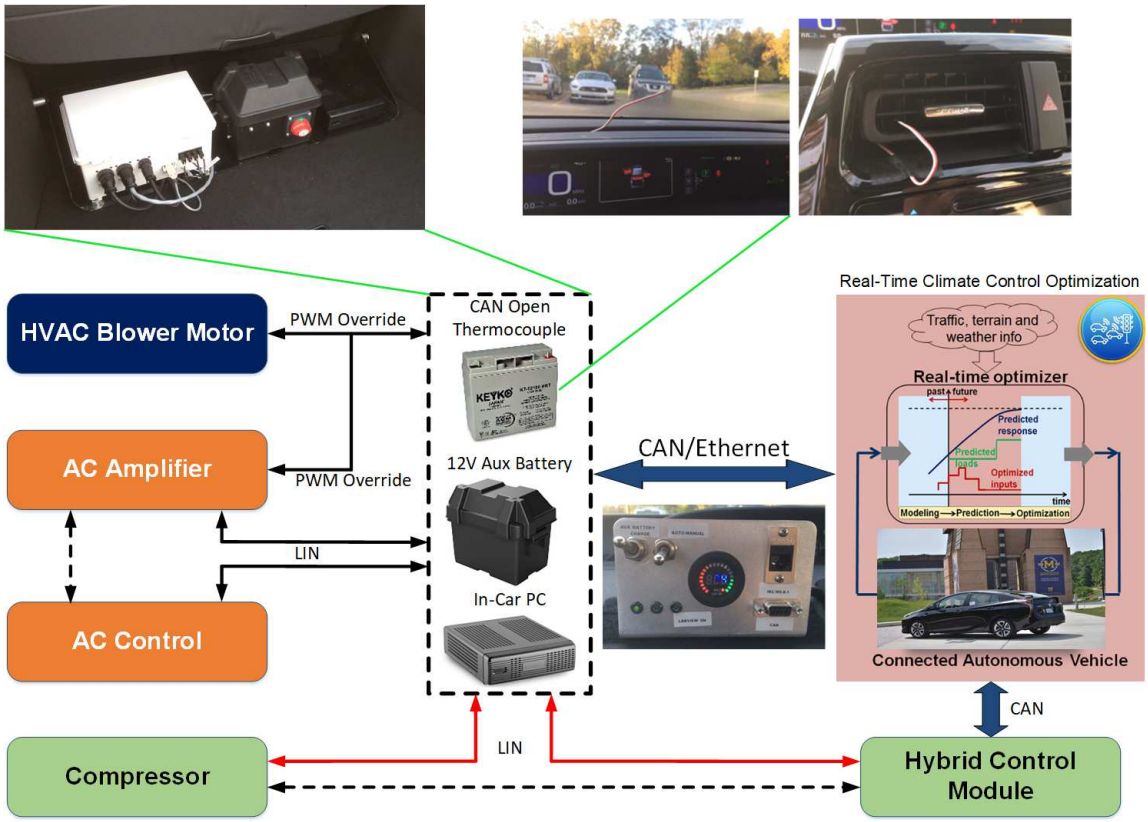

Figure 5.1: Schematic of the Modified Toyota Prius HVAC Control System with added thermocouples, CAN open thermocouple module, auxiliary battery, and In-Car PC.

As can be seen from Fig. 5.1, the original control loops are modified to access the available signals (see the full list in Appendix A) on the Controller Area Network (CAN) and Local Interconnect Network (LIN) buses through the In-Car PC via a NeoVI Fire mod-

ules. The In-Car PC is communicating with the testing laptop via Ethernet, where the CAN/LIN messages are read and logged through a LabVIEW interface. The LabVIEW interface allows for real-time data collection from the vehicle, and intercepting the A/C control commands by the user. All accessible vehicle measurements are listed in Appendix A. The commands, which can be sent to the vehicle in real-time, include the A/C blower speed, cabin temperature setpoint, blend door position setpoint, AC On/Off command, rear HVAC On/Off command, recirculation On/Off command, ECO mode On/Off command, rear/front defrost On/Off command, and auto mode On/Off command. In order to evaluate the thermal behavior inside the cabin, additional thermocouples have been installed within

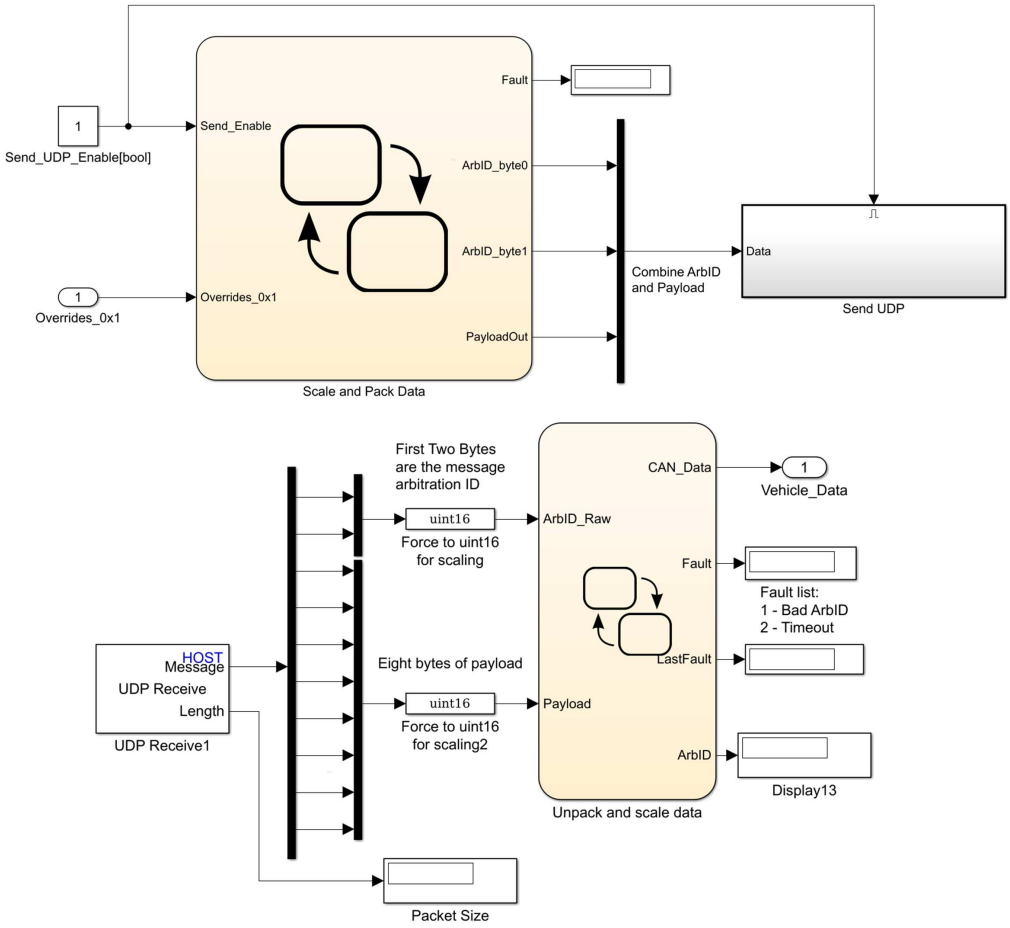

Figure 5.2: Schematic of the developed Simulink model to parse UDP data to be used in real-time by the HVAC controller.

the cabin, and added to the CAN bus. These thermocouples are shown on the top right in Fig. 5.1, including the temperature measured above the dashboard and the vent air temperature. Moreover, comprehensive airflow measurement tests have been performed by Roush to generate the A/C blower air flow map (see Appendix B), which will be used to develop the eco-cooling strategy.

To facilitate the design of the eco-cooling strategy and the vehicle tests in MATLAB/Simulink environment, a Simulink model (shown in Fig. 5.2) was developed to parse the messages, which will be used as feedback signals for the HVAC controller in real-time. Moreover, the developed Simulink model sends the computed HVAC control signals to the vehicle network by converting the control signals to UDP data. Overall, the instrumented vehicle allows us to log the vehicle data and update control commands by a Simulnik-based controller interface.

5.1.2 Vehicle Testing Results to Characterize HVAC System Impacts

To quantify the impacts of HVAC system on fuel economy, vehicle heating tests were performed during December 2017 and January 2018 and cooling tests were performed from May 2018 to July 2018. The testing results are reported separately in what follows.

5.1.2.1 Vehicle Tests to Characterize Heating System Impact

Unlike the cooling system, the heating system of our test vehicle utilizes the engine coolant heat. The heating power is delivered to cabin by the HVAC blower. Whenever free energy from engine waste heat is used for heating, there is no incremental energy consumption penalty. However, in cold weather, when engine waste heat is not sufficient, the fuel consumption may increase [29] during city driving and extended engine idling operation.

In the cold weather, extensive vehicle tests were performed to to understand the impacts of vehicle heating system on fuel consumption. It was found that in a city driving test with light traffic and ambient temperature around -8^oC, vehicle fuel consumption increases

by 21% due to the operation of the heating system, while negligible energy consumption increase is observed for highway tests with the same HVAC operation. During the city driving tests, auxiliary components of the heating system (e.g. engine coolant pump and HVAC blower) consume little energy and so most of the fuel consumption increase is attributed to engine efficiency drop and extended engine idling time. The energy saving opportunities exist in coordinating the control of HVAC system with engine operation to maintain the high operation efficiency of the engine and minimize the engine idling time.

Details of the testing results are reported as follows. A local driving test was performed at two different days when the ambient temperatures were around -8^oC. The data of three trips along the same route with HVAC on (75^oF temperature setpoint and constant blower flow rate) were collected on the same day, while, the data for HVAC off case were collected on the other day. The same testing scenario were implemented for highway driving as well. The testing routes and vehicle speed profiles of all trips are shown in Fig. 5.3 and Fig. 5.4 for local and highway driving, respectively. The energy consumption values are compared in Table 5.1 and Fig. 5.5. Note that the vehicle-level energy consumptions is computed using the following equation which will be used throughout this chapter for all vehicle tests:

$$E_{veh} = \int_0^T \frac{\dot{m}_{air}(t)}{AFR(t)} \cdot LHV \; dt + \frac{E_{batt} \cdot \Delta SOC}{\eta_{sys}}, \tag{5.1}$$

$$AFR(t) = \lambda(t) \cdot AFR_{stoich}, \tag{5.2}$$

$$\Delta SOC = SOC(0) - SOC(T), \tag{5.3}$$

where T represents the duration of each test run, $\dot{m}_{air}$ represents the air flow rate into the engine measured by the Mass Air Flow (MAF) sensor, AFR, λ, and AFR_{stoich} represent the air-fuel ratio, equivalent air-fuel ratio (measured), and stoichiometric air-fuel ratio, respectively, LHV represents the Lower Heating Value (LHV) of the gasoline, E_{batt} repre-

sents the battery capacity, η_{sys} represents the energy conversion efficiency from fuel energy to battery energy, and SOC represents the estimated battery state of charge from the measured CAN data. In general, this vehicle-level energy consumption (E_{veh}) computation is based on adjusted fuel energy which accounts for the SOC deviation over the entire test trip.

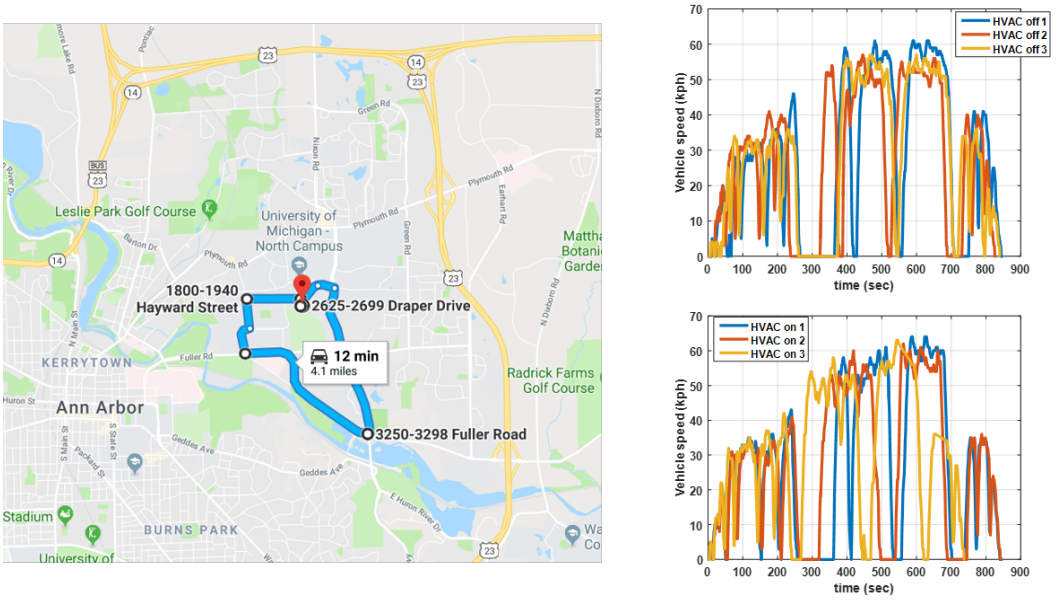

Figure 5.3: Local driving tests: Route (left) and vehicle speed profiles (right).

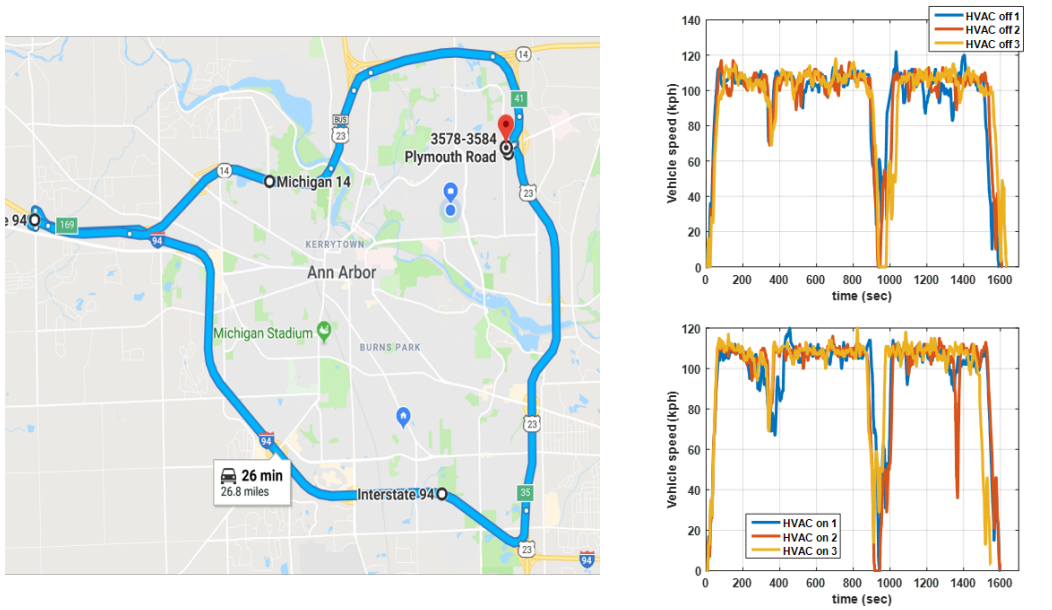

Figure 5.4: Highway driving tests: Route (left) and vehicle speed profiles (right).

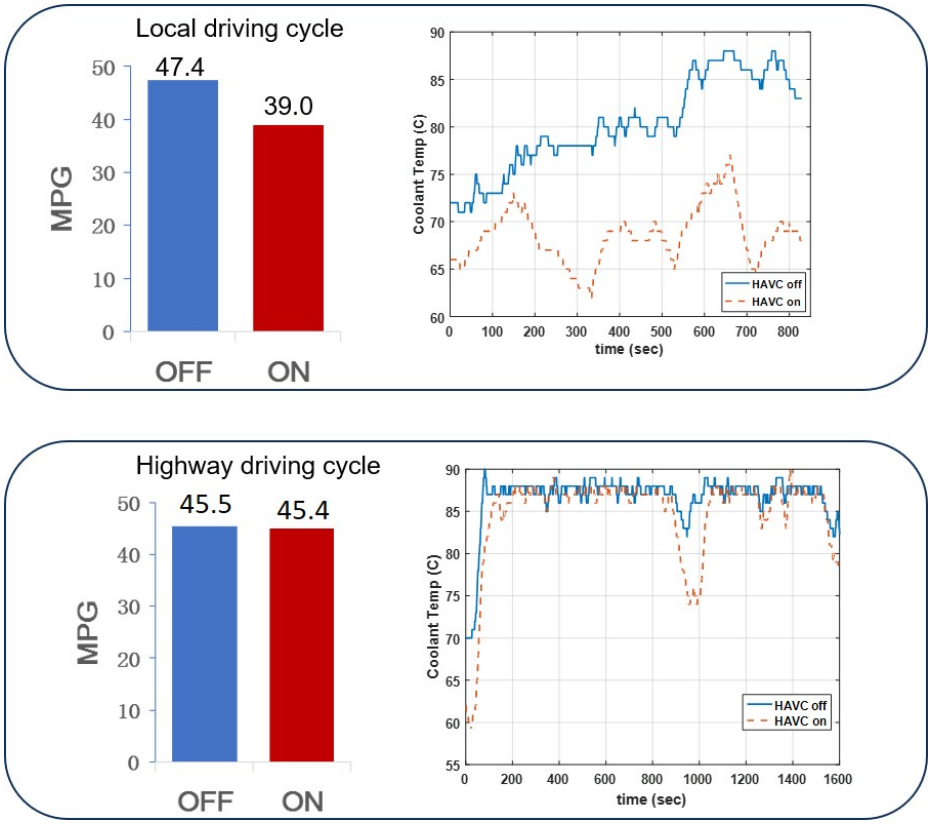

Figure 5.5: Summary of the results for vehicle heating tests.

Table 5.1: Vehicle-level energy consumption comparison

		Test1 (MJ)	Test 2 (MJ)	Test 3 (MJ)	Average (MJ)	Increase (%)	MPG
Local test	HVAC off	12.15	9.64	8.41	10.07	0	47.4
	HVAC on	12.66	12.61	11.40	12.22	21.35	39.0
Highway test	HVAC off	72.08	66.58	66.76	68.47	0	45.5
	HVAC on	69.81	68.20	68.61	68.87	0.58	45.4

Key findings of the heating tests are summarized in Fig. 5.5. The differences in fuel consumption between highway and local driving are correlated with the coolant temperature differences.

5.1.2.2 Vehicle Tests to Characterize Cooling System Impact

Two sets of vehicle tests to characterize the impact of A/C operation on vehicle-level energy consumption have been performed:

- The first set of tests was performed in May 2018 on a local driving route in Ann Arbor. While the driving route, travel time, and average vehicle speed were controlled

to be similar, due to external disturbances, changing traffic dynamics, and variable traffic light timings, the overall vehicle traction energy consumption may vary between tests. However, the energy consumed by the A/C system is consistent among different cases.

- In order to achieve more consistent vehicle speed profiles among different tests, another set of repeatable tests was performed in July 2018 to mimic the congested driving conditions with accurate control of stop-and-go timing in a disturbance-free driving environment.

Detailed testing conditions and results are reported as follows.

Tests performed on a local route: This set of tests was performed along a route shown in Fig. 5.6. It is a 4.1-mile trip in Ann Arbor and the tests were done with no traffic. Fig. 5.7 shows the speed trajectories during the six tests, three of which had A/C system off and three of which had A/C system on. The A/C on tests and A/C off tests were performed on two different sunny days with the same ambient temperature. The test conditions are summarized in Table 4.2.

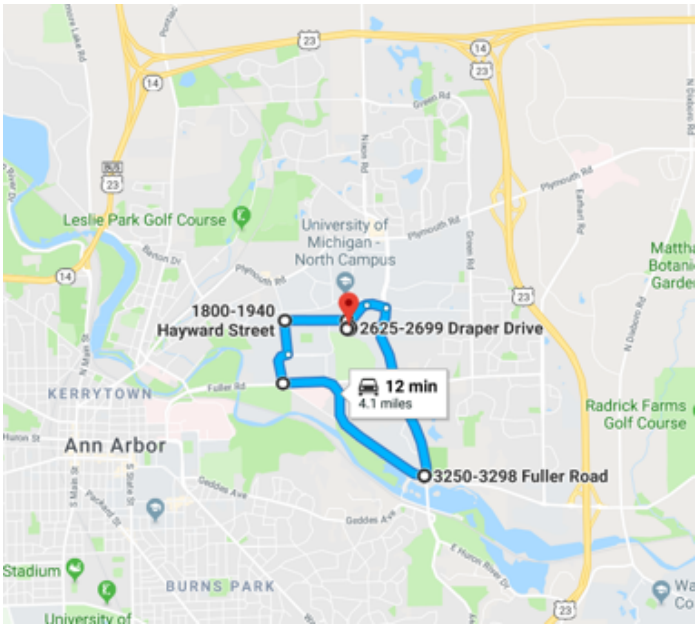

Figure 5.6: Local testing route information.

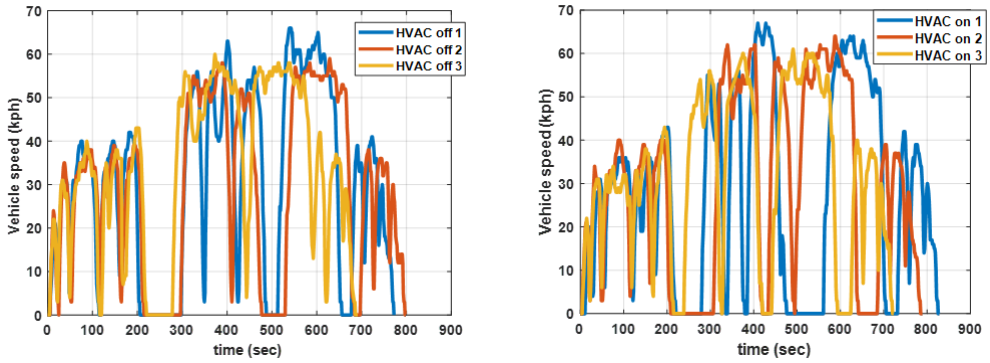

Figure 5.7: Local tests speed profiles.

Table 5.2: Test conditions for local driving tests.

Ambient temperature	A/C temp set-point	A/C blower	Recirculation
$81F^o$	$65F^o$	Maximum	No

Table 5.3: Vehicle-level energy consumption comparison (local driving tests).

	Test 1	Test 2	Test 3	Average	Increase	MPG
HVAC off	$5.84\ MJ$	$5.65\ MJ$	$5.19\ MJ$	$5.56\ MJ$	0	85.9
HVAC on	$10.14\ MJ$	$8.19\ MJ$	$8.17\ MJ$	$8.83\ MJ$	58.8%	54.2

The vehicle-level energy consumption for each test was computed based on the testing data. Table 4.3 provides energy consumption comparison between A/C off and on cases. As inferred from the test results, the A/C operation can cause a significant increase in the vehicle level energy consumption. Our energy consumption comparison results are reasonable under the assumption that the energy used for driving the vehicle are the same among all testing trips. This assumption is reasonable under the following conditions:

1. Each test trip starts and ends at the same location.

2. Overall trends in speed trajectories are similar (See Fig. 5.8 for the speed profile comparison without stops due to red traffic signals). The detailed differences occur mainly due to time shift related to the uncertainties in the traffic signals and traffic flow conditions.

Detailed A/C compressor and evaporator behaviors can be seen in Fig. 5.9.

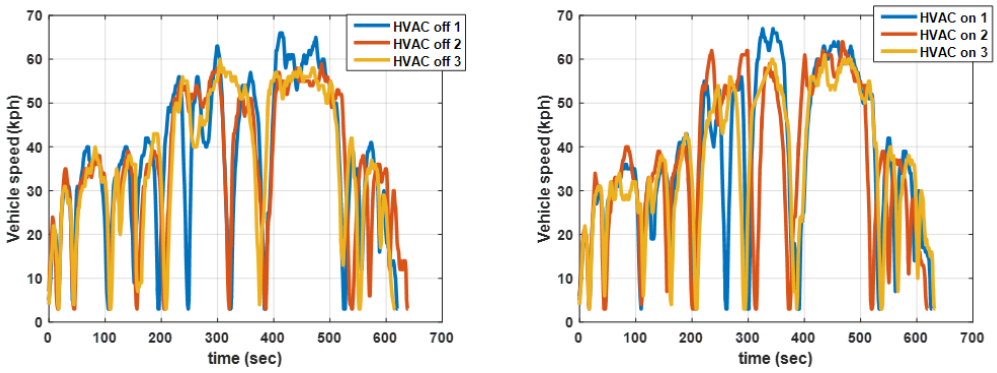

Figure 5.8: Local tests speed profiles with removed stops.

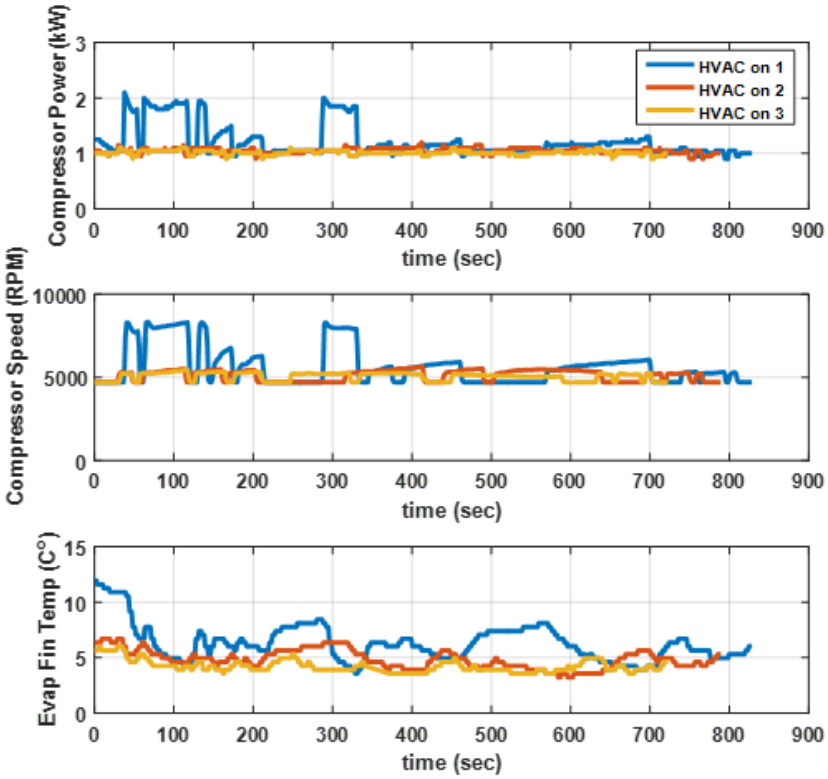

Figure 5.9: A/C system responses during local tests.

Tests performed in "simulated and controlled" congested driving conditions: Although we showed in Fig. 5.8 that the speed profiles are getting closer as we remove the stops due to uncertain traffic signals, the differences in speed profiles may still cause differences in fuel energy consumed for driving the vehicle. Therefore, the second set of tests

with repeatable and accurate controlled vehicle speed was performed in a disturbance-free environment aiming at mimicking the congested city driving scenario.

These tests were performed with testing conditions shown in Table 5.4. For this set of tests, the vehicle speed trajectories are repeatable, see Fig. 5.10. Adjusted energy consumption for each case and the A/C system responses are reported in Table 5.5 and Fig. 5.11, respectively. Compared with the local driving test, the impact of A/C system operation on vehicle fuel consumption is even more significant for congested driving scenario. This can be explained by the fact that the average vehicle speed for emulated congested city driving case (17.9 km/s) is lower than the one for the local driving case (29.7 km/h). Therefore given the same time period, the energy consumed for driving the vehicle is less for the former case. At the same time, energy consumed by A/C system is approximately the same.

Table 5.4: Test conditions for parking lot tests.

Ambient temperature	A/C temp set-point	A/C blower	Recirculation
$90F^o$	$65F^o$	Maximum	No

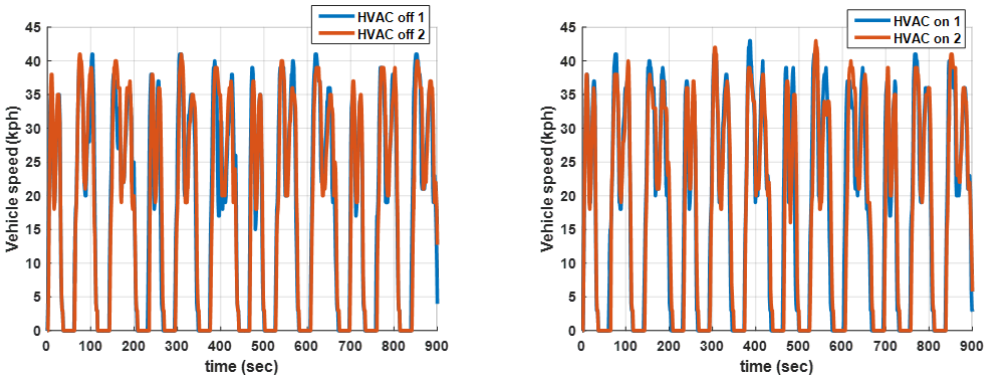

Figure 5.10: Parking lot tests with repeatable vehicle speed profiles.

Table 5.5: Adjusted fuel energy consumption comparison (parking lot tests).

	Test 1	Test 2	Average	Increase	MPG
HVAC off	4.28 MJ	4.55 MJ	4.42 MJ	0	72.9
HVAC on	9.09 MJ	8.06 MJ	8.58 MJ	94.0%	37.6

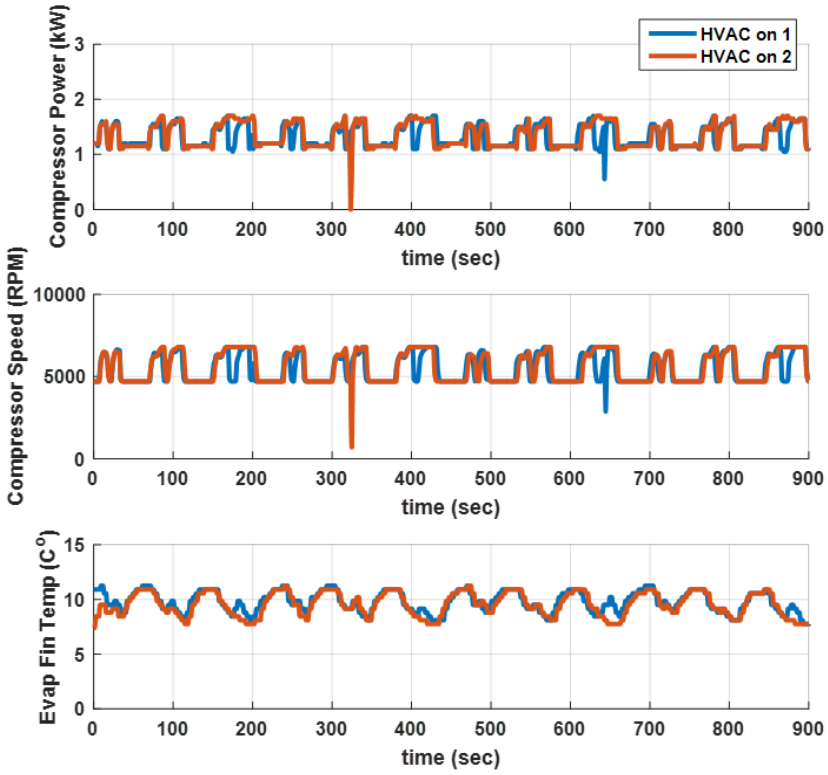

Figure 5.11: A/C system behaviors during parking lot tests.

5.2 Eco-cooling Strategy

In this section, the control-oriented model of the A/C system in the test vehicle will be presented followed by the detailed problem formulation of the proposed eco-cooling strategy.

5.2.1 Control-oriented Model Development of the A/C System

The control-oriented model for the A/C system of the test vehicle is similar to the one used for the development of the precision cooling strategy (PCS) presented in Chapter 4.

However, modifications were made to account for the differences between the physical setup of the test vehicle and the ACSim simulation model. Specifically, in the test vehicle, the vapor-compression process (i.e. the compressor and the evaporator) is not directly controlled to avoid damaging A/C system components. In particular, the nominal controller adjusts the evaporator wall temperature ($T_{evap,targ}$ from Eqn. 4.2) is not accessible in the vehicle tests while our controller manipulates the cabin cooling demand by adjusting the blower flow rate ($\dot{m}_{bl}$) and cabin temperature setpoint (T_{sp}). The control-oriented model then has the following form,

$$\begin{aligned} T_{evap}(k+1) &= f_{T_{evap}} \\ &= \gamma_1 T_{evap}(k) + \gamma_2 (T_{evap}(k) - T_{amb}) \dot{m}_{bl}(k) + \gamma_3, \qquad (5.4) \\ T_{ain}(k) &= f_{T_{ain}} \\ &= \gamma_4 T_{evap}(k) + \gamma_5 T_{sp}(k), \qquad (5.5) \end{aligned}$$

where T_{evap}, T_{amb}, $\dot{m}_{bl}$ and T_{ain} represent the evaporator wall temperature, the ambient temperature, the blower air flow rate, and the vent air temperature, respectively. All temperatures are in ^oC and the blower air flow rate has the units of kg/s. The model state is T_{evap}. The model inputs are the blower air flow rate, $\dot{m}_{bl}$, and the cabin temperature setpoint (T_{sp}). The model parameters, γ_i $(i = 1, 2, ..., 5)$, are constants identified from the vehicle data. This model is nonlinear because of the multiplicative coupling between model state and input in Eqn. (5.4). The model validation results are shown in Fig. 5.12 for the sinusoidal input excitation is applied while the vehicle is traveling on a local route. The sampling period is $5\ sec$ and γ_i $(i = 1, 2, ..., 5) = [1.0719, -1.2265, -2.8523, 0.8964, 0.1252]$, which was identified using a different data set. As can be seen from Fig. 5.12, the model can capture the evaporator wall temperature dynamics and match the vent air temperature well. This experimentally-validated control-oriented model will be used by our eco-cooling strategy.

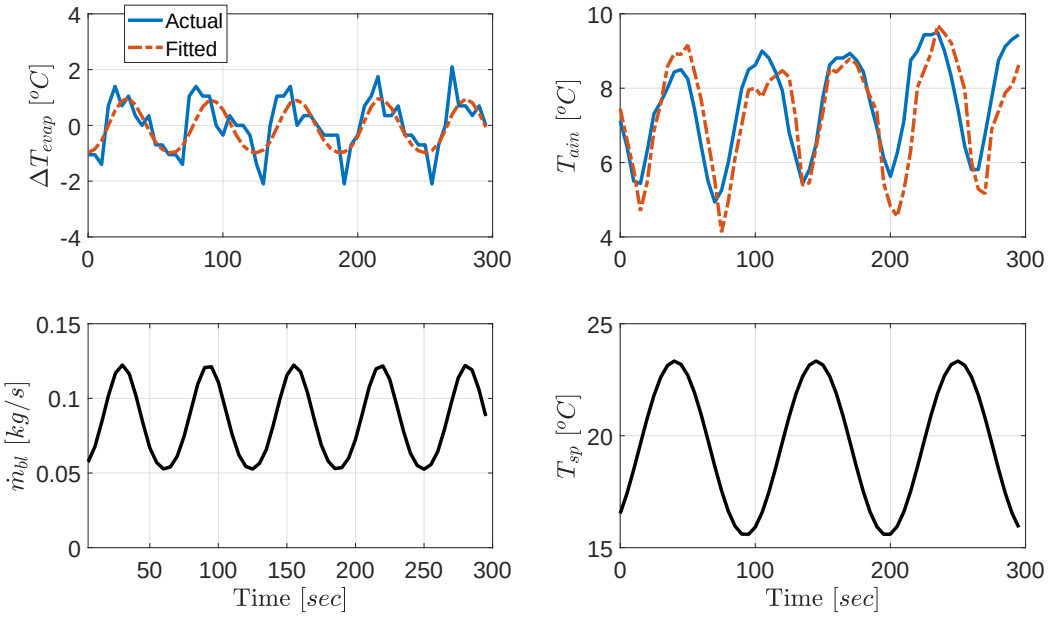

Figure 5.12: Model validation results of $\Delta T_{evap}(k) = T_{evap}(k+1) - T_{evap}(k)$ and $T_{ain}(k)$ for the sinusoidal excitations applied to the A/C system on test vehicle.

5.2.2 Eco-cooling Strategy and A/C Controls

The proposed eco-cooling strategy is determined by solving the following nonlinear optimization problem with the control-oriented model (Eqn. 5.4) used to predict the responses of the A/C system:

$$
\begin{aligned}
\min_{\substack{\dot{m}_{bl} \\ T_{sp}}} \quad & \sum_{i=0}^{N_p} \left\{ \left(P_{DACP}(i|k) - \beta(i|k) \cdot P_{DACP,targ}(i|k) \right)^2 \right\}, \\
\text{s.t.} \quad & T_{evap}(i+1|k) = f_{T_{evap}}(i|k), \\
& 0\ ^oC \leq T_{evap}(i|k) \leq 12^oC, \\
& 0.05\ kg/s \leq \dot{m}_{bl}(i|k) \leq 0.13\ kg/s, \\
& 16\ ^oC \leq T_{sp}(i|k) \leq 23\ ^oC, \\
& T_{evap}(0|k) = T_{evap}(k),
\end{aligned}
\tag{5.6}
$$

In (5.6), $(i|k)$ designates predicted values at the time instant $k+i$ when the prediction is made at the time instant k, while $f_{T_{evap}}$ is from Eqn. (5.4) and Eqn. (4.3). In the cost function, $P_{DACP}(i|k) = c_p(T_{amb}(i|k) - T_{ain}(i|k))\dot{m}_{bl}(i|k)$ and $\beta(k)$ is the design parameter. The main idea of this eco-cooling strategy is to leverage the sensitivity of the A/C system efficiency to vehicle speed which is accounted for by the design of speed dependent β. Fig. 5.13-(a) shows the dependence of β on the vehicle speed, V_{veh}. The increasing trend of β as V_{veh} increases represents the eco-cooling idea illustrated in Fig. 2.5. Detailed β values at different vehicle speeds are tuned by trial and error in order to match the overall same average P_{DACP} of the constant cooling case over the Plymouth driving cycle shown in Fig. 5.13-(b). This driving cycle was selected based on optimization of vehicle speed profile for a six intersection corridor at Plymouth Rd., Ann Arbor in [39]. The same driving cycle were used for the vehicle tests.

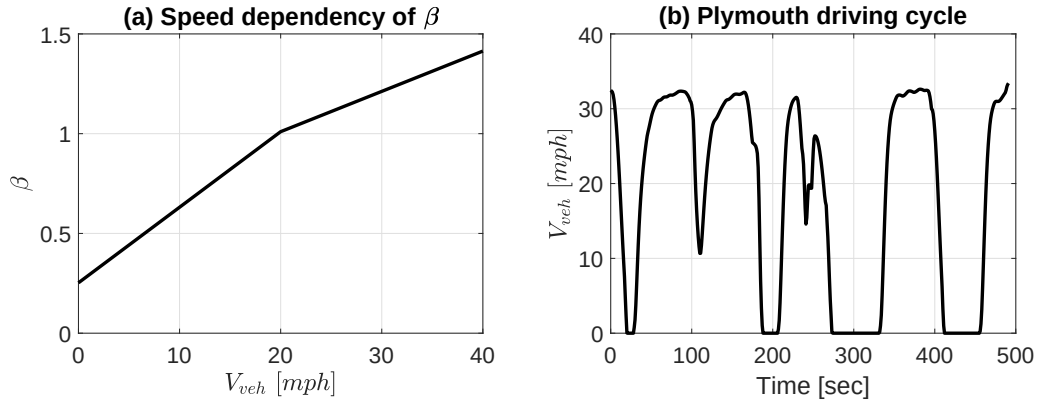

Figure 5.13: Speed-dependent β and Plymouth driving cycle.

Solving the optimization problem in (5.6) with respect to the control-oriented model renders the control inputs, $\dot{m}_{bl}$ and T_{sp}. The trajectories of the control inputs for the eco-cooling strategy are shown in Fig. 5.14. In addition, constant cooling control is selected for comparison. Note that in Fig. 5.14, the units of the two control inputs, $\dot{m}_{bl}$ and T_{sp}, are converted to percentage duty cycle (%) and degree Fahrenheit (^oF), respectively, which are direct control inputs to the vehicle A/C system.

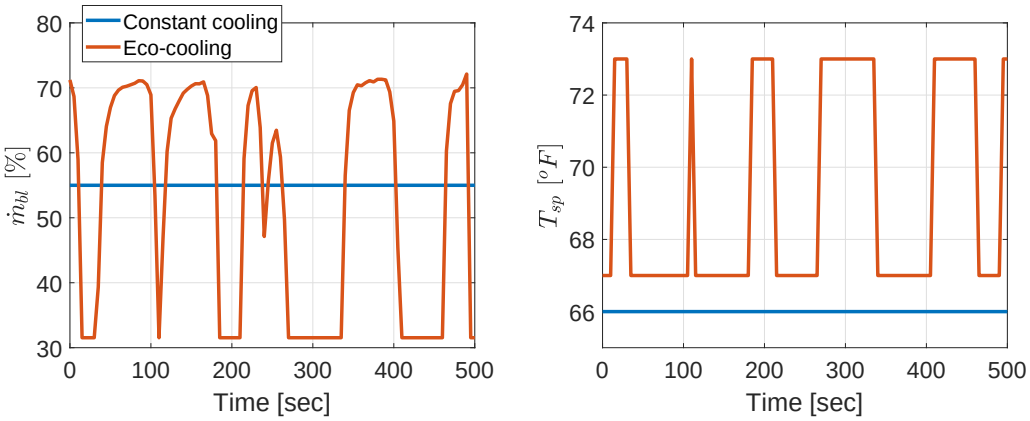

Figure 5.14: Control inputs for the constant cooling and eco-cooling cases.

5.3 Vehicle Tests on Open Road

The primary objective of the road tests is to demonstrate the energy saving of the proposed eco-cooling strategy with respect to the more conventional constant cooling strategy. In the comparison, the overall cooling performance of the two cases will also be quantified. In order to isolate the impact of the cabin thermal management, it is crucial that the uncertainties over different test trips are well-controlled, especially for the powertrain traction loss and cabin thermal conditions. To this end, the rest of this section discusses the testing procedures for the repeatable tests.

5.3.1 Route Selection

The road tests were performed over two different routes outside Ann Arbor. The locations of the two tests are shown in Fig. 5.15 and Fig. 5.16. Both routes are straight, with no stops and very little traffic so that we can emulate the Plymouth driving cycle shown in Fig. 5.13-b. The speed trajectory is followed by human-driver and the speed tracking performance will be presented later.

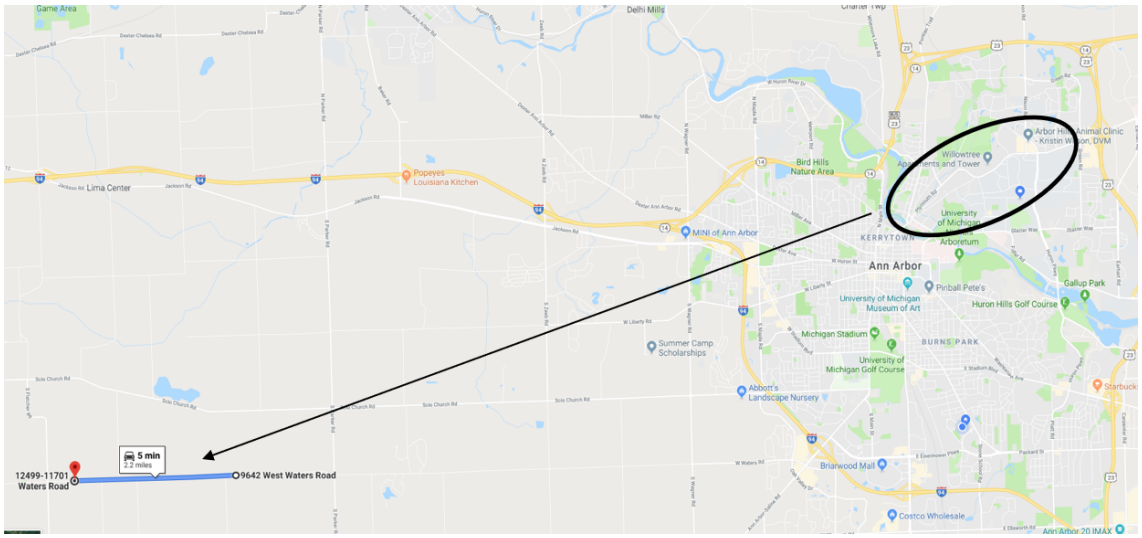

Figure 5.15: Route 1 along W. Waters Road with Plymouth corridor shown in the ellipse.

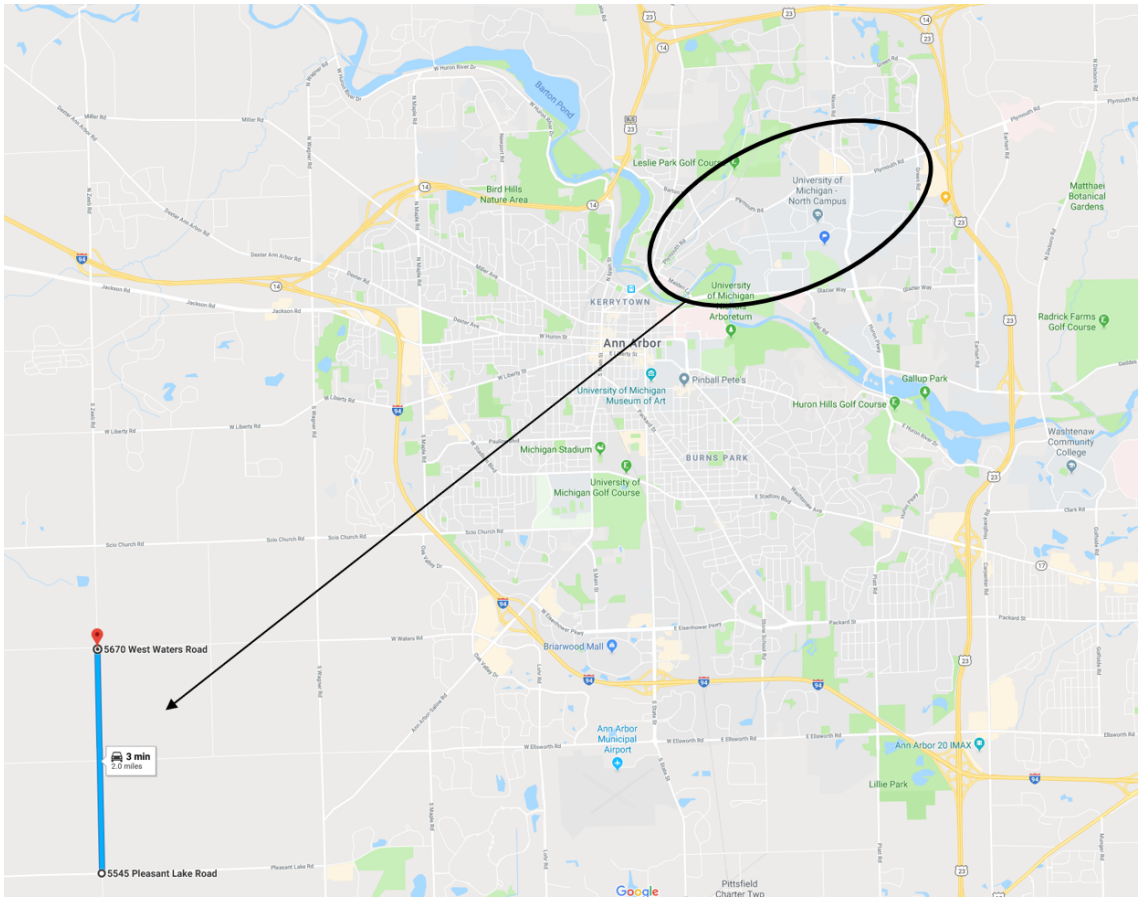

Figure 5.16: Route 2 along S. Zeeb Road with Plymouth corridor shown in the ellipse.

In terms of the road conditions, Route 1 is mostly flat but unpaved and Route 2 is paved but with larger deviations in road grade. The photos of the road conditions of the two routes are shown in Fig. 5.17.

Figure 5.17: Road conditions of the two testing routes.

5.3.2 Testing Process for Each Comparable Data Set

In our vehicle tests, we refer to a comparable data set as the set of tests that are performed sequentially in one day. For demonstrating the eco-cooling impact, a comparable data set consists of 3 consecutive trips following the Plymouth driving cycle, with the first one as the calibration test followed by the constant cooling test and the eco-cooling test. All three tests started at the same location. Between two tests, the vehicle cabin was fully ventilated using the ambient air when driving back to the starting location. At the beginning each test trip, vehicle cabin temperature was controlled to be at 30^oC. Note that the calibration test was utilized to conditioning the test vehicle, whose data will not be used for the energy consumption comparison.

5.3.3 Speed Tracking Performance Evaluation

In terms of vehicle testing on the open road, uncertainties associated with the speed tracking of desired driving cycle may affect the vehicle energy consumption. In order to improve

the speed tracking accuracy, an Matlab/Simulink® interface is created to guide the human driver. As shown in Fig. 5.18, both current vehicle speed (in red dots) and future speed preview (in blue line) are displayed on the testing laptop so that the drive will adjust the speed accordingly in real-time.

Figure 5.18: A vehicle test trip is ongoing along Route 1.

Fig. 5.19 provides an example of the speed trajectories for the tests performed on May 31^{st}, 2019. As can be seen from the comparison with the planned Plymouth driving cycle, the speed tracking error for all tests can be maintained within $2\ mph$ for most of the time. In addition, the average speed tracking error (e_{avg}) and the standard deviation of the speed tracking error (σ_{err}) for each test are listed in Table 5.3.3. As can be observed from the table, the average speed tracking error of each test is negligible while the standard deviation is well-controlled. The tests with similar speed tracking results to this example will be used to evaluate the energy consumption and cooling performance. The table summarizes the e_{avg} and σ_{err} for all the tests, in 18 comparable data sets, can be found in Appendix C. In Fig. 5.20, the box plot shows the statistical evaluations of the speed tracking performance for all eco-cooling tests.

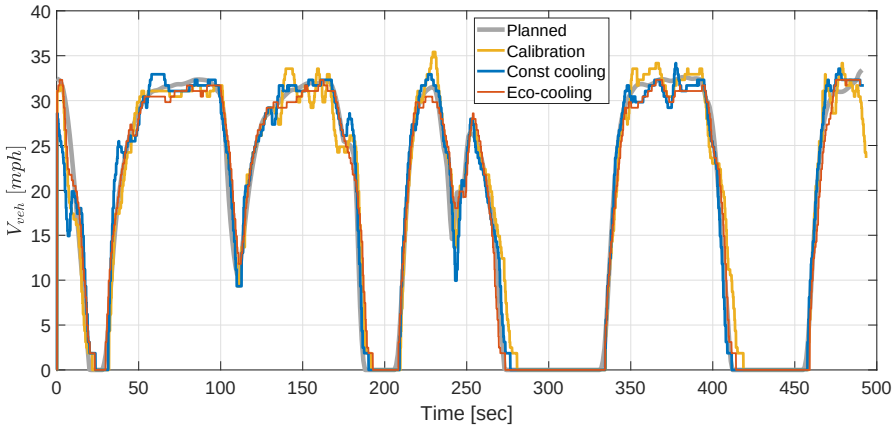

Figure 5.19: Vehicle speed trajectories for the tests performed on May 31^{st}, 2019.

Table 5.6: Average speed tracking error (e_{avg}) and the standard deviation of the speed tracking error (σ_{err}) for the tests performed on May 31^{st}, 2019.

	e_{avg} $[mph]$	σ_{err} $[mph]$
Calibration	0.24	2.52
Constant cooling	0.04	2.13
Eco-cooling	−0.11	1.98

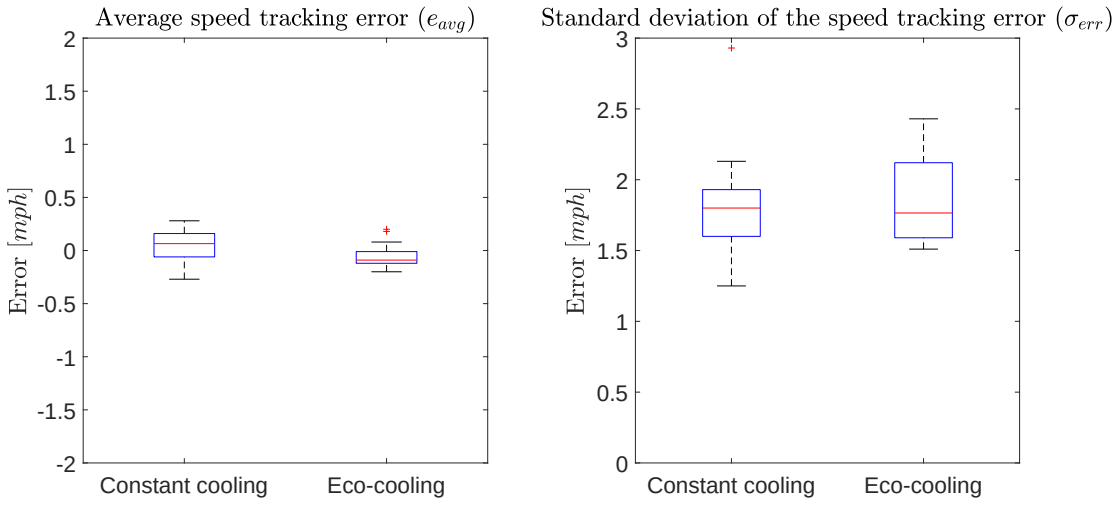

Figure 5.20: Statistical evaluations of the speed tracking performance for all the eco-cooling tests.

5.4 Experimental Results

5.4.1 Eco-cooling Impact

All the tests for demonstrating the eco-cooling impact were performed over the time period from May 23^{th} to September 5^{th} in 2019. The ambient air temperature during the testing period is within a large range between 22^oC to 34^oC. In total, 18 comparable data sets were collected (13 from the tests on Route 1 and 5 from the tests on Route 2). With well-controlled speed trajectories as presented in previous section, the average results of these 18 tests can demonstrate the impact of the proposed eco-cooling strategy.

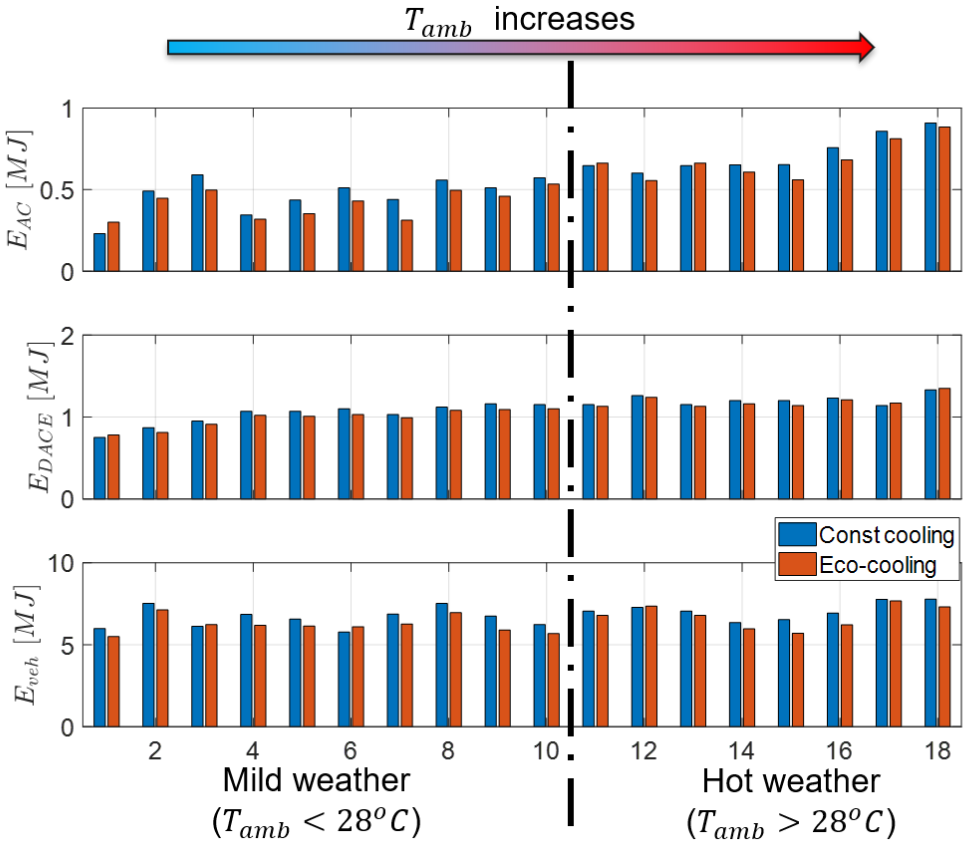

Figure 5.21: Energy consumptions and cooling performance of each test.

Fig. 5.21 plots the energy consumptions and cooling performance of all tests with constant cooling and eco-cooling. The energy consumptions consist of two metrics, E_{AC}

and E_{veh}, which represent the A/C system energy consumption and vehicle-level energy consumption, respectively. A/C system energy consumption is the integral of compressor power and blower power, which are measured. Vehicle-level energy consumption is computed based on Eqn. 5.1. In terms of the cooling performance, the discharge air cooling energy (DACE) is inherited from the PCS design, which is intended to quantify the overall cooling energy provided to the cabin over each test trip.For our vehicle tests, DACE is calculated as follows,

$$E_{DACE} = \int_0^T c_p \cdot (T_{amb}^{adj}(t) - T_{ain}(t)) \cdot \dot{m}_{bl}(t)\, dt. \tag{5.7}$$

In Eqn. 5.7, T is the duration of the Plymouth driving cycle, c_p is the specific heat capacity of air, T_{amb}^{adj} is adjusted ambient temperature measurement, which represents the temperature of the air entering the A/C system (i.e., before heat exchange with the evaporator). T_{amb}^{adj} is typically higher than the ambient air temperature (T_{amb}) considering extra heats picked up along the air path, where the heat energy mostly comes from the engine compartment. T_{ain} is the vent air temperature measured by the thermal couple located at the front vent shown in Fig. 5.1. $\dot{m}_{bl}$ is the blower air flow rate determined by the map in Fig. B.1. In Fig. 5.21, all 18 tests are sorted by the ambient air temperature and are separated into two groups, mild weather and hot weather, for further comparisons. As can be observed, as the ambient air temperature increases, the A/C system energy consumption increase dramatically. More importantly, for most cases, the eco-cooling strategy saves energy from the A/C system, which can translate into the vehicle-level energy saving. However, uncertainties associated with the road condition, powertrain control, and weather conditions, cannot be fully eliminated, which lead to several outliers in the results.

A more clear comparison can be seen from Fig. 5.22, where average energy consumptions and cooling performance are compared. Overall, the proposed eco-cooling strategy saves 8% of A/C system energy, which translates into 5.7% energy saving in vehicle-level at

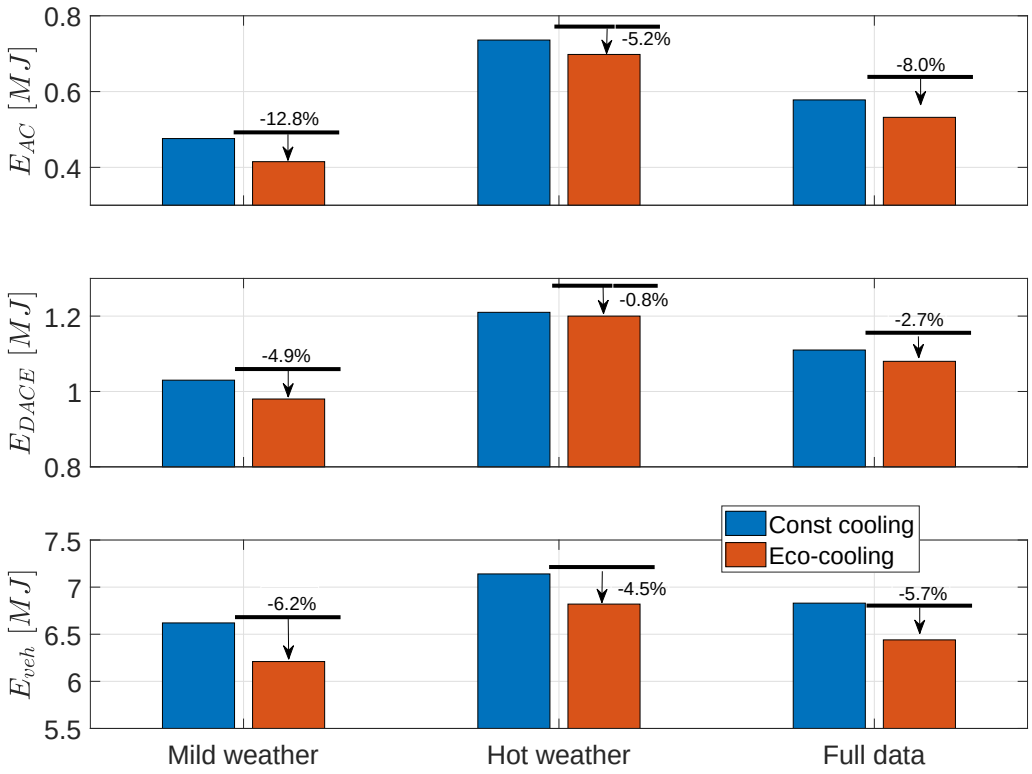

Figure 5.22: Comparison of average energy consumptions and cooling performance.

the cost of compromising the cooling performance by 2.7%. The energy saving is achieved by leveraging the A/C system efficiency to the vehicle speed. Comparing the results between mild weather and hot weather, we conclude that the impact of eco-cooling in hot weather is more pronounced than the one in mild weather. This conclusion is drawn based on the following observation that in mild weather, although eco-cooling saves much more A/C system energy in terms of percentage than in hot weather, the cooling performance is also considerably compromised, meanwhile the vehicle-level energy saving percentages are at the same level for both cases.

Regarding the comparison of detailed time histories of the system responses, Fig. 5.23 provides an example of the tests performed on May 31^{st} when it is sunny and the ambient air temperature is $27^{o}C$. As shown in Fig. 5.23-(d), the eco-cooling is achieved by coordi-

nating the A/C compressor power with respect to vehicle speed, while in constant cooling, the compressor power is relatively constant. Note that the trajectories of the average cabin temperature are similar for both cases. It is alsi worthy mentioning that the difference in the auxiliary power trajectories between the eco-cooling and constant cooling cases may trigger different powertrain control logic (e.g. power-split control). Whether the difference in powertrain control contributes to the 5.7% vehicle-level energy saving or not requires further investigations. This observation, in return, motivates the importance of the integrated analysis of vehicle power and thermal systems.

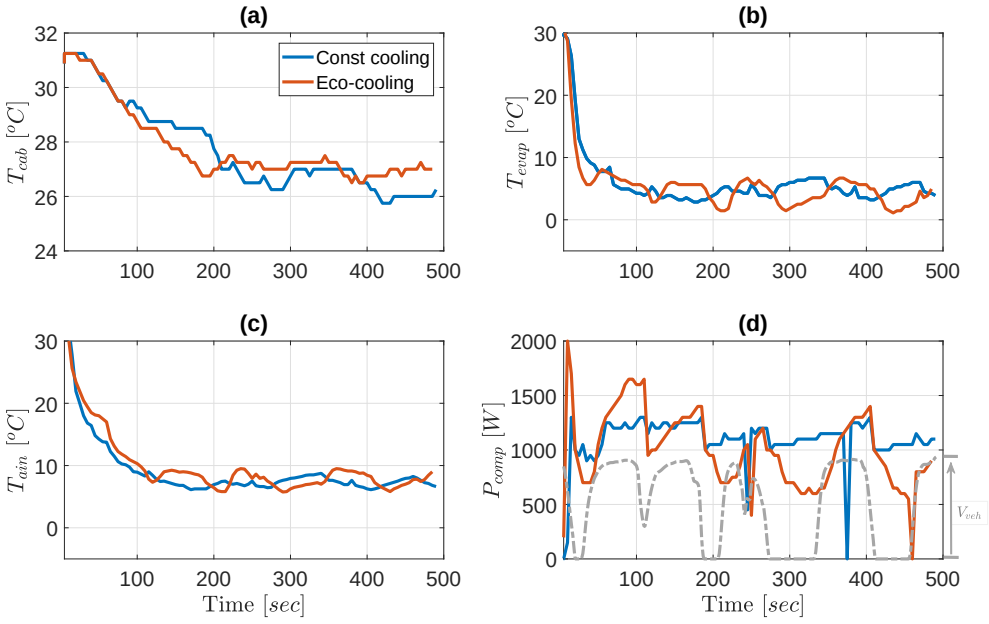

Figure 5.23: Time histories of the system responses for the tests performed on May 31^{st}, 2019.

5.4.2 Cabin Air Recirculation Impact

While the influence of cabin air recirculation on the air quality has been widely studied (see [66] and [67]), its impact on the A/C system and vehicle energy consumption is not clear. Besides the eco-cooling test results presented in previous section, additional vehicle tests have been performed on Route 2 for preliminary studies on the recirculation impact on the energy consumptions. The similar testing procedure was applied for comparing the eco-cooling over Plymouth driving cycle with recirculation on and off cases.

Table 5.7: Average energy consumptions for recirculation on and off cases.

	$E_{AC}\ [MJ]$	$E_{veh}\ [MJ]$
Recirculation off	0.385	6.54
Recirculation on	0.372	6.66

Table 5.4.2 summarizes the average energy consumptions from 5 comparable data sets collected under mild weather conditions from August 18^{th} to September 5^{th} in 2019. As shown in the energy consumption values, there is no clear energy consumption difference between recirculation on and off cases. Detailed system responses of the tests on August 25^{th} are plotted in Fig. 5.24. As shown in the figure, for this set of tests under mild weather ($T_{amb} = 25^oC$), the system behaviors are similar with and without recirculation. We conclude that the recirculation impact on vehicle energy consumptions is very limited under mild weather condition, however, whether the conclusion is still hold for the tests under hot weather conditions would require more investigations.

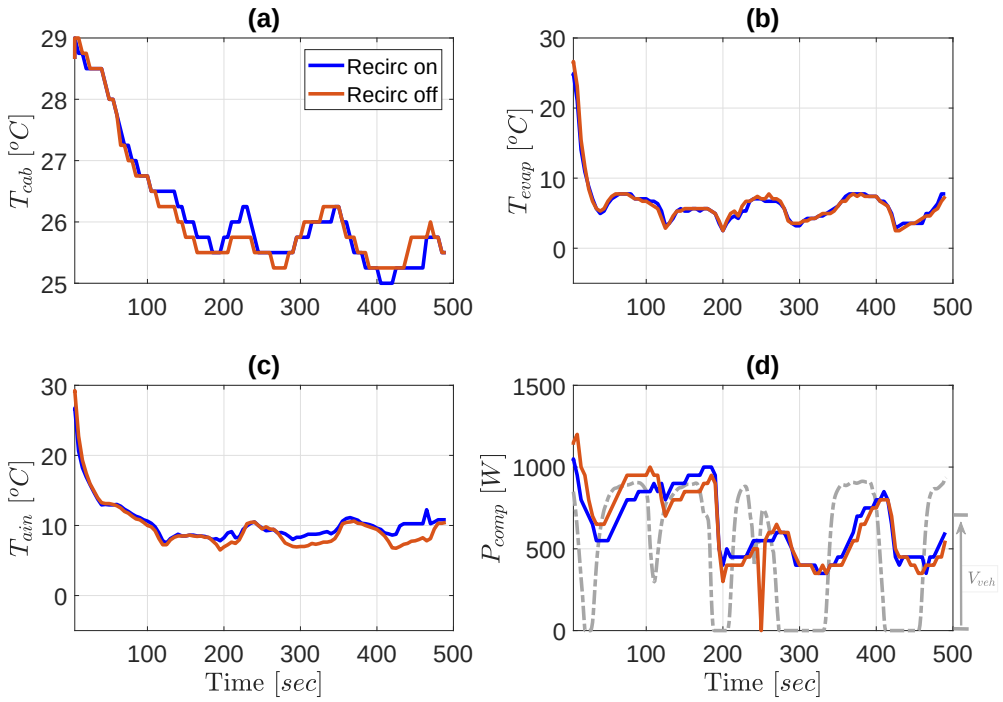

Figure 5.24: Vehicle system responses for the tests performed on August 25^{th}, 2019.

CHAPTER 6

Combined Energy and Comfort Optimization (CECO)

In Chapter 5, the vehicle testing results have been presented which confirms the effectiveness of the proposed eco-cooling strategy on vehicle-level energy saving. Such eco-cooling strategy coordinates the A/C operations with respect to the vehicle speed, taking advantage of the speed sensitivity of the A/C system efficiency. However, the implication of such A/C operation on OTC is not clear. To emphasize the impact of the eco-cooling on comfort, a more detailed OTC model is required. In this chapter, the OTC is is quantified by a modified PMV model adapted for an automotive application. Compared with the comfort metric proposed in Chapter 4, the PMV model proposed in this chapter is more comprehensive and explicitly handles the solar radiation, which is one of the most important factors regarding the OTC for automotive applications. Based on this more comprehensive metric, we propose a combined energy and comfort optimization (CECO) strategy for the air conditioning (A/C) system. By leveraging the weather and traffic predictions enabled by the emerging CAV technologies, the proposed strategy is able to minimize the A/C system energy consumption while maintaining the OTC within the comfort constraints. The benefits of energy consumption and OTC improvement will be demonstrated via closed-loop simulations on CoolSim.

6.1 Occupant Thermal Comfort (OTC) Modeling

In this section, we present the OTC model based on the modified PMV which accounts for multiple factors, including solar radiation and vent air temperature.

6.1.1 Original PMV Model

In the original PMV model for indoor spaces described in [68, 69], the PMV index computation exploits the following heat balance equation,

$$M - W_{mech} = H + E_c + C_{res} + E_{res}, \tag{6.1}$$

where M and W_{mech} represent the metabolic rate of the occupant and the effective mechanical power due to work performed by the occupant, respectively. The terms on the right of Eqn. (6.1), H, E_c, C_{res}, and E_{res} represent the dry heat loss, the evaporative heat exchange at skin, the respiratory convective heat exchange, and the respiratory evaporative heat exchange, respectively. All these variables are in units of W/m^2. When Eqn. (6.1) holds, the best OTC level is achieved. Otherwise, the occupant feels either warm or cold.

Inspired by this heat balance equation, the PMV index is calculated by [68, 70]:

$$\begin{aligned} y^*_{PMV} &= (0.303e^{-0.036M} + 0.028)[(M - W_{mech}) \\ &- (H + E_c + C_{res} + E_{res})], \end{aligned} \tag{6.2}$$

where,

$$\begin{aligned} H &= 3.96 \cdot 10^{-8} f_{cl}[(T_{cl} + 273)^4 - (T_{mr} + 273)^4] \\ &+ f_{cl} h_c (T_{cl} - T_a), \end{aligned} \tag{6.3}$$

$$\begin{aligned} E_c &= 3.05 \cdot 10^{-3}[5733 - 6.99 \cdot (M - W_{mech}) - p_a] \\ &+ 0.42(M - W_{mech} - 58.15), \end{aligned} \tag{6.4}$$

$$C_{res} = 0.0014M(34 - T_a), \tag{6.5}$$

$$E_{res} = 1.7 \cdot 10^{-5} M(5867 - p_a), \tag{6.6}$$

$$\begin{aligned} T_{cl} &= 35.7 - 0.0275(M - W_{mech}) - I_{cl}\{M - W_{mech} \\ &- 3.05[5.73 - 0.007(M - W_{mech}) - p_a] \\ &- 0.42(M - W_{mech} - 58.15) - 0.0173M(5.87 - p_a) \\ &- 0.0014M(34 - T_a)\}, \end{aligned} \tag{6.7}$$

$$h_c = \begin{cases} 2.38|T_{cl} - T_a|^{0.25}, & 2.38|T_{cl} - T_a|^{0.25} > 12.1\sqrt{V_{air}}, \\ 12.1\sqrt{V_{air}}, & 2.38|T_{cl} - T_a|^{0.25} \leq 12.1\sqrt{V_{air}}, \end{cases}$$

$$f_{cl} = \begin{cases} 1.05 + 0.645 I_{cl}, & I_{cl} > 0.078, \\ 1.00 + 1.29 I_{cl}, & I_{cl} \leq 0.078, \end{cases} \tag{6.8}$$

with T_{cl}, T_{mr}, T_a being the cloth surface temperature, the mean radiant temperature, and the air temperature (in ^oC), respectively. The constants (or variables) f_{cl}, h_c, I_{cl}, p_a, and V_{air} represent the clothing surface area factor, the convective heat transfer coefficient (in $W/(m^2 \cdot K)$), the clothing insulation (in $m^2 \cdot K/W$), the partial water vapor pressure (in Pa), and the relative air velocity (in m/s), respectively. Note that this model represents the comfort of an average people in population level. The model coefficients of this empirical

model may change when applied to a specific individual.

6.1.2 Modified PMV Model for Automotive Applications

In automotive applications, the passengers are subject to direct solar radiation and their thermal sensations are also influenced by the vent air velocity and temperature since they sit close to the vents. To account for these effects, modifications to the original PMV model are now proposed. Firstly, the heat balance equation Eqn. (6.1) is modified as

$$M + W_{rad} = H + E_c + C_{res} + E_{res}, \tag{6.9}$$

where W_{rad} represents the effective solar radiation power in the unit of W/m^2 and we assume $W_{mech} = 0$ since there is no mechanical work associated with the occupant sitting inside the cabin. Secondly, the PMV index computation by Eqn. (6.2) is modified to the following form:

$$\begin{aligned} y_{PMV} &= (0.303e^{-0.036M} + 0.028)[(M + W_{rad}) \\ &- (H + E_c + C_{res} + E_{res})], \end{aligned} \tag{6.10}$$

where H, E_c, C_{res}, and E_{res} are evaluated based on Eqns. (6.3)-(6.8) and with

$$T_a = \alpha_1 T_{cab} + \alpha_2 T_{ain}, \tag{6.11}$$

where α_1 and α_2 are the parameters introduced to account for the impact of T_{ain}. As compared to the original PMV model used in [71, 72], we introduced the new input W_{rad} to account for the solar radiation impact on the OTC and we combined the impacts of T_{cab} and T_{ain} in Eqn. (6.11) instead of using $T_a = T_{cab}$. In this work, several assumptions have been made in the y_{PMV} evaluation:

1. W_{rad} is time-varying depending on average solar radiation, cloud coverage, vehicle

orientation, etc. It is assumed to be known via V2X communications, e.g., using the approach in [73]. In the simulations, W_{rad} trajectory over the driving cycle is specified to qualitatively demonstrate the solar radiation impact on the OTC (i.e., the occupant tends to feel hotter as W_{rad} increases);

2. Similar to [49], we use the cabin interior temperature to represent the mean radiant temperature (i.e., $T_{mr} = T_{int}$), which is mainly used for capturing the radiative heat transfer of the human body to the cabin;

3. V_{air} is assumed to be only affected by $\dot{m}_{bl}$ so that V_{air} may be directly controlled. Furthermore, there is a prescribed linear mapping between $\dot{m}_{bl}$ and V_{air};

4. For simplicity, humidity control is not considered in current MPC design, therefore p_a is assumed to be constant ($1700\ Pa$) for the y_{PMV} evaluation.

Note that according to the original definition of the PMV index, $y_{PMV} = 0$, where y_{PMV} is defined by Eqn. (6.10), represents the best comfort level as the heat balance is achieved in Eqn. (6.9). The occupant feels warm or cold depending on whether y_{PMV} is positive or negative, respectively. In Table 6.1, the PMV-based thermal sensation level is determined according to [68].

Table 6.1: PMV-based occupant thermal sensation level.

y_{PMV}	Thermal sensation level
3	Hot
2	Warm
1	Slightly warm
0	Neutral
-1	Slightly cool
-2	Cool
-3	Cold

6.1.3 Occupant Thermal Comfort (OTC) Constraints

As illustrated in Fig. 6.1, the upper and lower bounds on y_{PMV} shown in the dotted black lines are assumed to be prescribed, which may depend on occupant's personal cooling preference. The comfort zone is defined as the region between the upper and lower bounds. The region complimentary to the comfort zone is referred to as the complain zone. We further define the case when y_{PMV} is above the upper bound as undercooling and the case when y_{PMV} is below the lower bound as overcooling. In the cooling case studied in this paper, the upper bound on y_{PMV} is time-varying to accommodate the realistic response of the A/C system in summer as it usually takes some time to cool down the cabin to the comfort level.

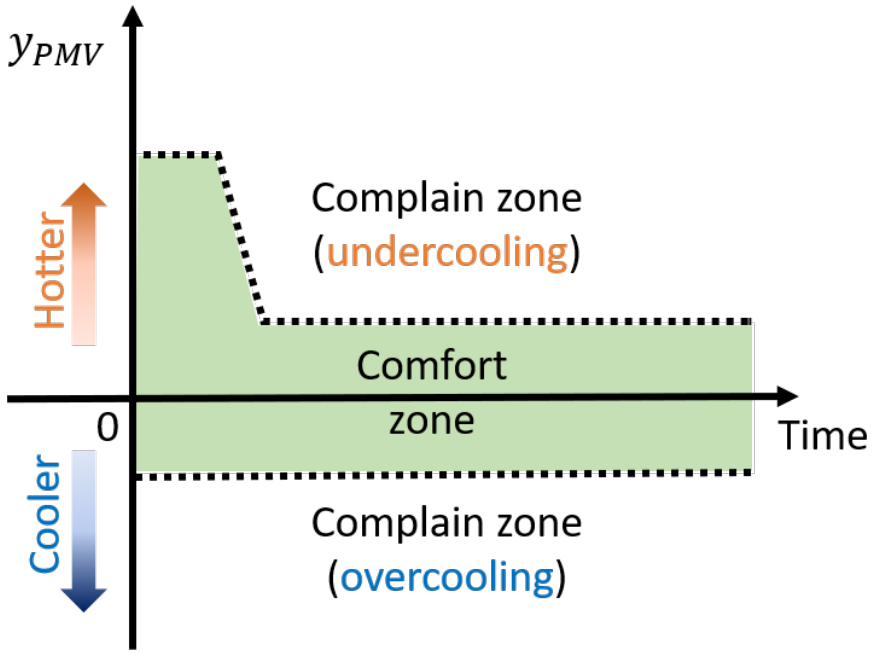

Figure 6.1: Illustration of the OTC constraints.

6.2 Problem Formulation of the CECO-based Strategies

6.2.1 General CECO Problem Formulation

The general CECO problem is formulated as follows with the objectives of minimizing the energy consumption while maintaining y_{PMV} within comfort zone:

$$
\begin{aligned}
\min_{\substack{\dot{m}_{bl}(\cdot|k) \\ T^{s.p.}_{evap}(\cdot|k)}} \quad & \sum_{i=0}^{N_p} \Big\{ P_{comp}(i|k) + P_{bl}(i|k) \Big\}, \\
\text{s.t.} \quad & T_{cab}(i+1|k) = f_{T_{cab}}(i|k),\ i = 0, \cdots, N_p, \\
& T_{evap}(i+1|k) = f_{T_{evap}}(i|k),\ i = 0, \cdots, N_p, \\
& y^{LB}_{PMV}(i|k) \le y_{PMV}(i|k) \le y^{UB}_{PMV}(i|k),\ i = 0, \cdots, N_p, \\
& T^{LB}_{evap}(i|k) \le T_{evap}(i|k) \le T^{UB}_{evap}(i|k),\ i = 0, \cdots, N_p, \\
& 0.05\ kg/s \le \dot{m}_{bl}(i|k) \le 0.17\ kg/s,\ i = 0, \cdots, N_p - 1, \\
& 3^oC \le T^{s.p.}_{evap}(i|k) \le 10^oC,\ i = 0, \cdots, N_p - 1, \\
& T_{cab}(0|k) = T_{cab}(k),\ T_{evap}(0|k) = T_{evap}(k),
\end{aligned}
\tag{6.12}
$$

where $(i|k)$ denotes the predicted value of the corresponding variable at time instant $k+i$ when the prediction is made at the time instant k, N_p represents the prediction horizon, the overall energy consumption of the A/C system is determined by the sum of compressor (P_{comp}) and blower (P_{bl}) powers in the cost function, $f_{T_{cab}}(i|k)$ and $f_{T_{evap}}(i|k)$ represent the major system dynamics as defined in Eqns. (3.1) and (3.2), y^{LB}_{PMV} and y^{UB}_{PMV} are the lower and upper bounds on y_{PMV}, and T^{LB}_{evap} and T^{UB}_{evap} are the lower and upper bound on T_{evap}, which account for the system operating limits. The lower and upper bounds on y_{PMV} applied in the simulation case studies over SC03 driving cycle are illustrated in Fig. 6.2. The upper and lower bounds on $\dot{m}_{bl}$ and $T^{s.p.}_{evap}$ are determined based on our particular A/C system operating limits. Note that in PMV-related studies [74], the comfort zone typically corresponds to $y^{LB}_{PMV} = -0.5$ and $y^{UB}_{PMV} = 0.5$.

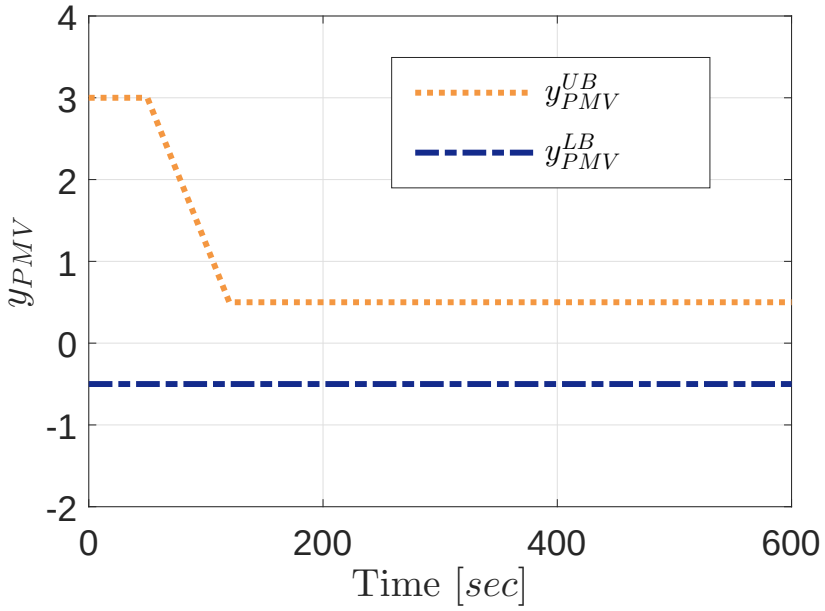

Figure 6.2: y_{PMV}^{UB} and y_{PMV}^{LB} over SC03 driving cycle.

6.2.2 CECO-E and CECO-C

Based on the general CECO problem formulation in Sec. 6.2.1, different variations in the controller design can be considered according to different objectives. To accommodate the trade-off between the energy consumption and the OTC, a modified cost function as compared to the one in (6.12) is proposed as follows,

$$\min_{\substack{\dot{m}_{bl}(\cdot|k) \\ T_{evap}^{s.p.}(\cdot|k)}} \quad \sum_{i=0}^{N_p} \Big\{ P_{comp}(i|k) + P_{bl}(i|k) + \gamma \cdot y_{PMV}^2(i|k) \Big\}, \tag{6.13}$$

where γ is the penalty on the deviation from $y_{PMV} = 0$, which represents the ideal OTC level. We further refer to the case when $\gamma = 0$ as **CECO with energy priority (CECO-E)** and refer to the case when γ equals to a large positive number (i.e., 10^5 in our case) as **CECO with comfort priority (CECO-C)**. Note that CECO-C is expected to consume more energy for providing better OTC level compared with CECO-E.

6.2.3 CECO with Intelligent Online Constraint Handling (CECO-IOCH)

As discussed in the previous section, better OTC can be achieved by adding a penalty term to the cost function of the general CECO problem, however, this may unnecessarily increase energy consumption. Here, we propose a more energy efficient approach for improving the OTC, which specifically leverages the vehicle speed preview. This approach is implemented by solving the following variation of the CECO problem with intelligent online constraint handling (IOCH), which is designated as **CECO-IOCH**.

$$
\begin{aligned}
\min_{\substack{\dot{m}_{bl}(\cdot|k)\\ T^{s.p.}_{evap}(\cdot|k)\\ \epsilon(\cdot|k)}} \quad & \sum_{i=0}^{N_p} \left\{ P_{comp}(i|k) + P_{bl}(i|k) + \beta\Big(\frac{\eta_{AC}(i|k)-1}{\epsilon(i|k)+\xi}\Big) \right\}, \\
\text{s.t.} \quad & T_{cab}(i+1|k) = f_{T_{cab}}(i|k),\ i=0,\cdots,N_p, \\
& T_{evap}(i+1|k) = f_{T_{evap}}(i|k),\ i=0,\cdots,N_p, \\
& y^{LB}_{PMV}(i|k) \le y_{PMV}(i|k) \le y^{UB}_{PMV}(i|k) - \epsilon(i|k),\ i=0,\cdots,N_p, \\
& T^{LB}_{evap}(i|k) \le T_{evap}(i|k) \le T^{UB}_{evap}(i|k),\ i=0,\cdots,N_p, \\
& 0.05\ kg/s \le \dot{m}_{bl}(i|k) \le 0.17\ kg/s,\ i=0,\cdots,N_p-1, \\
& 3^oC \le T^{s.p.}_{evap}(i|k) \le 10^oC,\ i=0,\cdots,N_p-1, \\
& 0 \le \epsilon(i|k) \le \epsilon^{UB},\ i=0,\cdots,N_p-1, \\
& T_{cab}(0|k) = T_{cab}(k),\ T_{evap}(0|k) = T_{evap}(k),
\end{aligned}
\tag{6.14}
$$

where $\eta_{AC} \ge 1$ is an efficiency multiplier [38], which is a function of the vehicle speed (larger value of η_{AC} represents higher efficiency in A/C system), β, ξ, and ϵ^{UB} represent the weighing factor, the regularity term, and the constant upper bound on ϵ, respectively. When compared with the problem formulation in (6.12), an additional optimization variable $\epsilon(i|k)$ is introduced and calculated online to actively tighten $y^{UB}_{PMV}(i|k)$ considering the speed sensitivity of the A/C system efficiency [21]. The basic idea of CECO-IOCH is tightening $y^{UB}_{PMV}(i|k)$ to provide better OTC only when A/C system is operating in high

efficiency regions (i.e., high vehicle speed regions). By utilizing this speed sensitivity, better energy efficiency may be achieved while maintaining the same OTC level. This IOCH mechanism was first proposed in [38] for tightening the constraint on T_{cab} based on the same speed sensitivity exploited here. $y_{PMV}^{UB}(i|k)$ and $y_{PMV}^{LB}(i|k)$ used in CECO-IOCH case are the same as the ones applied in the general CECO problem. Note that CECO-IOCH leverages both weather (W_{rad}) and traffic (V_{veh}) preview information while CECO-E and CECO-C only utilize the weather prediction. The NMPC problems (6.12)–(6.14) are solved numerically using the MPCTools package [64]. This package exploits CasADi [65] for automatic differentiation and IPOPT algorithm for the numerical optimization.

6.3 Simulation Results and Performance Evaluation of the CECO-based Strategies

In order to compare with the CECO-based designs (i.e., CECO-E, CECO-C, and CECO-IOCH), a baseline strategy is defined by applying a PI anti-windup controller to track a constant cabin temperature set-point. This baseline strategy represents a more conventional A/C system control strategy, which considers the average cabin temperature as the only measure of the OTC. The implementation of CECO-based MPC controller in closed-loop with CoolSim model is illustrated in Fig. 6.3, which takes the measurements from the CoolSim model, the OTC evaluation, the weather and traffic predictions as inputs and updates the controls of the A/C system. The three design scenarios are implemented by solving variations of the general CECO problem in (6.12). The MPC controller is updated at the sampling time $T_s = 5\ sec$ with prediction horizon $N_p = 6$. The weather (W_{rad}) and traffic (V_{veh}) previews are assumed to be known over the prediction horizon. Their trajectories over SC03 cycle are shown in Fig. 6.4.

In Fig. 6.5, the time histories of major system outputs based on the closed-loop simulations with the CoolSim model are shown for different control strategies. In Fig. 6.5-(a)

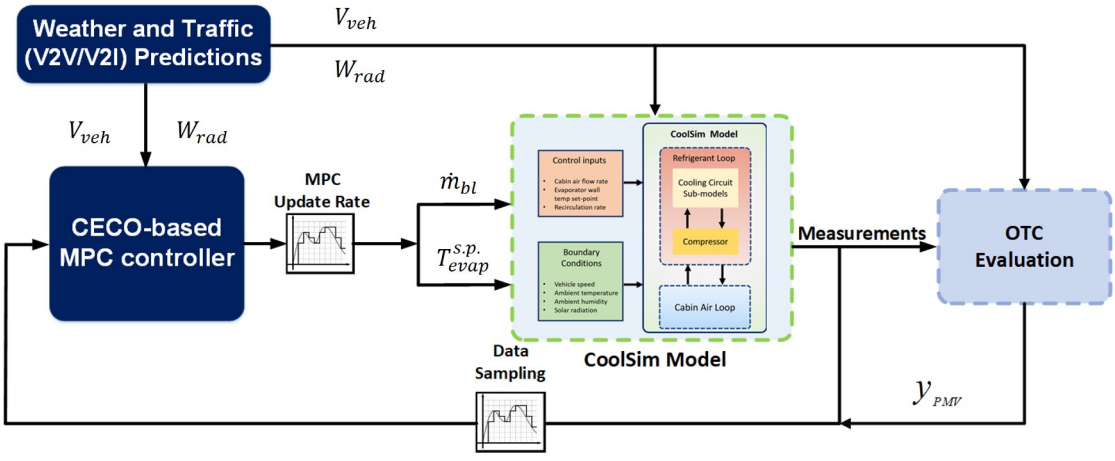

Figure 6.3: Schematic of implementing CECO-based MPC controller with CoolSim model in Simulink®.

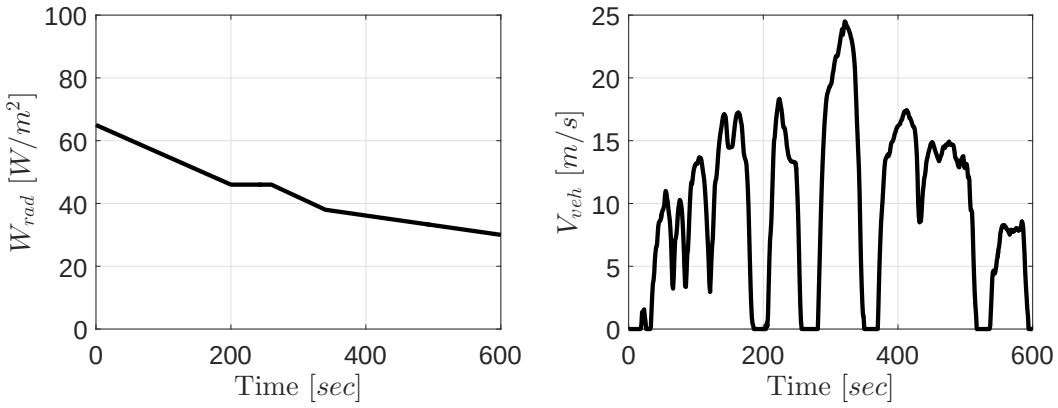

Figure 6.4: Weather and traffic preview information for the case studies, which are assumed available via CAV technologies.

which shows the y_{PMV} trajectories, the hard constraints on the OTC are plotted in dotted black lines. It is shown that the baseline controller regulates T_{cab} to track the set-point ($26\ ^oC$), however, according to y_{PMV}, this baseline strategy violates the OTC constraints for a significant amount of time, leading to both undercooling and overcooling cases. In comparison, all CECO-based control designs are able to overall maintain the OTC within the comfort zone. The energy and comfort comparisons of these four cases are provided in Fig. 6.6. The total A/C energy consumption (E_{tot}) over the simulation time T is calculated by

$$E_{tot} = \int_{t=0}^{T} (P_{comp}(t) + P_{bl}(t))dt. \tag{6.15}$$

To quantify the OTC level, two metrics are considered: I_{PMV} is defined as

$$I_{PMV} = \int_{t=0}^{T} y_{PMV}^2(t)dt, \tag{6.16}$$

and OTC violation is defined as

$$\text{OTC violation} = \frac{\tilde{T}}{T} \times 100\%, \tag{6.17}$$

where,

$$\tilde{T} = \{ \int_{t=0}^{T} x(t)dt \Big| \tag{6.18}$$

$$x(t) = \begin{cases} 1 : \text{if } y_{PMV}(t) > y_{PMV}^{UB}(t) \text{ or } y_{PMV}(t) < y_{PMV}^{LB}(t), \\ 0 : \text{otherwise}, \end{cases} \}.$$

As shown in Fig. 6.6, comparing CECO-E with the baseline strategy, the energy consumption of the A/C system is reduced by 15.9%, and lower OTC violation is achieved with higher I_{PMV} value. When CECO-C is applied, 4.1% energy is saved compared with the baseline strategy, meanwhile, lower values in I_{pmv} and OTC violation indicate that better comfort level has also been achieved. By comparing the CECO-IOCH results with the CECO-C, the benefit of incorporating traffic preview information is demonstrated. While CECO-IOCH design provides similar OTC level, it saves more energy by exploiting the speed sensitivity of the A/C system efficiency. Note that the OTC violations in CECO-C and CECO-IOCH are all from the initial responses at the very beginning of the cycle while in CECO-E, due to model mismatch, operating close to the constraint leads to higher OTC violation which may occur at certain instants over the entire simulation period. CECO-based designs save energy by avoiding the overcooling, which consumes energy and compromises the comfort. In our simulation case studies, as W_{rad} gradually decreases (shown in Fig. 6.4), the CECO-based designs coordinate with the trend of W_{rad} and decrease the A/C usage accordingly while enforcing the OTC constraints.

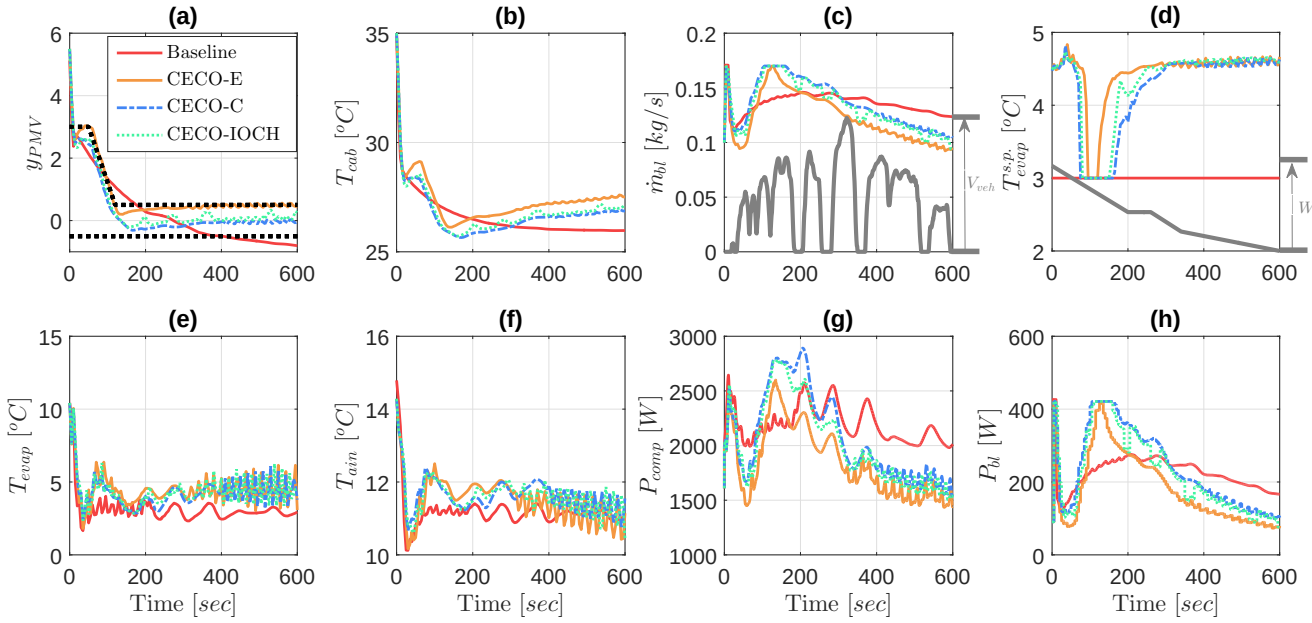

Figure 6.5: Simulation results from CoolSim model when comparing different CECO-based designs with the baseline strategy.

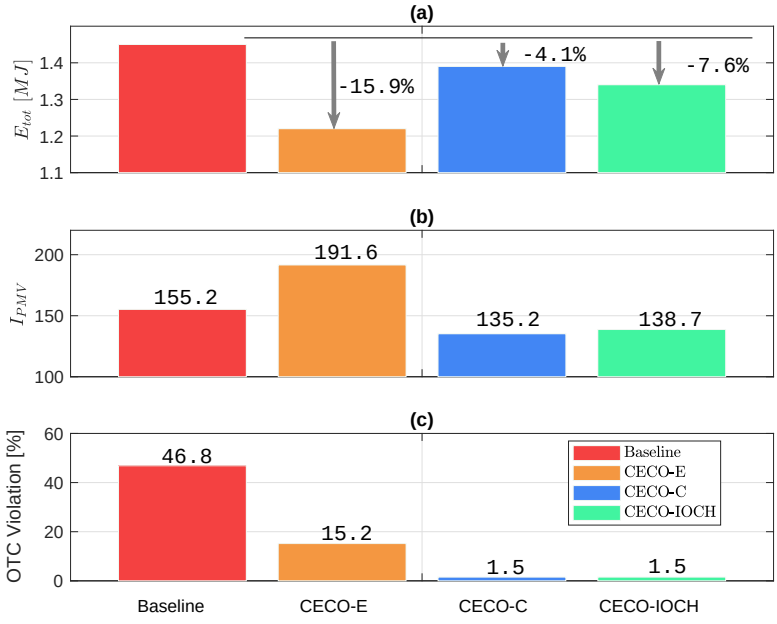

Figure 6.6: A/C system energy consumption and the OTC comparisons.

To further validate the impact of the proposed CECO-based strategy on vehicle level energy consumption, we utilize the same powertrain model from [38], which was developed and partially experimentally validated against a Prius HEV (MY 2017) data. For the validation, the same powertain controller is applied with the A/C power trajectories from different design cases shown in Fig. 6.5. As can be seen from Fig. 6.7, CECO-E, CECO-C, and CECO-IOCH reduce the vehicle energy consumption by 6.4%, 1.8%, and 3.1%, respectively, when compared with the baseline strategy over the SC03 driving cycle.

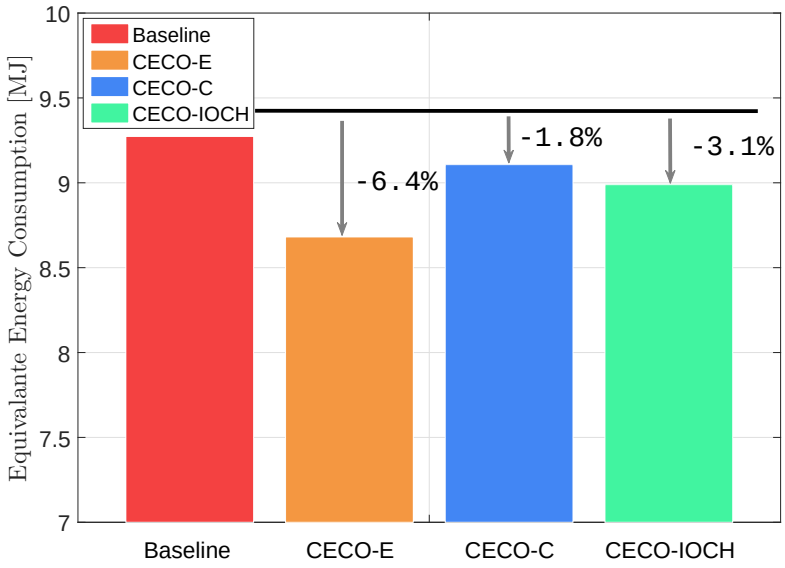

Figure 6.7: Vehicle-level equivalent energy consumption comparison.

CHAPTER 7

Conclusions and Future Work

7.1 Conclusions

Motivated by recent progress in CAV-related research for improving vehicle energy efficiency, this dissertation has been focusing on developing efficient thermal management strategies for the automotive climate control system. Three novel MPC-based A/C management strategies has been proposed depending on different OTC assumptions, robustness considerations, and implementation complexities on the testing vehicle.

The first strategy, the hierarchical optimization, exploits a two-layer H-MPC design for handling the potential uncertainties associated with the predictive information over long horizon. It has been demonstrated in simulations over different driving cycles that, by leveraging the vehicle speed sensitivity of the A/C system efficiency, the vehicle energy consumption can be reduced while maintaining the cabin temperature within the constraints when compared with a baseline of tracking constant cabin temperature.

The second strategy, the PCS, considers a more practical metric, DACP, for quantifying the comfort level instead of the cabin temperature. The simulation results in closed-loop with an industrial-level A/C system model shows that, the proposed PCS saves 4.9% of the A/C energy consumption over SC03 driving cycle when compared with an OEM calibrated benchmark. It is also demonstrated that by coordinating with future vehicle speed and shifting the A/C power load, the A/C energy consumption can be further reduced. Compared

with hierarchical optimization, the PCS has much simpler structure and is more suitable for the vehicle demonstration. Therefore, inspired by the PCS, an off-line eco-cooling controls for the A/C system have been computed and tested on an HEV for open road tests. The results of 18 repeatable testing cases show that, over a real-world driving cycle, the eco-cooling contributes to 8% A/C system energy saving, which translates to 5.7% vehicle-level energy saving at the cost of slightly compromised overall cooling performance.

In the third strategy, the CECO, a comprehensive OTC model is developed and incorporated into the optimal control problem. In simulations, it has been shown that, besides leveraging the speed sensitivity of the A/C system efficiency, additional vehicle energy saving can be achieved with improved the OTC level by avoiding the over-cooling,.

Above all, in this dissertation, we've discovered the dynamic coupling between the thermal and power systems, focused on leveraging the special characteristics of the automotive HVAC system to facilitate the iPTM design, developed real-time implementable algorithms to perform the energy and comfort optimizations, and demonstrated the energy saving benefits via repeatable vehicle tests.

7.2 Future Work

Future working directions beyond the scope of this dissertation may include the following two aspects:

- **Generalized iPTM to other thermal systems:** This dissertation addresses the iPTM problem with respect to the A/C system, which is one of the vehicle thermal subsystems. The energy saving benefits in the context of CAV has not been fully explored for other thermal management systems in electrified vehicles, such as those for engine, battery, and electric machine. Even within the climate control system, the heating counterpart has not been fully investigated. The optimal control problem for the heating system can be more interesting since multiple heat sources can be involved for future electrified vehicle, such as the engine coolant, Positive Temperature Coefficient (PTC) heater, and heat pump. Robust control solutions within each thermal subsystem as well as for the integration with the power system are required for future CAV design.

- **Adaptive comfort optimization considering occupant feedback**: In this dissertation, the proposed combined energy and comfort optimization renders the solution assuming that the personal comfort model is accurately known as priori. However, in practice, each individual may have personal preference and the personal comfort requirement may also change with time. To this end, it is necessary to make the comfort optimization adaptive to the occupant's feedback while still preserve the capability of leveraging the speed sensitivity of the system efficiency. Besides the adaptive design, the validation of a nominal OTC model for an average person is still a challenging work considering the complex cabin thermal environment. Eventually, a personalized efficient climate control would be ideal for future CAVs.

APPENDIX A

List of Vehicle Onboard Measurements

The following list provide the information of all available onboard measurements of the testing vehicle, which are used for the system analysis and control design. Note that the "control signal" of the list indicates whether the signal can be directly controlled in real-time for the HVAC system via the testing laptop.

Table A.1: List of vehicle onboard measurements.

Signal Name	**Unit**	**Notation**	**Control signal?**
Cabin temperature setpoint	^oF	T_{sp}	Y
HVAC blower flow	$\%$	$\dot{m}_{bl}$	Y
Blend door positon	Enum	na	Y
A/C on/off Commend	Boolean	na	Y
Rear HVAC on/off	Boolean	na	Y
Recirculation on/off	Boolean	na	Y
ECO mode on/off	Boolean	na	Y
Rear defrost on/off	Boolean	na	Y
Front defrost on/off	Boolean	na	Y
Auto mode on	Boolean	na	Y
HVAC off	Boolean	na	Y
Engine speed	RPM	N_{eng}	N
Engine torque	Nm	τ_{eng}	N
Equivalent air/fuel ratio	na	λ	N
Engine mass air flow	g/s	$\dot{m}_{air}$	N

Signal Name	Unit	Notation	Control signal?
Engine coolant pump speed	RPM	N_{cl}	N
Engine coolant temperature	^oC	T_{cl}	N
Catalyst temp	^oC	T_{cat}	N
Vehicle speed	kph	V_{veh}	N
Vehicle acceleration	m/s^2	a_{veh}	N
Vehicle yaw rate	deg/s	ω_{yaw}	N
Accelerator pedal position	$\%$	na	N
Master cylinder control torque	Nm	na	N
Front left wheel speed	kph	V_{fl}	N
Front right wheel speed	kph	V_{fr}	N
Rear left wheel speed	kph	V_{rl}	N
Rear right wheel speed	kph	V_{rr}	N
Steering angle	deg	α_{steer}	N
Adjusted ambient temperature	^oC	T_{amb}^{adj}	N
Cabin temperature	^oC	T_{cab}	N
Glass temperature	^oC	T_{gl}	N
A/C compressor speed	RPM	N_{comp}	N
Evaporator fin temperature	^oC	T_{evap}	N
A/C compressor power	W	P_{comp}	N
HVAC blower power	W	P_{bl}	N
Vehicle throttle position	$\%$	na	N
Traction motor speed	RPM	N_{mg1}	N
Traction motor torque	Nm	τ_{mg1}	N
Generator speed	RPM	N_{mg2}	N
Generator torque	Nm	τ_{mg2}	N
Battery voltage	V	V_{batt}	N
Battery current	A	I_{batt}	N
Battery SOC	$\%$	SOC	N
Battery temp	^oC	T_{batt}	N
Battery resistance	Ω	R_{batt}	N
Battery cooling inlet temp	^oC	$T_{batt,in}$	N
Battery cooling outlet temp	^oC	$T_{batt,out}$	N
Cabin interior roof temp	^oC	T_{roof}	N
Dashboard skin temp	^oC	T_{dash}	N
Vent air temp	^oC	T_{vent}	N

APPENDIX B

HVAC Blower Air Flow Map

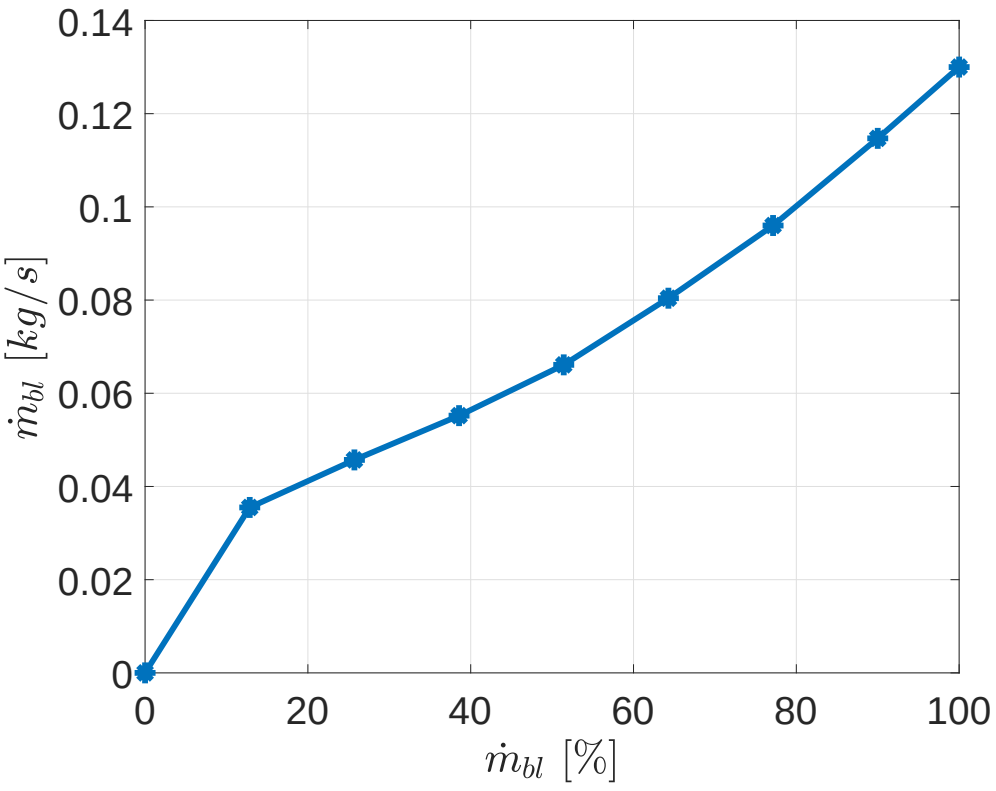

Figure B.1: HVAC blower air flow map.

Fig. B.1 shows the map that converts the HVAC blower flow rate between percentage PWM control signal and the actual flow rate into the cabin in kg/s. This map is calibrated via the experiments of the third party. Note that this map is validated for the case with the blend door position at the vent position (i.e. air comes in front of the driver) and with no

cabin air recirculation, which is the case for the eco-cooling tests. While the blend door position changes or the recirculation is on, due to the back-pressure changes, the same percentage PWM control signal of the HVAC blower may results in different air flow rates into the cabin. In addition, since the calibration experiments were performed in a well-controlled lab environment, the uncertainties associated with the ambient conditions for the open road tests, such as temperature, pressure, and humidity, may also affect the actual air flow rate into the cabin.

APPENDIX C

Speed Tracking Performance Evaluation for Eco-cooling Tests

Table C.1: Speed tracking performance evaluation fro all eco-cooling tests.

Date	**Test case**	e_{avg}	σ_{err}
23-May	1	0.17	1.98
	2	0.19	1.93
	3	0.20	2.04
25-May	1	-0.04	1.95
	2	-0.22	2.03
	3	-0.17	2.35
31-May	1	0.24	2.52
	2	0.04	2.13
	3	-0.11	1.98
9-Jun	1	-0.46	1.75
	2	-0.09	1.60
	3	-0.10	1.80
3-Jun	1	-0.14	1.96
	2	0.16	1.54
	3	-0.01	2.43
7-Jul	1	0.05	1.56
	2	-0.04	1.80
	3	0.05	1.55
14-Jul	1	0.05	1.56
	2	-0.04	1.80
	3	-0.05	1.55
19-Jul	1	-0.41	3.55
	2	-0.08	1.98
	3	-0.11	1.51

Date	**Test case**	e_{avg}	σ_{err}
20-Jul	1	0.15	1.47
	2	0.19	1.61
	3	0.18	1.72
28-Jul	1	-0.01	1.80
	2	-0.06	1.54
	3	-0.05	1.68
4-Aug	1	-0.13	1.54
	2	0.09	1.25
	3	-0.20	1.63
10-Aug	1	-0.27	1.43
	2	0.06	1.70
	3	-0.12	1.81
11-Aug	1	0.62	1.93
	2	0.28	1.80
	3	-0.15	2.40
18-Aug	1	0.07	2.09
	2	0.12	1.84
	3	-0.05	1.73
25-Aug	1	0.09	1.99
	2	-0.27	2.93
	3	-0.10	2.12
30-Aug	1	-0.02	2.07
	2	0.07	1.49
	3	-0.08	2.33
2-Sep	1	0.12	1.61
	2	0.22	1.91
	3	0.08	1.55
5-Sep	1	0.17	1.57
	2	0.12	1.71
	3	-0.20	1.59

BIBLIOGRAPHY

[1] Shladover, S. E., "Connected and automated vehicle systems: Introduction and overview," *Journal of Intelligent Transportation Systems*, Vol. 22, No. 3, 2018, pp. 190–200.

[2] Rios-Torres, J. and Malikopoulos, A. A., "A survey on the coordination of connected and automated vehicles at intersections and merging at highway on-ramps," *IEEE Transactions on Intelligent Transportation Systems*, Vol. 18, No. 5, 2016, pp. 1066–1077.

[3] Bevly, D., Cao, X., Gordon, M., Ozbilgin, G., Kari, D., Nelson, B., Woodruff, J., Barth, M., Murray, C., Kurt, A., et al., "Lane change and merge maneuvers for connected and automated vehicles: A survey," *IEEE Transactions on Intelligent Vehicles*, Vol. 1, No. 1, 2016, pp. 105–120.

[4] Zhang, Y. J., Malikopoulos, A. A., and Cassandras, C. G., "Optimal control and coordination of connected and automated vehicles at urban traffic intersections," *2016 American Control Conference (ACC)*, IEEE, 2016, pp. 6227–6232.

[5] Malikopoulos, A. A., Cassandras, C. G., and Zhang, Y. J., "A decentralized energy-optimal control framework for connected automated vehicles at signal-free intersections," *Automatica*, Vol. 93, 2018, pp. 244–256.

[6] Vahidi, A. and Sciarretta, A., "Energy saving potentials of connected and automated vehicles," *Transportation Research Part C: Emerging Technologies*, Vol. 95, 2018, pp. 822–843.

[7] Jiang, H., Hu, J., An, S., Wang, M., and Park, B. B., "Eco approaching at an isolated signalized intersection under partially connected and automated vehicles environment," *Transportation Research Part C: Emerging Technologies*, Vol. 79, 2017, pp. 290–307.

[8] Guanetti, J., Kim, Y., and Borrelli, F., "Control of connected and automated vehicles: State of the art and future challenges," *Annual reviews in control*, Vol. 45, 2018, pp. 18–40.

[9] Stephens, T., Gonder, J., Chen, Y., Lin, Z., Liu, C., and Gohlke, D., "Estimated bounds and important factors for fuel use and consumer costs of connected and automated vehicles," Tech. rep., National Renewable Energy Lab.(NREL), Golden, CO (United States), 2016.

[10] Barth, M. and Boriboonsomsin, K., "Energy and emissions impacts of a freeway-based dynamic eco-driving system," *Transportation Research Part D: Transport and Environment*, Vol. 14, No. 6, 2009, pp. 400–410.

[11] Asadi, B. and Vahidi, A., "Predictive cruise control: Utilizing upcoming traffic signal information for improving fuel economy and reducing trip time," *IEEE transactions on control systems technology*, Vol. 19, No. 3, 2010, pp. 707–714.

[12] Dib, W., Chasse, A., Moulin, P., Sciarretta, A., and Corde, G., "Optimal energy management for an electric vehicle in eco-driving applications," *Control Engineering Practice*, Vol. 29, 2014, pp. 299–307.

[13] Sciarretta, A., De Nunzio, G., and Ojeda, L. L., "Optimal ecodriving control: Energy-efficient driving of road vehicles as an optimal control problem," *IEEE Control Systems Magazine*, Vol. 35, No. 5, 2015, pp. 71–90.

[14] Yi, Z., Smart, J., and Shirk, M., "Energy impact evaluation for eco-routing and charging of autonomous electric vehicle fleet: Ambient temperature consideration," *Transportation Research Part C: Emerging Technologies*, Vol. 89, 2018, pp. 344–363.

[15] Setlur, P., Wagner, J. R., Dawson, D. M., and Marotta, E., "An advanced engine thermal management system: Nonlinear control and test," *IEEE/ASME transactions on mechatronics*, Vol. 10, No. 2, 2005, pp. 210–220.

[16] Karnik, A. Y., Fuxman, A., Bonkoski, P., Jankovic, M., and Pekar, J., "Vehicle powertrain thermal management system using model predictive control," *SAE International Journal of Materials and Manufacturing*, Vol. 9, No. 3, 2016, pp. 525–533.

[17] Cloudt, R. and Willems, F., "Integrated emission management strategy for cost-optimal engine-aftertreatment operation," *SAE International Journal of Engines*, Vol. 4, No. 1, 2011, pp. 1784–1797.

[18] Feru, E., Murgovski, N., de Jager, B., and Willems, F., "Supervisory control of a heavy-duty diesel engine with an electrified waste heat recovery system," *Control Engineering Practice*, Vol. 54, 2016, pp. 190–201.

[19] Xia, G., Cao, L., and Bi, G., "A review on battery thermal management in electric vehicle application," *Journal of power sources*, Vol. 367, 2017, pp. 90–105.

[20] Snyder, K. L. and Ku, J., "Optimization for plug-in vehicles-waste heat recovery from the electric traction motor," Tech. rep., SAE Technical Paper, 2014.

[21] Wang, H., Kolmanovsky, I., Amini, M. R., and Sun, J., "Model predictive climate control of connected and automated vehicles for improved energy efficiency," *2018 Annual American Control Conference (ACC)*, June 2018, pp. 828–833.

[22] Pirotais, F., Bellettre, J., Lecorre, O., Tazerout, M., De Pelsemaeker, G., and Guyonvarch, G., "A model of energetic interactions between a car engine, the cabin heating system and the electrical system," Tech. rep., SAE Technical Paper, 2002.

[23] Scattolini, R., "Architectures for distributed and hierarchical model predictive control–a review," *Journal of process control*, Vol. 19, No. 5, 2009, pp. 723–731.

[24] Stewart, B. T., Rawlings, J. B., and Wright, S. J., "Hierarchical cooperative distributed model predictive control," *Proceedings of the 2010 American Control Conference*, IEEE, 2010, pp. 3963–3968.

[25] Cominesi, S. R., Farina, M., Giulioni, L., Picasso, B., and Scattolini, R., "A two-layer stochastic model predictive control scheme for microgrids," *IEEE Transactions on Control Systems Technology*, Vol. 26, No. 1, 2017, pp. 1–13.

[26] Clarke, W. C., Manzie, C., and Brear, M. J., "Hierarchical economic MPC for systems with storage states," *Automatica*, Vol. 94, 2018, pp. 138–150.

[27] Koeln, J. P. and Alleyne, A. G., "Robust hierarchical model predictive control of graph-based power flow systems," *Automatica*, Vol. 96, 2018, pp. 127–133.

[28] Farina, M., Zhang, X., and Scattolini, R., "A hierarchical multi-rate MPC scheme for interconnected systems," *Automatica*, Vol. 90, 2018, pp. 38–46.

[29] Gong, X., Wang, H., Amini, M. R., Kolmanovsky, I., and Sun, J., "Integrated optimization of power split, engine thermal management, and cabin heating for hybrid electric vehicles," *3rd IEEE Conference on Control Technology and Applications (CCTA)*, August 2019.

[30] Amini, M. R., Sun, J., and Kolmanovsky, I., "Two-layer model predictive battery thermal and energy management optimization for connected and automated electric vehicles," *2018 IEEE Conference on Decision and Control (CDC)*, IEEE, 2018, pp. 6976–6981.

[31] Zhu, C., Lu, F., Zhang, H., and Mi, C. C., "Robust predictive battery thermal management strategy for connected and automated hybrid electric vehicles based on thermoelectric parameter uncertainty," *IEEE Journal of Emerging and Selected Topics in Power Electronics*, Vol. 6, No. 4, 2018, pp. 1796–1805.

[32] Rugh, J. and Farrington, R., "Vehicle ancillary load reduction project close-out report: an overview of the task and a compilation of the research results," Tech. rep., National Renewable Energy Lab.(NREL), Golden, CO (United States), 2008.

[33] Jeffers, M. A., Chaney, L., and Rugh, J. P., "Climate control load reduction strategies for electric drive vehicles in warm weather," Tech. rep., National Renewable Energy Lab.(NREL), Golden, CO (United States), 2015.

[34] "NREL works to increasee electric vehicle efficiency through enhanced thermal management," https://www.nrel.gov/docs/fy14osti/62241.pdf, Accessed: 2019-09-30.

[35] Khayyam, H., Kouzani, A. Z., Hu, E. J., and Nahavandi, S., "Coordinated energy management of vehicle air conditioning system," *Applied thermal engineering*, Vol. 31, No. 5, 2011, pp. 750–764.

[36] Rostiti, C., Stockar, S., and Canova, M., "A rule-based control for fuel-efficient automotive air conditioning systems," Tech. rep., SAE Technical Paper, 2015.

[37] Zhang, Q. and Canova, M., "Modeling air conditioning system with storage evaporator for vehicle energy management," *Automotive Air Conditioning*, Springer, 2016, pp. 247–266.

[38] Amini, M. R., Wang, H., Gong, X., Liao-McPherson, D., Kolmanovsky, I., and Sun, J., "Cabin and battery thermal management of connected and automated HEVs for improved energy efficiency using hierarchical model predictive control," *IEEE Transactions on Control Systems Technology*, 2019, pp. 1–16.

[39] Amini, M. R., Gong, X., Feng, Y., Wang, H., Kolmanovsky, I., and Sun, J., "Sequential optimization of speed, thermal load, and power split in connected HEVs," *2019 Annual American Control Conference (ACC)*, July 2019.

[40] Wang, H., Meng, Y., Zhang, Q., Amini, M. R., Kolmanovsky, I., Sun, J., and Jennings, M., "MPC-based precision cooling strategy (PCS) for efficient thermal management of automotive air conditioning system," *3rd IEEE Conference on Control Technology and Applications (CCTA)*, August 2019.

[41] Daanen, H. A., Van De Vliert, E., and Huang, X., "Driving performance in cold, warm, and thermoneutral environments," *Applied ergonomics*, Vol. 34, No. 6, 2003, pp. 597–602.

[42] Martinho, N., Silva, M., and Ramos, J., "Evaluation of thermal comfort in a vehicle cabin," *Proceedings of the Institution of Mechanical Engineers, Part D: Journal of Automobile Engineering*, Vol. 218, No. 2, 2004, pp. 159–166.

[43] Croitoru, C., Nastase, I., Bode, F., Meslem, A., and Dogeanu, A., "Thermal comfort models for indoor spaces and vehiclesCurrent capabilities and future perspectives," *Renewable and Sustainable Energy Reviews*, Vol. 44, 2015, pp. 304–318.

[44] Freire, R. Z., Oliveira, G. H., and Mendes, N., "Predictive controllers for thermal comfort optimization and energy savings," *Energy and buildings*, Vol. 40, No. 7, 2008, pp. 1353–1365.

[45] Ku, K., Liaw, J., Tsai, M., and Liu, T., "Automatic control system for thermal comfort based on predicted mean vote and energy saving," *IEEE Transactions on Automation Science and Engineering*, Vol. 12, No. 1, 2014, pp. 378–383.

[46] Chen, X., Wang, Q., and Srebric, J., "Model predictive control for indoor thermal comfort and energy optimization using occupant feedback," *Energy and Buildings*, Vol. 102, 2015, pp. 357–369.

[47] Farzaneh, Y. and Tootoonchi, A. A., "Controlling automobile thermal comfort using optimized fuzzy controller," *Applied Thermal Engineering*, Vol. 28, No. 14-15, 2008, pp. 1906–1917.

[48] Yan, X., Fleming, J., and Lot, R., "A/C energy management and vehicle cabin thermal comfort control," *IEEE Transactions on Vehicular Technology*, Vol. 67, No. 11, 2018, pp. 11238–11242.

[49] Brusey, J., Hintea, D., Gaura, E., and Beloe, N., "Reinforcement learning-based thermal comfort control for vehicle cabins," *Mechatronics*, Vol. 50, 2018, pp. 413–421.

[50] Schaut, S. and Sawodny, O., "Thermal management for the cabin of a battery electric vehicle considering passengers' comfort," *IEEE Transactions on Control Systems Technology*, 2019.

[51] Wang, H., Amini, M. R., Song, Z., Kolmanovsky, I., and Sun, J., "Combined energy and comfort optimization of air conditioning system in connected and automated vehicles," *2019 ASME Dynamic Systems and Control Conference (DSCC)*, October 2019.

[52] Kiss, T., Chaney, L., and Meyer, J., "New automotive air conditioning system simulation tool developed in MATLAB/Simulink," Tech. rep., National Renewable Energy Lab.(NREL), Golden, CO (United States), 2013.

[53] Zhang, Q., Meng, Y., Greiner, C., Soto, C., Schwartz, W., and Jennings, M., "Air conditioning system performance and vehicle fuel economy trade-Offs for a hybrid electric vehicle," *WCX 17: SAE World Congress Experience*, MAR., 2017.

[54] Zhang, Q., Li, S. E., and Deng, K., *Automotive air conditioning: optimization, control and diagnosis*, Springer, 2016.

[55] Fayazbakhsh, M. A. and Bahrami, M., "Comprehensive modeling of vehicle air conditioning loads using heat balance method," Tech. rep., SAE Technical Paper, 2013.

[56] Kelman, A. and Borrelli, F., "Bilinear model predictive control of a HVAC system using sequential quadratic programming," *IFAC Proceedings Volumes*, Vol. 44, No. 1, 2011, pp. 9869 – 9874, 18th IFAC World Congress.

[57] Oldewurtel, F., Parisio, A., Jones, C. N., Gyalistras, D., Gwerder, M., Stauch, V., Lehmann, B., and Morari, M., "Use of model predictive control and weather forecasts for energy efficient building climate control," *Energy and Buildings*, Vol. 45, 2012, pp. 15 – 27.

[58] Bhatti, M. S., "A critical look at R-744 and R-134a mobile air conditioning systems," *SAE Journal of Passenger Cars: Part 1*, 1997, pp. 781–805.

[59] Diehl, M., Findeisen, R., Allgower, F., Bock, H., and Schloder, J., "Nominal stability of real-time iteration scheme for nonlinear model predictive control," *IEE Proceedings-Control Theory and Applications*, Vol. 152, No. 3, 2005, pp. 296–308.

[60] Liao-McPherson, D., Huang, M., and Kolmanovsky, I., "A regularized and smoothed Fischer-Burmeister method for quadratic programming with applications to model predictive control," *IEEE Transactions on Automatic Control*, 2018, In press.

[61] Sun, C., Sun, F., Hu, X., Hedrick, J., and Moura, S., "Integrating traffic velocity data into predictive energy management of plug-in hybrid electric vehicles," *American Control Conference*, 2015, Chicago, IL, USA.

[62] Herrera, J. C., Work, D. B., Herring, R., Ban, X. J., Jacobson, Q., and Bayen, A. M., "Evaluation of traffic data obtained via GPS-enabled mobile phones: The Mobile Century field experiment," *Transportation Research Part C: Emerging Technologies*, Vol. 18, No. 4, 2010, pp. 568–583.

[63] Halbach, S., Sharer, P., Pagerit, S., Rousseau, A. P., and Folkerts, C., "Model architecture, methods, and interfaces for efficient math-based design and simulation of automotive control systems," Tech. rep., SAE Technical Paper, 2010.

[64] Risbeck, M. and Rawlings, J., "MPCTools: Nonlinear model predictive control tools for CasADi," 2016.

[65] Andersson, J. A., Gillis, J., Horn, G., Rawlings, J. B., and Diehl, M., "CasADi: a software framework for nonlinear optimization and optimal control," *Mathematical Programming Computation*, Vol. 11, No. 1, 2019, pp. 1–36.

[66] Atkinson, W. J., Hill, W. R., and Mathur, G. D., "The impact of increased air recirculation on interior cabin air quality," Tech. rep., SAE Technical Paper, 2017.

[67] Hudda, N. and Fruin, S., "Carbon dioxide accumulation inside vehicles: The effect of ventilation and driving conditions," *Science of The Total Environment*, Vol. 610, 2018, pp. 1448–1456.

[68] *Ergonomics of the thermal environment-Analytical determination and interpretation of thermal comfort using calculation of the PMV and PPD indices and local thermal comfort criteria*, ISO, 2005.

[69] Croitoru, C., Nastase, I., Bode, F., Meslem, A., and Dogeanu, A., "Thermal comfort models for indoor spaces and vehicles: current capabilities and future perspectives," *Renewable and Sustainable Energy Reviews*, Vol. 44, 2015, pp. 304–318.

[70] Hoof, J., "Forty years of Fangers model of thermal comfort: comfort for all?" *Indoor Air*, Vol. 18, No. 3, 2008, pp. 182–201.

[71] Farzaneh, Y. and Tootoonchi, A. A., "Controlling automobile thermal comfort using optimized fuzzy controller," *Applied Thermal Engineering*, Vol. 28, No. 14-15, 2008, pp. 1906–1917.

[72] Yan, X., Fleming, J., and Lot, R., "A/C energy management and vehicle cabin thermal comfort control," *IEEE Transactions on Vehicular Technology*, Vol. 67, No. 11, 2018, pp. 11238–11242.

[73] Szwabowski, S. J., MacNeille, P., Kolmanovsky, I. V., and Filev, D., "In-vehicle ambient condition sensing based on wireless internet access," Tech. rep., SAE Technical Paper, 2010.

[74] Freire, R. Z., Oliveira, G. H., and Mendes, N., "Predictive controllers for thermal comfort optimization and energy savings," *Energy and buildings*, Vol. 40, No. 7, 2008, pp. 1353–1365.